

ABSTRACT

Title of thesis: THERMAL CHARACTERIZATION
OF FIREBRAND PILES

Raquel Hakes, Masters of Science, 2017

Thesis directed by: Professor Michael J. Gollner
Department of Fire Protection Engineering

Over the past several decades, the severity of wildland-urban interface (WUI) fires has increased drastically, resulting in thousands of structures lost globally each year. The cause of the majority of structure losses is ignition via firebrands, small pieces of burning material which are generated from burning vegetation and structures. In this thesis, a methodology for studying the heating to recipient fuels by firebrands is developed. Small-scale experiments designed to capture heating from firebrand piles and the process of ignition were conducted using laboratory-fabricated cylindrical wooden firebrands. The methodology compares two heat flux measurement methods. Experimental results compare the effects of varying firebrand diameter, pile mass, and wind speed. An ignition condition is described using temperature and heat flux.

THERMAL CHARACTERIZATION OF FIREBRAND PILES

by

Raquel Sara Pilar Hakes

Thesis submitted to the Faculty of the Graduate School of the
University of Maryland, College Park in partial fulfillment
of the requirements for the degree of
Masters of Science
2017

Advisory Committee:
Professor Michael J. Gollner, Chair/Advisor
Professor Stanislav I. Stoliarov
Dr. Jiann C. Yang

© Copyright by
Raquel Sara Pilar Hakes
2017

Acknowledgments

I would like to thank the many, many people who have helped me along the way. A big thank you particularly to my advisor, Professor Michael Gollner, for the opportunity to work with him over the past several years. This project in particular gave me the opportunity to grow a lot as a researcher. Thank you very much for your time and advice throughout this project.

I would also like to thank my committee members, Dr. Jiann Yang and Professor Stanislav Stoliarov. In addition to taking the time to read this thesis and provide their thoughts and feedback, they both provided support to the project as I was conducting it. Thank you to Dr. Yang for providing ideas and suggesting papers relevant to the problem throughout the project. Thank you to Dr. Stoliarov for allowing me the use of his cone calorimeter and the help of his students.

I was very fortunate to have several other students at the University of Maryland to help me throughout this project. I am very grateful to Hamed Salehizadeh for the time he spent running many, many experiments. I am also grateful to Matthew Weston-Dawkes, for the time he spent setting up and helping to run experiments. Thank you to Erin Griffith, Alicea Fitzpatrick, and Seth Lattner for jumping onto the project towards the end to help finish up calibrations. Thank you to the others that contributed time helping on experiments and in the lab: Evan Sluder and Nicole Welch.

I was particularly lucky to work with Sara Caton as we both began Masters on firebrand projects. I am grateful for her support and companionship in the lab and

the office. In general, I was fortunate to work in a lab group of fun and interesting people. I had the privilege of working in a department full of many wonderful colleagues. Thank you to the many friends who ate lunch with me, talked through research thoughts, and in general made the office a great place to work.

I would like to acknowledge the financial support, advice, and encouragement I received from the WUI Group at NIST.

I would like to acknowledge Tim Holy, who made the MATLAB function `distinguishablecolors.m`, which I used for plots included in this thesis.

Finally, I would like to thank my family and my fiance, Will. All of you have been my biggest supporters and believed in me completely. Thank you for encouraging me to continue with the Master's when I was uncertain about concussion recovery. I am always grateful for your love.

There are many others who provided me with advice, support, encouragement, and feedback. Thank you to all of you.

Table of Contents

List of Tables	vi
List of Figures	vii
List of Abbreviations	xiii
1 Introduction	1
1.1 Motivation	4
1.2 Objectives	6
2 Literature Review	8
2.1 Overview	8
2.2 Ignition: Flaming and Smoldering	9
2.2.1 Theories of Ignition	11
2.3 Experimental Studies	13
2.3.1 Firebrand Production	13
2.3.2 Firebrand Ignition of Vegetative Fuels	14
2.3.3 Firebrand Ignition of Solid Fuels	16
3 Experimental Methodology	18
3.1 Overview	18
3.2 Calibration Tests	20
3.3 Heat Flux Tests With Firebrand Piles	24
3.3.1 Experimental Design	25
3.3.2 Wood Properties and Firebrand Production	28
3.4 Experimental Procedures	31
3.4.1 Firebrand Pile Tests Using Thin-Skin Calorimeters	32
3.4.2 Firebrand Pile Tests Using Water-Cooled Heat Flux Gauge	33
3.5 Tests Under Forced Flow Conditions	35
3.5.1 Ignition Test Set-up	35
3.5.2 Thin-Skin Calorimeter Forced Flow Experiments	38

4	Measurement Techniques and Calibration Results	40
4.1	Overview	40
4.2	Heat Flux: Water-Cooled Heat Flux Gauge	40
4.2.1	Results of Gauge Size Comparison	41
4.3	Heat Flux: Thin-Skin Calorimeters	42
4.3.1	Fabrication	43
4.3.2	Calibration	45
4.3.3	Theoretical Formulation	47
4.3.4	Results of Calibration	50
4.3.5	Application of Calibration to Experiments	52
5	Results of Firebrand Pile Tests	59
5.1	Overview	59
5.2	Visual Observations	59
5.3	Thermocouple and Thin-Skin Calorimeter Temperature Results	61
5.4	Heat Flux Results	65
5.4.1	Components of Heat Transfer	65
5.4.2	Spatial Distribution of Heat Flux	67
5.5	A Comparison of Heating From Piles	73
5.5.1	Effect of Brand Diameter	73
5.5.2	Effect of Pile Mass	77
5.5.3	Peak Heat Flux and Net Heating	80
6	Results of Ignition Tests	89
6.1	Overview	89
6.2	Visual Observations	89
6.2.1	Description of the Ignition Process	92
6.3	Thermal Characteristics at Ignition	94
6.3.1	Temperatures	94
6.3.2	Heat Flux	97
6.3.3	Spatial Distribution of Heat Flux	99
7	Discussion	103
7.1	Firebrand Pile Heat Flux Tests	103
7.2	Ignition Tests	104
8	Conclusions	108
8.1	Overview	108
8.2	Conclusions	108
8.3	Recommendations for Future Work	110
A.1	Raw Thin-Skin Calorimeter Results	113
A.2	Raw Water-Cooled Heat Flux Gauge Results	120
A.3	Gauge Comparison Plots	125
	Bibliography	132

List of Tables

3.1	The test matrix. For each type of test, experiments were conducted using the diameter and masses of firebrands indicated. Note that the masses listed are initial mass before burning.	19
-----	--	----

List of Figures

1.1	Firebrand pile forms on a deck during wind-driven firebrand shower experiments. Figure from Manzello and Suzuki [1].	4
2.1	Possible formulation of the energy balance of a firebrand pile on (left) a flat solid fuel, and (right) a solid fuel with a crevice. Based on Manzello and Suzuki [1].	9
2.2	Ignition results of experiments plotted with theoretical ignition boundary. Figure from Hadden <i>et al.</i> [2].	12
3.1	Side view photograph of radiant heater calibration set-up. The radiant heater is on the right side of the figure; gauges are set up on the left side of the figure.	23
3.2	Schematic side view of both heat flux experimental set-ups with propane burner for fabricating firebrands. Figure of burner from Caton [3]. Not drawn to scale.	26
3.3	Top view of the experimental board using thin-skin calorimeters with reference numbering of calorimeters (drawn to scale). Thermocouple location shown in center of thin-skin array.	27
3.4	Comparison of heat flux calculated using initial calibration and new calibration after five tests of 12.7 mm firebrands with a 50 g initial pile mass.	34
3.5	Schematic of recipient fuel configurations oriented with respect to wind direction.	38
3.6	Schematic side view of wind tunnel set-up for thin-skin calorimeter heat flux tests, showing direction of wind and angles of cameras. Not drawn to scale.	39
4.1	Comparison of heat fluxes measured for a 50 g initial mass 12.7 mm diameter firebrand pile.	42
4.2	Energy balance around control volume of a single thin-skin calorimeter.	47
4.3	Components of heat flux for one radiant heater thin-skin calorimeter calibration test.	51
4.4	Linear fit to correction factor.	52

4.5	Thin-skin calorimeter temperature as a function of time for 16 thin-skins in array. Thin-skin calorimeter locations can be found in Figure 3.3.	54
4.6	Total heat flux imparted to the thin-skin calorimeters, calculated using measured thin-skin calorimeter temperatures.	55
4.7	Averaged heat flux results for a 12.7 mm diameter firebrand, 9.6 g deposited mass pile, measured using the water-cooled heat flux gauge.	56
4.8	Magnified replication of previous figure of averaged heat flux results for a 12.7 mm diameter firebrand, 9.6 g deposited mass pile, measured using the water-cooled heat flux gauge, showing long-time trends.	57
4.9	Plot of averaged heat flux over all repetitions for a 12.7 mm, 9.6 g test to compare heat fluxes obtained using thin-skin calorimeters and the water-cooled heat flux gauge.	58
5.1	Image sequence showing varying firebrand pile sizes, increasing in diameter from left to right and increasing in pile mass from top to bottom.	60
5.2	Temperature as a function of time as measured by thin-skin calorimeters and thermocouple beneath 12.7 mm diameter firebrand pile of 9.6 g deposited mass.	62
5.3	Temperature as a function of time as measured by the thermocouple and its four immediate nearest thin-skin calorimeters for a 12.7 mm diameter firebrand pile of 9.6 g deposited mass.	63
5.4	A comparison of temperature as a function of time for the thermocouple and an average temperature of the thin-skin calorimeters initially covered by the firebrand pile for a 12.7 mm diameter firebrand pile of 9.6 g deposited mass.	64
5.5	Components of heat transfer for a single thin-skin calorimeter during a piled test.	66
5.6	Components of heat transfer for the covered thin-skin calorimeter of a single firebrand test.	67
5.7	Heat flux as a function of time for a 12.7 mm diameter, 9.6 g deposited mass test, measured using the thin-skin calorimeter array with coverage of thin-skins denoted.	68
5.8	Averaged temperatures of thin-skin calorimeters based on coverage: full, partial, or no coverage (12.7 mm diameter, 9.6 g deposited mass test).	69
5.9	Averaged heat flux of thin-skin calorimeters based on coverage: full, partial, or no coverage (12.7 mm diameter, 9.6 g deposited mass test).	70
5.10	Evolution of spatial distribution of heat flux for a 5 g deposited mass pile of 12.7 mm at 100 s, 150 s, 400 s, 900 s, and 1400 s after firebrands are deposited.	71

5.11	Comparison of spatial heat flux maps for (left) a single firebrand, and (right) the largest pile size, 9.6 g deposited mass. From top to bottom, heat flux maps shown an instantaneous heat flux approximately 1 min into the test, averaged heat flux over the entire test, and maximum heat flux for each location. Due to large heat flux differences, the color bar values change for each plot.	72
5.12	A comparison of averaged point measurements from the water-cooled heat flux gauge of 6.35 mm and 9.52 mm diameter firebrands for a single firebrand. The larger diameter produces a higher heat flux and lasts longer.	74
5.13	A comparison of averaged point measurements from the water-cooled heat flux gauge of 6.35 mm and 9.52 mm diameter firebrands for a 1 g pile, deposited mass. Differences in heat flux are well within the standard deviation of the average.	75
5.14	A comparison of averaged point measurements from the water-cooled heat flux gauge of 6.35 mm and 12.7 mm diameter firebrands for a 2.8 g pile, deposited mass. There is no trend apparent between heat flux and diameter.	76
5.15	A comparison of averaged point measurements from the water-cooled heat flux gauge of 9.52 mm and 12.7 mm diameter brands for a 5 g pile, deposited mass. The drop-off of the 9.52 mm curve is due to averaging; the average heat flux curve was calculated only as long as the shortest test. The larger diameter produces higher heat fluxes.	77
5.16	A comparison of averaged heat flux curves obtained using the water-cooled heat flux gauge as deposited pile mass increases for 6.35 mm firebrand piles.	78
5.17	A comparison of averaged heat flux curves obtained using the water-cooled heat flux gauge as deposited pile mass increases for 9.52 mm firebrand piles.	79
5.18	A comparison of averaged heat flux curves obtained using the water-cooled heat flux gauge as deposited pile mass increases for 12.7 mm firebrand piles.	79
5.19	A comparison of averaged heat flux curves obtained using the thin-skin calorimeters as deposited pile mass increases for 12.7 mm firebrand piles.	80
5.20	Peak heat flux as a function of firebrand diameter from thin-skin calorimeter tests.	81
5.21	Peak heat flux as a function of firebrand diameter from water-cooled heat flux gauge tests.	82
5.22	Peak heat flux as a function of deposited mass from thin-skin calorimeter tests.	83
5.23	Peak heat flux as a function of deposited mass from water-cooled heat flux gauge tests.	84
5.24	Net heating parameter as a function of firebrand diameter for water-cooled heat flux gauge tests.	85

5.25	Net heating parameter as a function of deposited pile mass for thin-skin calorimeter tests.	86
5.26	Net heating parameter as a function of deposited pile mass for water-cooled heat flux gauge tests.	87
5.27	Net heating parameter as a function of number of firebrands in the pile. Each marker is an average of all repetitions conducted for a specific test condition. Error bars are the standard deviation of the repetitions.	88
6.1	Side view of a flat ignition experiment immediately after firebrand pile is deposited. A small flame occurs in the upper right hand portion of the image. Wind direction right to left.	90
6.2	Side view of flat ignition experiment over OSB 1 min into experiment. Flames anchored to the fuel surface are visible. The wind direction is from right to left.	91
6.3	Side view of a flat ignition experiment over OSB 10 min into the experiment. Flaming combustion is sustained for the recipient fuel. The wind direction is from right to left.	92
6.4	Side view of flat ignition experiment over OSB 15 min into the experiment. Flaming combustion has ceased. The wind direction is from right to left.	93
6.5	Conceptualization of possible ignition processes that occur when firebrands ignite a recipient fuel.	93
6.6	Visual image (left) and IR image (right) captures for, from top to bottom: 1 min, 10 min, and 15 min into an ignition test. Note the changed scales on the IR images. The wind is from the right side of images.	95
6.7	A comparison of the thermocouple temperatures and thin-skin temperatures averaged over all covered thin-skins for one test of 10 g deposited mass.	96
6.8	A comparison of the thermocouple temperature with the temperatures measured by the four thin-skin calorimeters surrounding the thermocouple for the same test as previous figure.	97
6.9	Heat flux as a function of time for the full thin-skin calorimeter array for a 10 g deposited mass test with applied wind.	98
6.10	Averaged heat flux curves for 10 g deposited mass tests with wind.	99
6.11	Spatial distribution of heat flux approximately 1 min into a test with 10 g deposited pile mass. Wind direction right to left.	100
6.12	Spatial distribution of heat flux over 10 min into the same test with 10 g deposited pile mass. Wind direction right to left.	101
6.13	Spatial distribution of heat flux averaged over the first two thirds of the forced flow test with a 10 g firebrand mass.	101
6.14	Spatial distribution of the maximum heat flux obtained for each point during the forced flow 10 g mass test.	102

7.1	A comparison of averaged heat flux curves, measured with thin-skin calorimeters, under ambient and forced flow conditions. The dashed lines represent initial mass 50 g test while the solid lines represent initial mass 100 g tests. All tests use 12.7 mm diameter firebrands.	106
7.2	Net heating parameter as a function of deposited pile mass for ambient and forced flow experiments using 12.7 mm diameter firebrands.	107
1	Heat flux as a function of time measured by the thin-skin calorimeter array under ambient conditions for 6.35 mm diameter firebrands of 100 g initial mass.	113
2	Heat flux as a function of time measured by the thin-skin calorimeter array under ambient conditions for 9.52 mm diameter firebrands of 100 g initial mass.	114
3	Heat flux as a function of time measured by the thin-skin calorimeter array under ambient conditions for 12.7 mm diameter firebrands of 100 g initial mass.	115
4	Heat flux as a function of time measured by the thin-skin calorimeter array under ambient conditions for 12.7 mm diameter firebrands of 50 g initial mass.	116
5	Heat flux as a function of time measured by the thin-skin calorimeter array under ambient conditions for 12.7 mm diameter firebrands of 20 g initial mass.	117
6	Heat flux as a function of time measured by the thin-skin calorimeter array under ambient conditions for 12.7 mm diameter firebrands of 1 brand.	118
7	Heat flux as a function of time measured by the thin-skin calorimeter array under forced flow conditions for 12.7 mm diameter firebrands of 100 g initial mass.	119
8	Heat flux as a function of time measured by the thin-skin calorimeter array under forced flow conditions for 12.7 mm diameter firebrands of 50 g initial mass.	120
9	Heat flux as a function of time as measured by the water-cooled heat flux gauge for 6.35 mm firebrands and 6.3 g deposited mass.	121
10	Heat flux as a function of time as measured by the water-cooled heat flux gauge for 9.52 mm firebrands and 8.2 g deposited mass.	122
11	Heat flux as a function of time as measured by the water-cooled heat flux gauge for 12.7 mm firebrands and a single brand test.	123
12	Heat flux as a function of time as measured by the water-cooled heat flux gauge for 12.7 mm firebrands and 2.7 g deposited mass.	124
13	Heat flux as a function of time as measured by the water-cooled heat flux gauge for 12.7 mm firebrands and 5.2 g deposited mass.	125
14	Comparison of average heat flux results using the thin-skin calorimeter array vs. the water-cooled heat flux gauge. 6.35 mm diameter, 100 g initial mass.	126

15	Comparison of average heat flux results using the thin-skin calorimeter array vs. the water-cooled heat flux gauge. 9.52 mm diameter, 100 g initial mass.	127
16	Comparison of average heat flux results using the thin-skin calorimeter array vs. the water-cooled heat flux gauge. 12.7 mm diameter, 100 g initial mass.	128
17	Comparison of average heat flux results using the thin-skin calorimeter array vs. the water-cooled heat flux gauge. 12.7 mm diameter, 50 g initial mass.	129
18	Comparison of average heat flux results using the thin-skin calorimeter array vs. the water-cooled heat flux gauge. 12.7 mm diameter, 20 g initial mass.	130
19	Comparison of average heat flux results using the thin-skin calorimeter array vs. the water-cooled heat flux gauge. 12.7 mm diameter, single brand.	131

Nomenclature

c_p	Specific Heat (J/kg K)
Gr	Grashof Number (-)
h	Convective Heat Transfer Coefficient (W/m ² K)
k	Thermal Conductivity (W/mK)
Nu	Nusselt Number (-)
Pr	Prandtl Number (-)
\dot{q}''	Heat Flux per Unit Area (W/m ²)
Ra	Rayleigh Number (-)
t	Time (s)
T	Temperature (K)

Greek symbols

α	Absorptivity (-)
δ	Thickness (m)
ε	Emissivity (-)
ρ	Density (kg/m ³)
σ	Stefan-Boltzmann Constant (W/m ² K ⁴)
ν	Kinematic viscosity (m ² /s)

Subscripts

θ	Initial Value
∞	Ambient Value
cond	Conductive Term
conv	Convective Term
inc	Incident Term
indepth	In-depth Term
max	Maximum Value
net	Net Value
opt	Optimum
rad	Radiative Term
rerad	Reradiative Term
stor	Storage Term

Abbreviations

ASTM	American Society for Testing and Materials
IR	Infrared
MC	Moisture Content
OSB	Oriented Strand Board
NIST	National Institute of Standards and Technology
TSC	Thin-Skin Calorimeter
WUI	Wildland-Urban Interface

Chapter 1: Introduction

Over the past several decades, the number of devastating wildland-urban interface (WUI) fires has increased drastically. The WUI is defined as the location where human development abuts or intermixes with wildland vegetation [4]. Fires that enter these areas are referred to as WUI fires and pose a significant hazard to homes, people, businesses, and infrastructure. Although the number of wildland fires has remained relatively constant over the past several decades, the number of wildland fires affecting human development has increased dramatically. In 2016 over 4,000 structures were destroyed by wildfires in the United States alone. On average, over 2,000 structures in the United States are lost annually to wildland fires [5]. Global statistics reflect similar trends [6].

A number of factors have influenced the increase in the number of WUI fires: climate change, fuel management practices, and an increase in human development into WUI areas [7]. Local changes in climate have occurred in many wildland fire-prone areas, resulting in hotter temperatures and less precipitation. These changes affect the likelihood of the initiation and spread of wildland fires. Lower moisture content (MC) of fuels, as a result of hot temperatures and low precipitation, increases the severity of wildland fires, as dry fuels are able to ignite more quickly, thus

spreading the fire more quickly. In the early 1900s, the United States Forest Service introduced a policy to suppress all wildland fires [8]. Although large fires can result in high structure and economic loss, small fires are a natural part of the environment and work to mitigate fuel build-up in forests, actually decreasing the likelihood of large, severe fires. The result of the Forest Service policy was a huge build-up in fuels across the country. When fires burn in areas with major fuel build-up, they can often become severe. Finally, by 2000, WUI development had increased by 50% since 1970, and expansion into WUI areas is expected to continue [9]. Increased human development in WUI areas increases the number of structures at risk during WUI fires, as structures are being built in areas that have traditionally burned without being a threat to human development.

Structures ignite in a wildland fire when the structure is directly or indirectly exposed to flames or heat from the fire. Three exposure processes are typically defined for WUI fires: radiation, direct flame contact, and firebrands [7]. Radiant ignition of structures occurs in a WUI fire when the fire front or another burning object (e.g. a nearby structure or tree already ignited by the fire) produces sufficient heat flux over an extended period of time to ignite the structure at a distance. Although radiant ignition can occur in wildland fires, results of the International Crown Fire Modeling Experiments found that no ignition of wooden wall segments occurred when the wall was 20 m or more from an actively crowning 150 kW/m^2 fire [10]. Direct flame contact causes ignition of structures in WUI fires when vegetation (e.g. ornamental bushes) or other flammable material, such as fallen leaves, forms an unbroken path from the fire to the structure. Both of these ignition conditions

can be mitigated using known methods, such as maintaining adequate defensible space around a structure [11].

Investigations of past fires, such as the Grass Valley Fire [12], the Waldo Canyon Fire [13,14], and Witch and Guejito Fires [15,16], have found that firebrands are responsible for the majority of structure losses in WUI fires [17]. Firebrands, or burning embers, are small pieces of burning material generated from vegetation or burning structures during a fire. Firebrands are lofted in the fire plume and can be transported up to 9 km ahead of the fire front [16]. Firebrands can land in either a smoldering or a flaming state and cause ignition of a structure several hours after the main fire front has passed. Even though the evidence shows that firebrands cause the majority of structure ignitions, firebrands have received less research attention than radiant ignition has.

Firebrand research that has been conducted can be split into work on three mechanisms: firebrand generation, lofting and transportation of firebrands, and deposition and ignition by firebrands [7]. Firebrand generation describes the production of embers in a wildland fire and how those embers break off from structures and vegetation. Firebrand lofting and transport describes the mechanisms which can loft firebrands from the buoyant plume and transport them over large distances, reported to be as far as 9 km in some cases [16]. Firebrand deposition and ignition describes the processes that occur when a firebrand lands on a recipient material. If this material is combustible, such as a pile of mulch or a deck, ignition describes the process by which the firebrands ignite the material.

1.1 Motivation

The mechanisms governing ignition by firebrands are not well-studied. In particular, wind-driven firebrand studies by Manzello and Suzuki [1] have found that firebrands typically form piles and ignition tends to occur in locations with firebrand piles, as shown in Figure 1.1. Despite the importance of firebrand piles for ignition, most previous small-scale work has focused on ignition by a single firebrand. A number of large-scale studies (full-scale structures or structural components) exist which investigate ignition propensity from piles [37]; however, few small-scale studies using firebrand piles can be found in the literature (e.g. [18]).



Figure 1.1: Firebrand pile forms on a deck during wind-driven firebrand shower experiments. Figure from Manzello and Suzuki [1].

During a wildland fire, firebrands can ignite vegetative fuels, such as leaves or grasses, or WUI fuels, such as decks, porches, fences, or other dense fuels. Previous studies on structure loss have found that ignition by firebrands is often indirect (i.e.

firebrands ignite an adjacent structure, such as the WUI fuels described, and that adjacent structure subsequently ignites the structure). Previous work on firebrand ignition has focused primarily on vegetative fuels, which are more porous than solid WUI fuels. The porosity of vegetative fuels allows firebrands to embed themselves in the recipient fuel, creating greater contact between the ignition source and fuel. On the other hand, the contact area between solid fuels and firebrands is much smaller. Firebrands accumulate in piles on top of solid fuels. The behavior of firebrand piles is expected to be different than that of a single firebrand because the heating from individual brands in the pile can interact. The pile behaviour, as well as the fact that the fuel is solid rather than porous, is likely to change the heat transfer mechanisms governing the smoldering ignition process and the transition from smoldering to flaming ignition.

This work aims to fill some of the gaps in firebrand ignition research. One part of the research is to study the heat fluxes produced by piles of smoldering firebrands in order to understand the contact heat transfer between firebrands and the recipient fuel. No data currently exists quantitatively connecting pile sizes (measured by the mass or number of firebrands) and ignition; however, qualitative results of other studies [18] suggest that greater numbers of firebrands are significantly more likely to ignite a recipient fuel than are single firebrands. The work aims to determine whether there is a link between pile size and ignition and describe the process of ignition of typical WUI fuels.

1.2 Objectives

The ultimate goal of this research is to understand the ignition process of dense structural WUI fuels by firebrand piles. Ultimately, understanding the ignition process of these fuels can allow for the development of a model of the ignition process. There are three main objectives in this work.

In order to measure the heating from and thermal characteristics of firebrand piles, it is necessary to have a method to reliably conduct pile experiments and measure relevant thermal quantities. The first objective of this study was thus to formulate a methodology for measuring temperatures and heat fluxes in experiments using smoldering firebrands. This objective necessitated the development of a reproducible and repeatable method for the creation of firebrand piles and a reliable method of measuring heat fluxes from firebrand piles to different substrates, including identifying the best sensor to measure the heat fluxes in firebrand piles.

The second objective of this study was to quantify the heat flux from firebrand piles to an inert surface, in order to isolate the heat flux produced by firebrands from the heat flux produced when a recipient fuel ignites. This objective was feasible after the first objective had been completed. This objective included determining how parameters such as firebrand diameter and pile size (mass, number) affect changes in heating behavior.

The final objective was to describe the ignition process and the thermal characteristics (heat flux, temperature) at the time of flaming ignition. The objective was meant to connect ignition and heat fluxes measured for the second objective.

Conducting firebrand pile experiments on a recipient fuel and on an inert substrate allowed for a description of ignition conditions.

Chapter 2: Literature Review

2.1 Overview

The main goal of this project is to understand the ignition process by which firebrand piles ignite recipient WUI fuels. In this chapter, an overview of ignition is provided in order to form a basis for understanding the firebrand pile. The differences between radiant ignition and ignition via firebrand piles are discussed, as are the differences between flaming and smoldering ignition. The chapter concludes with a discussion of previous experimental studies of firebrand ignition.

Ignition is the initiation of either flaming or smoldering combustion. This process is associated with a temperature rise of a fuel to a certain critical point. In the case of flaming ignition, the temperature rise results in pyrolysis of the solid fuel to gaseous fuel. At a critical mass flux, this gaseous fuel will ignite. In the case of smoldering ignition, combustion takes place in the solid phase. An important aspect of this process is how energy, in the form of heat, is transferred to a fuel in order to initiate a temperature rise.

The heat transfer process for a firebrand pile is not completely understood; however, Figure 2.1 shows hypothetical formulations of the possible energy balance of a firebrand or firebrand pile on a recipient fuel. Firebrands ignite recipient fuels

due to heat transfer across an interface. Depending on how well the firebrand contacts the recipient fuel, which may be poor for solid fuel but relatively good for porous fuels, conduction or radiation will dominate the heat transfer process. This heat transfer will occur in a variety of modes that ultimately result in in-depth heat transfer to the recipient fuel, $\dot{q}''_{indepth}$, eventually heating the fuel until it ignites. The pile will also produce heat due to continued smoldering, proportional to the rate of mass loss and latent heat of the fuel, $\dot{m}''L$; however, the pile will also lose heat due to convection, \dot{q}''_{conv} and radiation \dot{q}''_{rad} to the ambient. For situations when there is a gap in the fuel, it is suspected there could be additional re-radiation within the fuel bed and access to oxygen that promotes surface oxidation, making smoldering ignition and transition to flaming easier.

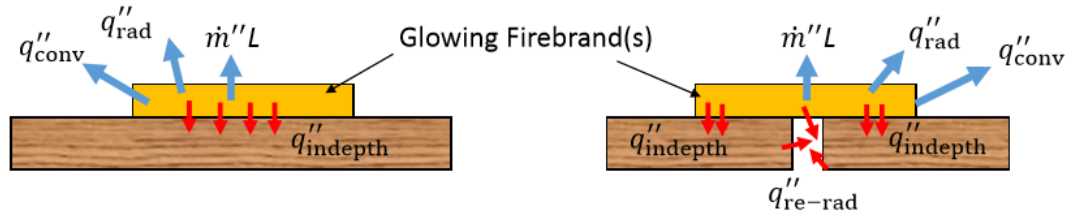


Figure 2.1: Possible formulation of the energy balance of a firebrand pile on (left) a flat solid fuel, and (right) a solid fuel with a crevice. Based on Manzello and Suzuki [1].

2.2 Ignition: Flaming and Smoldering

Descriptions of flaming and smoldering ignition are provided. Ignition theories applicable to the current problem are reviewed. A description of flaming ignition and

ignition by radiation is described because these areas have received more research attention. Understanding the ways in which researchers formulate and describe radiant ignition can provide context when formulating a way to describe ignition by firebrand piles. A brief review of smoldering combustion and its thermal characteristics is provided in order to give a comparison to the magnitude of thermal characteristics measured in this study’s heat flux and ignition experiments.

There are several methods of describing a critical ignition point for radiant ignition. Radiant ignition can occur as a result of a sustained ignition temperature [19], sustained heat flux over a given period of time [10], or a certain mass flux over a given time [20].

While ignition thresholds such as those described above are typically used to determine flaming auto-ignition, the initiation of smoldering combustion is particularly important in our application. Smoldering is a solid phase combustion process, a heterogeneous oxidation reaction, which peaks at lower temperatures and heat release rates than flaming combustion – approximately 450–700°C and 10–30 kW/m² [21].

In addition to producing lower peak temperatures, critical thresholds for smoldering combustion are also lower. For example, Rein found that under an incident radiant heat flux, smoldering ignition of polyurethane could be initiated at 7 kW/m², while spontaneous flaming ignition did not occur until 30 kW/m² [21]. Anthenien and Fernandez-Pello were able to ignite polyurethane using conduction at as low as 3.1 kW/m² [22]. Although these values are for polyurethane, which has different thermal properties than WUI fuel materials (woods, plastics, and wood-plastic

composites), the comparison between values for critical heat flux for smoldering and flaming ignition are notable as the values for smoldering are significantly lower. Gratkowski *et al.* conducted experiments on the smoldering ignition of plywood in a cone calorimeter. They found that the minimum heat flux at which the plywood would ignite was 7.5 kW/m^2 [23].

2.2.1 Theories of Ignition

A number of theories of ignition have been developed which are related to the problem of firebrand ignition, although some of these theories have been developed for other related applications. Gol'shleger *et al.* provide a theory of hot spot ignition, which assumes a hot, inert object lands on a reactive material. The object is assumed to create pockets of heating in the recipient fuel, and these hot areas are assumed to be the locations where ignition occurs [24]. Although this theory could be a good starting point, the assumption of an inert object is not valid for the firebrand problem.

Hadden *et al.* [2] performed experiments using hot metal particles to ignite cellulose fuel beds. They varied the particle size and found a hyperbolic relationship between the particle size and particle temperature required to ignite the fuel bed. They applied hot spot theory to their data and obtained a qualitative fit. Results of the experimental study and the theoretical fit can be seen in Figure 2.2. Further experiments by Zak *et al.* [25] and Fernandez-Pello *et al.* [26] have noted the importance of heat losses from larger particles. The hot spot theory, though qualitatively

validated, does not take into account ongoing reactions in the hot particles, which may play an important role in firebrand pile heating.

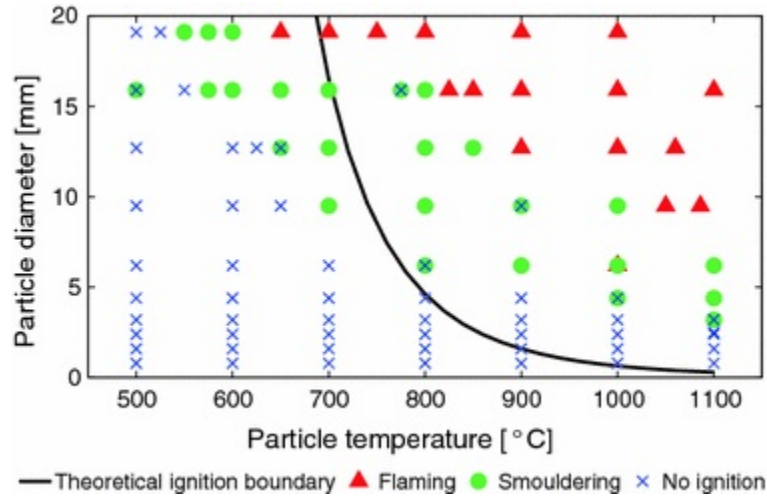


Figure 2.2: Ignition results of experiments plotted with theoretical ignition boundary. Figure from Hadden *et al.* [2].

Gray also discusses the concept of criticality, hypothesizing that critical ignition curves can be plotted where the heat loss from a hot object balances with the heat generation within the fuel [27]. This concept is similar to the ignition boundary plotted by Hadden *et al.* [2]. This concept could be important in terms of defining ignition criteria for firebrand ignition of solid fuels.

In a different analysis, Gratkowski *et al.* employed the Frank-Kamenetskii parameter, a measure of thermal stability, when using self-heating ignition theory. This parameter indicates the balance of heat generation in relation to heat losses and whether the heat generation will be sufficiently larger to cause thermal runaway of the system [23]. The theory found good agreement with experiments of radiant smouldering ignition of plywood and with self-heating theory.

Another theory of ignition is to solve the energy equations of a smoldering reaction in order to determine a critical ignition heat flux as a function of smoldering depth. This method is described in Dosanjh and Pagni [28] and applied experimentally to the smoldering ignition of polyurethane in Anthenien and Fernandez-Pello [22]. Using this method, Anthenien and Fernandez-Pello found good agreement between the experiments and the theoretical prediction of ignition as a function of critical heat flux and time.

2.3 Experimental Studies

A number of previous studies have explored facets of the firebrand ignition problem, both experimentally and theoretically. A review of these studies provides background on current experimental methods which can be a useful comparison for formulating the research methods used for the current study.

The following sections describe experimental studies on ignition by firebrands. Specifically, different firebrand production methods are discussed, and ignition experiments on vegetative and solid WUI fuels are reviewed to highlight important considerations when formulating the experiments in this study.

2.3.1 Firebrand Production

A review of firebrand production methods used in previous studies was conducted before determining the method used in the current study. Below are concise descriptions of several firebrand production methods. Ellis [?] fabricated glowing

firebrands from eucalyptus bark by igniting the sample using a gas stove and then placing it in a “truncated cone”, in which the sample rotated while exposed to airflow. This method was used only for a single firebrand. Santamaria *et al.* [30] simulated firebrands both with charcoal and by submerging virgin material into flames from a heptane pool fire. In a method which would later be used in the National Institute of Standards and Technology (NIST) firebrand generator, called the NIST Dragon, Manzello *et al.* suspended small Ponderosa Pine (*Pinus ponderosa*) disks above butane flames to produce either flaming or glowing firebrands [18]. After a set time, the firebrands were exposed to wind and became part of a firebrand shower.

Dowling [31] ignited wooden cribs and set them adjacent to his experiment. A similar procedure was used by Quarles *et al.* [32] when they tested decks for firebrand exposure by igniting a wood crib on top of the deck. Other methods for producing flaming firebrands include igniting virgin fuel (e.g. wood, bark) with a flame and allowing it to burn [33]. None of the studies reported time in flames or whether the time was held constant for all tests; however, the use of flames for firebrand production is a common and successful option. A refinement on this method was utilized in this study.

2.3.2 Firebrand Ignition of Vegetative Fuels

A collection of experimental studies exist which focus on ignition of fuels by firebrands. A number of these studies focus on recording Ignition vs. No Ignition

for a range of experimental parameters; however, these studies do not investigate heat fluxes associated with ignition or the mechanisms governing the transition from smoldering to flaming ignition. A large number of studies on firebrand ignition utilize vegetative fuels as the recipient fuel. Many studies also use one firebrand or a small number of firebrands, rather than large piles. Of these studies, many explore ignition as a function of number of firebrands deposited. There are a number of larger scale studies using solid fuels as the recipient fuel for ignition experiments.

Manzello *et al.* [18] used either a single brand or three to four firebrands to test ignition of pine needles, shredded paper, and cedar wood crevices. A single glowing firebrand was able to initiate smoldering in the completely dry shredded paper under an external airflow of 0.5 - 1.0 m/s. Four large (50 mm diameter disk) firebrands were able to ignite pine needles, which transitioned from smoldering to flaming under a 1.0 m/s wind. No glowing firebrands were able to ignite the cedar crevice. In later tests, Manzello *et al.* [34] conducted similar tests as described above on three other fuels: shredded hardwood mulch, pine straw mulch, and cut grass. A single glowing firebrand was never able to ignite any of the fuels. Four glowing 50 mm disk firebrands were able to initiate smoldering ignition for some of the fuel beds under external airflow.

Viegas *et al.* [33] conducted ignition tests using bark and pine cones as firebrands and six fuel beds of dried and live eucalyptus leaves, dried and live pine needles, hay, and straw. Experiments were conducted under ambient conditions. For a single glowing firebrand, no ignition occurred. No experiments of glowing firebrands under external airflow conditions were conducted.

Ellis [29] conducted experiments using glowing and flaming firebrands made of 500 mm long bamboo pieces. The moisture content of the fuel bed, eucalyptus litter, was varied from 4-21% and external airflow varying from 0 - 2 m/s was applied. Glowing firebrands only produced ignition for fuel beds with lower moisture contents. In general, fuel beds with higher moisture content required higher wind to produce ignition.

2.3.3 Firebrand Ignition of Solid Fuels

Early tests by Waterman and Takata [35] were the first experiments using firebrands on urban fuels. They found that ignition probability increased with increasing wind speed. An additional external heat flux was applied to act as a pilot ignition source. Dowling [31] conducted firebrand tests in bridge timbers and found that 7 g of firebrands were sufficient to produce ignition.

A series of experiments by Manzello *et al.* have been conducted on both a small and large scale using the NIST Dragon. In small-scale tests, they deposited glowing firebrands (between one and four total firebrands) in a cedar crevice. External airflows of 0.5 m/s and 1.0 m/s were applied. No ignition occurred [18]. In further experiments, four glowing firebrands were deposited into crevices made of either plywood or oriented strand board (OSB), both common building materials [36]. Ignition was sensitive to angle – only tests at 60° or 90° ignited. Additionally, of tests at these angles, only tests with 2.4 m/s external airflow and dry recipient fuel

ignited. The authors expected that the fuels with higher moisture content (i.e. 11%) did not ignite due to the higher thermal inertia of these samples [36].

Manzello *et al.* [37] provides an extensive summary of large scale experiments in Japan's Building Research Institute Fire Research Wind Tunnel Facility using the full-scale NIST Dragon. These experiments determined vulnerabilities of siding, roofing, and other portions of full structures that are susceptible to firebrand attack.

Santamaria *et al.* [30] conducted ignition tests on solid wood boards using a heat flux from a controlled source heater and piles of charcoal to simulate firebrands; however, charcoal was not found to simulate firebrands well. Heat fluxes from bark firebrands were taken on a vermiculate inert board and found to produce heat fluxes of up to 6 W/m^2 .

Chapter 3: Experimental Methodology

3.1 Overview

Several experiments were conducted to determine characteristics of piled firebrand behavior. There were three main objectives of this project, which produced three overall sets of experiments:

1. Calibration tests used to identify and quantify given measurement techniques
2. Heat flux tests with firebrand piles under ambient conditions
3. Tests under forced flow conditions to describe an ignition condition

Each set of experiments can be broken down into individual test configurations based on the measurement instruments used. This further breakdown of experimental sets will be described in each section. While the calibration tests were focused on the types of instruments to be used and correct quantification of heat flux, the other two sets of experiments measured quantities (i.e. temperature, heat flux, ignition) in relation to firebrand pile sizes. Table 3.1 shows the test matrix of the firebrand pile sizes in terms of diameter and mass used for each specific experiment.

Table 3.1: The test matrix. For each type of test, experiments were conducted using the diameter and masses of firebrands indicated. Note that the masses listed are initial mass before burning.

<i>Diameter</i>	Ambient	Ambient TS	Forced Flow	Ignition
	Water-Cooled	Calorimeter	TS	Experiments
	HFG	Experiments	Calorimeter	
	Experiments		Experiments	
6.35 mm	1 brand, 20 g, 50 g, 100 g	100 g	None	None
9.52 mm	1 brand, 20 g, 50 g, 100 g	100 g	None	None
12.7 mm	1 brand, 20 g, 50 g, 100 g	1 brand, 20 g, 50 g, 100 g	50 g, 100 g	50 g, 100 g

3.2 Calibration Tests

The specific measurement techniques chosen, as well as calibration results, are described in Chapter 4. The first objective of identifying a reliable method of measuring thermal characteristics necessitated the identification of a method of measuring heat flux from firebrand piles. An accurate instrument for measuring heat flux was difficult to find, as most heat flux measurements are focused on radiative fluxes. Three potential heat flux gauges were identified as options for our heat flux experiments: water-cooled heat flux gauges, thermopiles, and thin-skin calorimeters. For a full description of each instrument used, please see Chapter 4.

The water-cooled heat flux gauge is the most commonly used method for measuring heat flux in fire protection engineering research. The main concern with the use of a water-cooled heat flux gauge for this application was whether the water-cooling for the gauge would cool the firebrands. Testing whether cooling occurred was one subset of the calibration tests.

Thermopiles have the advantage of not requiring water-cooling; however, they can become fragile at high temperatures (including those temperatures expected from firebrand piles). Due to the stochastic nature of ignition, it was desirable to have an instrument sufficiently durable to withstand many repetitions of heat flux and ignition experiments. For this reason, a thermopile was not employed.

The thin-skin calorimeter is more durable than the thermopile and also does not require cooling, making it a potentially good option for firebrand pile experiments where heat fluxes are low enough that cooling could likely influence experi-

ments. Unlike water-cooled heat flux gauges and thermopiles, thin-skin calorimeters measure temperature which must be converted to heat flux via heat transfer calculations. An understanding of the energy balance for the complex heat transfer around the firebrand pile posed the largest challenge for using the thin-skin calorimeters for this application. Calibration of thin-skin calorimeters was the second subset of the calibration tests.

A thin-skin calorimeter is a calorimeter fabricated by welding a thermocouple to the backside of a thin metallic sheet. Given the properties (density, specific heat, thickness) of the metal, the thin-skin calorimeter can be used to measure heat transfer rates by calculating heat transfer components from a measured temperature history, using the assumptions of one-dimensional heat transfer and lumped capacitance. The test method is described in ASTM E459 [46].

ASTM E459 states one application of thin-skin calorimeters as “heat transfer measurements in fires and fire safety testing” [46]. A study by Hildalgo et al. [38] describes an application of thin-skin calorimeters for measuring incident radiant heat flux in large-scale fire tests. This study describes a method of calibration of thin-skin calorimeters meant to better account for uncertainties in the heat transfer calculations.

In order to determine whether the water-cooled heat flux gauge cooled firebrands, two sets of tests were conducted: one set with a 2.54 cm (1.0 in) Medtherm heat flux gauge and the second set with a smaller, 1.27 cm (1/2 in) Medtherm heat flux gauge. For both gauges, the measurement area is the same size; however, the cooling area is larger for the larger gauge. Both gauges were used for repetitions of

firebrand pile tests using a single brand and 50 g initial mass for three diameters of firebrands. Averages for each diameter and pile mass were calculated and the two gauges compared. Results can be found in Chapter 4, Section 4.2.1.

Initially, several methods were employed to attempt calibration of the thin-skin calorimeters. One method of conductive calibration was attempted. This method consisted of heating a copper slug in a propane flame until it was glowing and then placing the slug on the thin-skin calorimeter. This method was not continued because of uncertainty surrounding the contact resistance between the slug and the thin-skin calorimeter. Another method attempted was calibration using a cone calorimeter. Due to availability constraints on the cone calorimeter, a radiant heater was used for calibration following the method described below.

Ultimately, thin-skin calorimeters were calibrated following a method described by Hidalgo *et al.* [38]. The calibration used a radiant propane heater, a Dyna-Glo TT15CDGP 15,000, which attached onto the top of a propane tank. The heater was oriented vertically and placed directly facing a reference water-cooled heat flux gauge and the thin-skin calorimeter to be calibrated. In order to attain higher heat fluxes, the steel heat reflector was removed from the front of the heater. The reference gauge and the thin-skin calorimeter to be calibrated were set up using ring stands and were on a level vertically and horizontally. Additionally, it was critical that the surface of each gauge was the same distance from the heater. The gauges were set so that the center point between the gauges was in-line with the center of the radiant heater. Both the heater and the gauges were beneath a flow hood in order to exhaust products.

During calibration, the gauges were set as far back as possible to one side of the hood, while the radiant heater was set to the other side of the hood (see Figure 3.1). The radiant heater was kept on “High” for all calibration points and was moved closer to the gauges in order to increase the heat flux. Each position was kept constant for 10 min in order to account for the time lag of the thin-skin calorimeter and allow several minutes of constant readings. At the end of 10 min, the radiant heater was moved closer to the gauges by a few centimeters. This procedure was repeated until the radiant heater surface was as close as possible to the gauges without the gauges entering the thermal boundary layer of the heater. A total of five to fifteen radiative heat fluxes were used for each calibration.

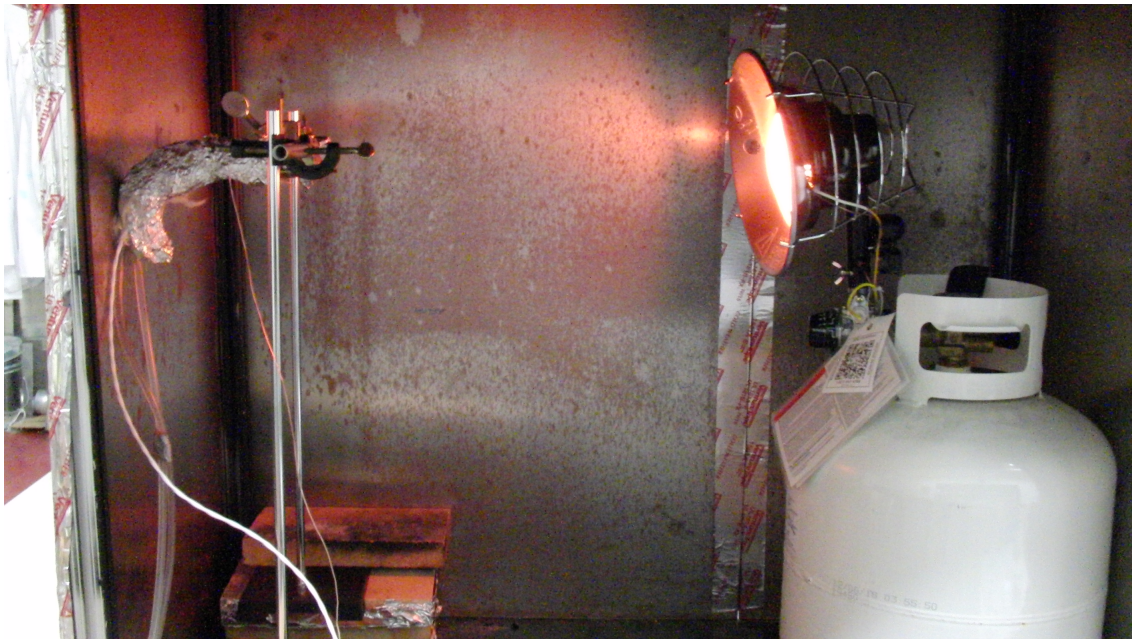


Figure 3.1: Side view photograph of radiant heater calibration set-up. The radiant heater is on the right side of the figure; gauges are set up on the left side of the figure.

Several thin-skin calorimeters were calibrated by this method in order to determine what differences, if any, there were between specific thin-skin calorimeters. A total of five thin-skin calorimeters with similar emissivity were calibrated and compared to determine a general calibration.

3.3 Heat Flux Tests With Firebrand Piles

The second overall set of experiments was to quantitatively determine the heat fluxes from firebrand piles and to test the calibration methods employed as part of the first set of experiments. For this set of experiments, two subsets of analogous tests (see test matrix in Table 3.1) were conducted: one using a water-cooled heat flux gauge and another using an array of thin-skin calorimeters. Using both methods of heat flux measurement allowed for a comparison of the two methods and a check for the thin-skin calorimeter calibration. These tests were all conducted on an inert ceramic insulation board in order to isolate the heat flux from the firebrand piles.

Experiments using thin-skin calorimeters provided spatial maps of the heat flux beneath the firebrand pile and indicated the total area heated by the firebrands, as well as heat fluxes later in the tests. Experiments with a single-point water-cooled heat flux gauge provided time-resolved heat flux measurement early in each experiment and were used to validate the thin-skin calorimeter calibration.

3.3.1 Experimental Design

Two experimental set-ups were built for heat flux tests, and differences in design arose out of the different size and shape requirements of the different sensors. Both set-ups, shown in Figure 3.2, were created by layering a 1.5 cm thick sheet of Superwool 607 High Temperature ceramic insulation board atop a 1.2 cm thick piece of plywood. The insulation board was used as an inert material and the plywood was used to provide a stabilizing mass for the set-up under wind. The insulation and plywood, which comprised the whole experimental board, were both 18 cm x 18 cm. Due to the sensitivity of the load cell and the ambient air movement of approximately 0.1 m/s, any overhang of the experimental board increased uncertainty in the mass measurements; thus, the size was chosen to match the size of the load cell test surface. Although no mass readings were taken during the water-cooled heat flux experiments, the set-up size was kept constant in order to decrease potential changes in airflow around the board.

In the thin-skin calorimeter set-up, sixteen sensors were arranged in a 4 x 4 array (see Figure 3.3) with the centers of the calorimeters separated by 1.5 cm, leaving 0.5 cm between the edges of adjacent thin-skins. The wires from the sixteen thin-skin calorimeters were threaded through the insulation and through drilled holes in the plywood, then secured onto the back side of the plywood. In this set-up, a Chromel-Alumel K-Type thermocouple with 30 gauge wire was placed on top of the insulation and secured using a small metal staple, so that the thermocouple bead was directly atop the insulation and in the middle of the array of thin-skins.

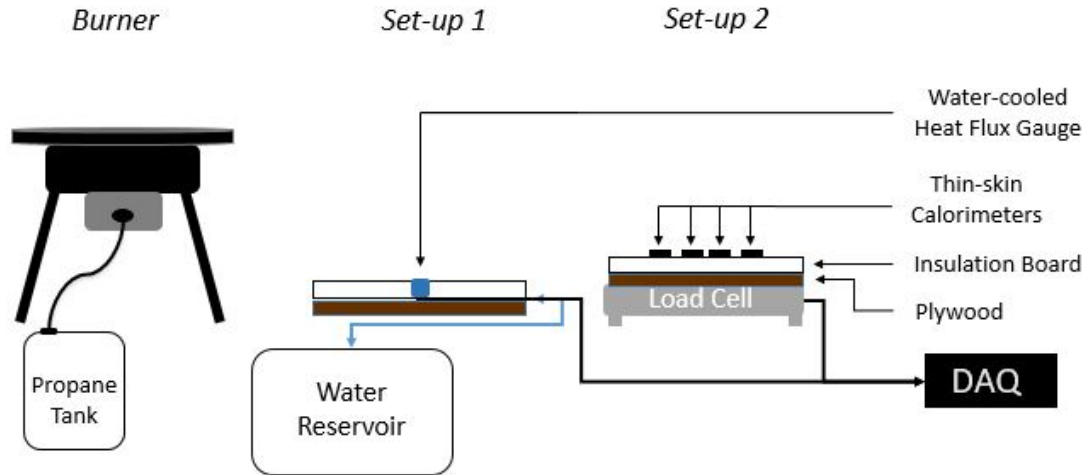


Figure 3.2: Schematic side view of both heat flux experimental set-ups with propane burner for fabricating firebrands. Figure of burner from Caton [3]. Not drawn to scale.

Thermocouples were fabricated in the laboratory using a HOT SPOT TC Welder spot welder. The thermocouple was placed on top of the insulation, beneath the firebrand pile. It measured the temperature of either the gaseous products within the firebrand pile or the temperature of a firebrand, if a particular firebrand landed on the surface of the thermocouple. Thus, the temperature measured is a ballpark pile temperature, but may experience variation based on how the firebrands in the pile land.

The entire set-up was placed on a load cell and inside a laminar flow hood for ambient experiments. The airflow in the laminar flow hood above the surface of the experimental board was measured to be 0.1 m/s using a hand held hot wire anemometer placed at several locations around the experimental sensors.

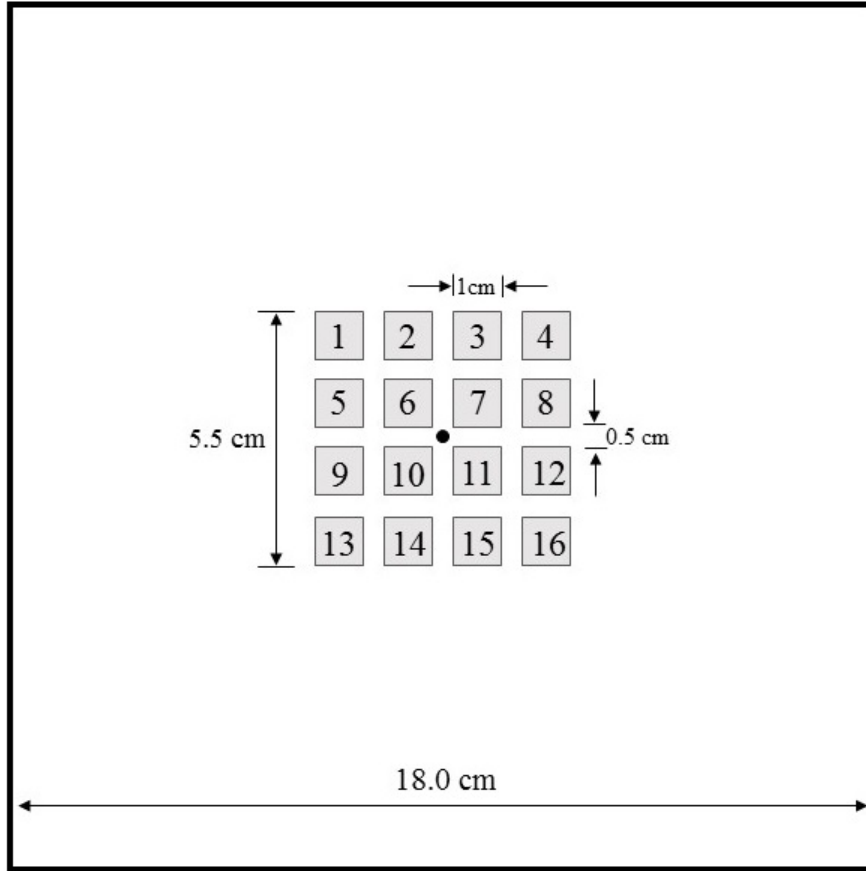


Figure 3.3: Top view of the experimental board using thin-skin calorimeters with reference numbering of calorimeters (drawn to scale). Thermocouple location shown in center of thin-skin array.

During thin-skin calorimeter heat flux experiments, a Mettler Toledo MS6002TS load cell with ± 0.01 g precision was used to measure the mass loss of the experiment. Despite this precision, ambient airflow caused the mass readings to fluctuate by approximately 1 g. Due to the low mass loss of the firebrand piles (on the order of 1 - 8 g) and the airflow fluctuations, reliable mass loss rates were not calculated.

For the water-cooled heat flux gauge experiments, the 1.27 cm Medtherm water-cooled heat flux gauge was used for this set of experiments. In the water-

cooled heat flux gauge set-up, a hole 1.27 cm in diameter, the size of the casing of the water-cooled heat flux gauge, was drilled into the wood and insulation board. The water-cooled heat flux gauge was placed directly in the center of the insulation board. The tubes from the gauge were L-shaped and were secured to the top of the plywood beneath the insulation for stability of the gauge. Water tubes for cooling were connected to a pump in a 15 gal water storage tank. A thermocouple was placed in the water tank in order to ensure a consistent cooling source was provided. In both this set-up and the previous set-up, a video camera recorded the experiment from an elevated side view.

3.3.2 Wood Properties and Firebrand Production

Birch wooden dowels were used to produce firebrands used in all tests. For these experiments, cylindrical dowels of three diameters, 6.35 mm, 9.52 mm, and 12.7 mm, were cut to 25.4 mm in length. While firebrands come in different shapes and sizes – disks or bark pieces, needles, and sticks – collection studies by Manzello *et al.* [39] found that cylindrical sticks are one of the most common brand shapes. Although Santamaria *et al.* [30] also found bark to be a common firebrand, sticks are more reproducibly simulated. Diameters and length were chosen because they were near the average size based on collection studies and because of the availability of dowel sizes. Although 12.7 mm diameter firebrands may be larger than average, this provided the ability to compare over a range of diameters (from 6.35 mm to 12.7 mm). It is important to note that these diameters represent the initial diameters of

the wood; however, the diameters of the burned firebrands are smaller. See Caton [3] for representative proportions of diameter decrease in wooden dowels.

All dowels were birch, which was chosen in this study as it was readily available in the sizes of firebrands typically observed in WUI fires; however, its density is slightly higher than that of softwoods more commonly found in WUI fires (approximately 600 kg/m^3 in comparison to the $350\text{-}530 \text{ kg/m}^3$ density range of softwoods [40]). Wood was dried at $103 \pm 2^\circ\text{C}$ in a VWR Gravity Convection Oven per ASTM Standard D4442 [41]. Drying was complete when the mass of the sample steadied within $\pm 0.1 \text{ g}$ for three consecutive hours, when measured on a Mettler Toledo NewClassic MF load cell (Model # MS32001L) with accuracy $\pm 0.1 \text{ g}$. Moisture content (MC) was also measured using an A&D MF-50 moisture content analyzer. Dried wood was placed in one gallon plastic bags with drierite to keep it from regaining moisture between drying and testing. The wet-basis MC of the samples was in the range of $0 \pm 0.5 \%$.

In order to test the effect of smoldering firebrands on recipient fuels, it was necessary to devise a method to repeatably produce smoldering firebrands. Previous studies using firebrands have used a variety of methods of producing brands, but many focus on flaming rather than smoldering brands. Of those studies that used glowing firebrands, methods used to produce smoldering firebrands were either not repeatable or difficult for use in producing a pile of firebrands. Previous firebrand production methods are discussed in Section 2.3.1.

Several fabrication methods were tested to determine the most repeatable method of producing smoldering firebrands. Initially, wooden dowels were placed in

a 12 cm x 16.5 cm x 11 cm Thermolyne furnace (Type 1400) at a set temperature between 300-450°C for a given time between 5-30 min. (The temperatures and times were varied to determine if a given temperature-time combination would produce a pile of glowing firebrands.) Although one to two dowels typically glowed at their tips, most dowels were either charred or had turned to ash when removed from the oven. It was determined that the oven did not provide sufficient oxygen for the dowels to reach a smoldering state [21].

Another method tested for producing firebrands was heating on a Corning PC-600D Hotplate. Dowels were deposited on the hot plate and turned occasionally. Imaging using a Seek Thermal IR camera determined that the hot plate did not provide even heating to the brand surface. Additionally, the highest temperature produced by the apparatus (550°C) did not provide sufficient heat for the wood to smolder. It was determined that exposure to flames would likely be necessary to produce smoldering and would more realistically replicate exposure during a wildland fire.

In order to best simulate a real fire exposure, dowel pieces were exposed to flames. Initially, dowels were put in a small metal bowl with 5 mL of heptane or ethanol; however, though the dowels flamed, they did not continue glowing after the flames ceased. Ultimately, the dowels were exposed to a propane flame. All dowel pieces to be used in a given test were put in a wire mesh basket which was set on a Bunsen-type burner over a propane flame (e.g. for a test of 25 g of 6.35 mm brands, all 25 g would be exposed to flame simultaneously). The flame height was kept constant, so that it touched the bottom of the basket in every test. The flame

was turned off after all of the brands had visibly ignited, approximately 150-200 s. After the cessation of flaming, glowing firebrands were deposited on the test set-up. Another method of extinguishing was tested, in which the flames were manually extinguished by placing the firebrands in a metal box with a hole drilled in the top to allow smoke to escape. It was found that brands were more reproducibly formed in a glowing state when they self-extinguished. This firebrand production procedure was kept constant throughout all of the tests.

Although this firebrand production method was repeatable to conduct, there were certain associated uncertainties. Larger quantities of firebrands flamed for longer periods of time after the burner was turned off. As a result, larger piles of firebrands may have been in a more degraded state upon deposition than smaller piles or single firebrands. It is uncertain whether these differences produced any discernible differences in the data recorded.

3.4 Experimental Procedures

A set of experimental procedures was developed for each type of test, depending on the instruments used and the flow conditions (forced flow or ambient). All general procedures were kept the same for all types of tests. After the experimental board was in place, firebrand production was begun. Once the burner was turned off, data acquisition was initiated in order to capture ambient conditions before the test began. Data acquisition used in each test is listed in Table ???. Glowing firebrands were deposited on the test board, and data acquisition was continued until

measured parameters decreased below a set threshold, specified for each instrument used. For tests in ambient conditions, both the propane burner and the test board needed to fit under the laminar flow hood, while forced flow and ignition experiments were conducted in a large burn room with overhead exhaust capabilities. Due to the proximity of the propane burner to the test set-up in the ambient configuration, the flaming of the firebrands elevated baseline temperatures of the thin-skin calorimeters and thermocouples to approximately 30°C before the tests began.

3.4.1 Firebrand Pile Tests Using Thin-Skin Calorimeters

Before beginning each test using the thin-skin calorimeter array, each calorimeter was tested to determine that it had not broken. This procedure was undertaken because the thin-skin calorimeters were fragile – sometimes the attachment of the wire to the metal broke. Testing was conducted by exposing each calorimeter to a small butane flame and checking whether it increased in temperature as expected.

To begin the experiment, firebrands were placed onto the thin-skin calorimeter array after they ceased flaming. For tests with single firebrands, tongs were used to move the firebrand from the wire mesh basket and to set it directly atop Thin-Skin Calorimeter 6 (see Figure 3.3). For piles, glowing firebrands were poured onto the center of the test set-up from the side of the wire mesh basket, using a large pair of tongs as a guide. Once the firebrands were deposited on the test set-up, tongs were used to push the firebrands to the center of the board if they had fallen to the side. For larger piles of 6.35 mm firebrands, a few glowing brands sometimes decreased

in diameter sufficiently to fall through the holes in the mesh. When this occurred, those firebrands were not later placed on the pile.

After firebrands were deposited on the test board, the pile was left, and data was recorded until the thermocouple and thin-skin calorimeters decreased below 27°C. This cut-off temperature for thermocouples was used because heat fluxes calculated at this temperature were small. At this point, data acquisition was stopped. The firebrand remnants, char and ash, were swept off the test board using a small piece of cardboard, and the sensors were cleaned of debris using compressed air.

3.4.2 Firebrand Pile Tests Using Water-Cooled Heat Flux Gauge

For tests using a water-cooled heat flux gauge, water tubes were connected to the gauge and the pump was placed in the 15 gal water storage container and allowed to cycle water for two to three minutes before firebrand production began. For tests using a single firebrand, the brand was placed directly atop the center of the sensor. For piles, the same procedure was followed as for the thin-skin calorimeter array. Data acquisition was stopped when the heat flux gauge no longer registered any external heat flux.

After each test, the gauge was checked to see if any paint had been discolored or scratched. If significant changes occurred, the heat flux gauge was repainted and re-calibrated, as described in Section 4.2. In order to ensure that the firebrands on top of the sensor did not damage the gauge, re-calibration was conducted after the first five heat flux tests were finished. Both the old and new calibration coefficients were

applied to voltage measurements on the final test, so that the effect of calibration could be determined. The results of this comparison are shown in Figure 3.4. The differences in the heat fluxes produced by the different calibration coefficients were within the uncertainty of the tests. The procedure was repeated again after fifteen more tests. Again, the effect on heat flux was sufficiently small.

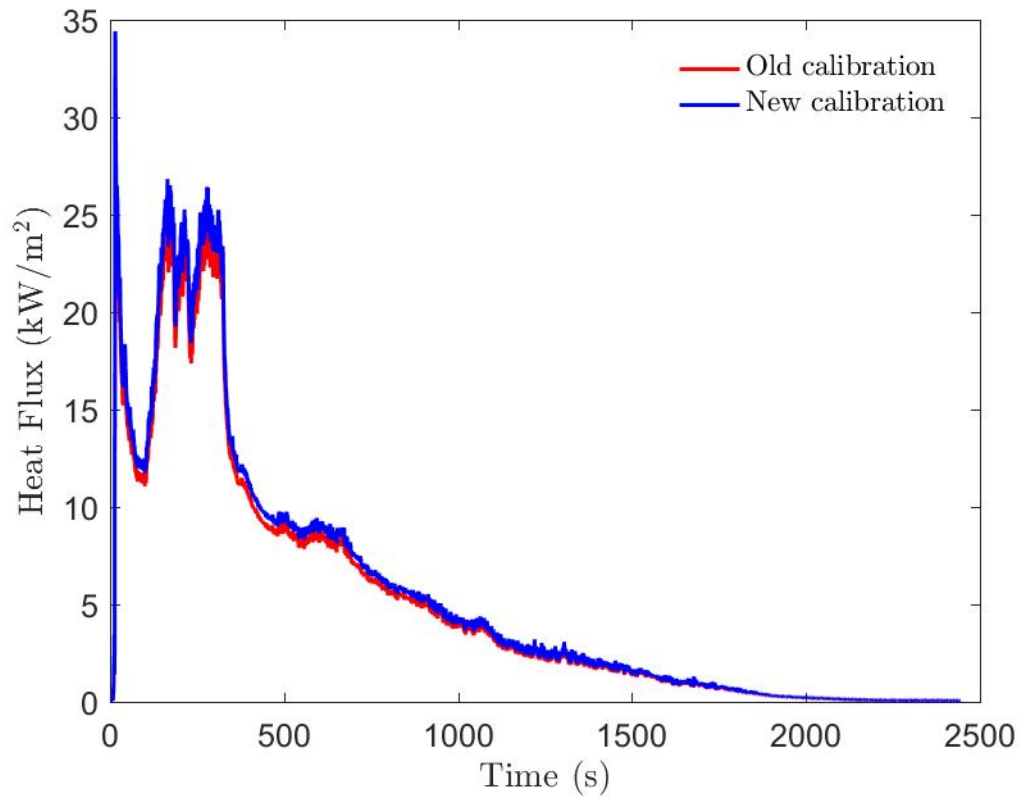


Figure 3.4: Comparison of heat flux calculated using initial calibration and new calibration after five tests of 12.7 mm firebrands with a 50 g initial pile mass.

3.5 Tests Under Forced Flow Conditions

The objective of conducting tests under forced flow was to describe a specific ignition condition. The application of wind was necessary to aid ignition, as preliminary tests of flaming ignition of a recipient fuel under ambient airflow conditions were not successful. Again, two subsets of tests were conducted. The first subset was a series of ignition tests using firebrand piles on a recipient fuel which were conducted to determine time to ignition and the necessary wind velocity and pile size to produce flaming ignition. The second subset was a series of heat flux measurements on an inert board using the same external conditions as were used to produce ignition. This second subset of experiments was conducted to isolate the thermal characteristics that occurred immediately preceding ignition.

3.5.1 Ignition Test Set-up

The experimental set-up for the ignition tests was fairly straightforward. A 6.35 mm thick aluminum plate with a super elliptical leading edge (described in [42]) was placed several centimeters in front of the outlet of the wind tunnel. The aluminum plate allowed for the formation of a laminar boundary layer before the firebrand test section. In the ignition tests, an 18 cm x 18 cm sheet of oriented strand board (OSB) was placed behind the aluminum edge, flush with its surface. (The analogous thin-skin calorimeter set-up shown in Figure 3.6 shows the orientation of the aluminum plate in relation to the wind and experimental set-up.)

OSB was used in these tests because of its common usage as a building material, often used as sheathing for walls and roofing. It has also been used for ignition tests in other studies [36]. OSB was dried at $103 \pm 2^\circ\text{C}$ in a VWR Gravity Convection Oven, following the same procedure as was used to dry the wood for firebrands. As described previously, dried wood was placed in gallon plastic bags with drierite to keep it from regaining moisture between drying and testing. Drying the wood was important, as many studies have found that the ignition of recipient fuels (including woods and plastics) is sensitive to the MC of the fuel [18, 33, 36, 43].

Preliminary ignition tests were conducted under ambient conditions to determine whether flaming ignition could be achieved. Firebrand pile sizes up to 100 g initial mass (10 g deposited mass) of 12.7 mm firebrands were tested; however, no piles achieved flaming ignition, though most achieved smoldering ignition. The largest diameter firebrand were used because results by Hadden *et al.* [2] and Manzello *et al.* [18, 34] found that larger hot objects are more likely to produce ignition.

Subsequently, tests under forced flow were conducted. These experiments were conducted in front of the outlet of a laminar blower, the characteristics of which are described in Singh and Gollner [44]. A series of tests was conducted in which the pile mass was kept constant (100 g initial of 12.7 mm firebrands) and the wind velocity was increased from 0.85 m/s to 1.98 m/s. These tests were used to identify an ignition condition (wind velocity and pile size) which would reliably transition to flaming ignition. The repeatable ignition condition for a flat sheet of OSB with surface area 18 cm x 18 cm was 1.84 m/s wind velocity and 100 g initial mass of

12.7 mm firebrands. This wind speed is consistent with average wind speeds found in fires (e.g. 1.8 m/s in the New Jersey Pine Barrens prescribed burns [45]).

A video camera recorded experiments at 29 fps (frames per second) from an elevated side view, angled downward towards the experiments and allowing coverage of the thin-skin calorimeter array to be determined. A FLIR ThermCAM SC3000 infrared camera (IR) camera with a spectral response of 8-9 μm recorded IR video from directly above the set-up and recorded in the temperature range of 350-1500°C. This range was chosen to cover the initial high temperatures of the firebrands. The emissivity of the firebrands was unknown, though previous researchers have used values between 0.6 - 1.0 [7]. A value of 0.92 was chosen; however, IR results were meant to give a qualitative rather than quantitative view of heating from the top of the pile.

For these tests, three wood configurations were compared: a flat board analogous to that used for heat flux tests, an L-shaped configuration with the vertical board of the L perpendicular to the wind direction, and a crevice of width 5 mm and depth 26 mm with the crevice perpendicular to the wind direction. These last two configurations simulate the edge of a home where the deck meets the wall of a house and decking boards, respectively. The crevice sizes correspond to typical configurations [1]. Both of these configurations are known to be particularly susceptible to firebrand accumulation [37]. All three ignition configurations with relation to the wind direction can be seen in Figure 3.5.

Before testing, the mass of the OSB sample was taken so that total mass loss could be calculated. Firebrands were deposited in the middle of the OSB sample

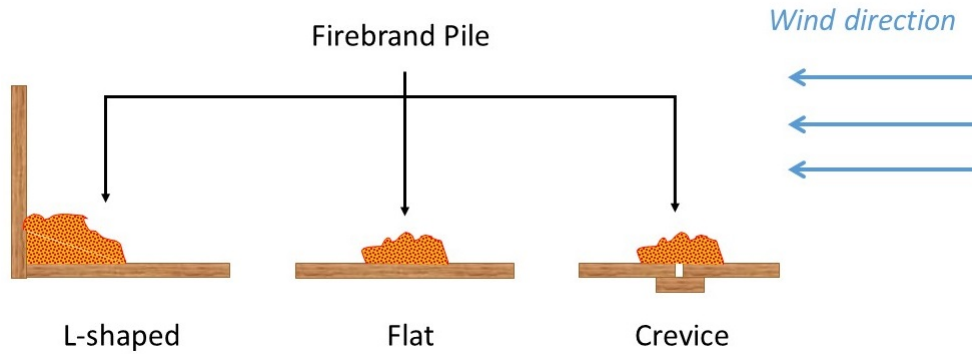


Figure 3.5: Schematic of recipient fuel configurations oriented with respect to wind direction.

for both the flat and crevice samples, and in the corner of the L-shape, for the L-shaped sample. Tests were continued until the IR camera registered no variation in temperature between the sample and surrounding area. After testing finished, the firebrands were removed from the OSB by tapping gently on the edge of the OSB, and the final mass of the OSB sample was taken.

3.5.2 Thin-Skin Calorimeter Forced Flow Experiments

Heat flux tests using thin-skin calorimeters were also conducted under the forced flow conditions found to produce ignition. Figure 3.6 shows the experimental set-up for the wind tunnel experiments. The experimental board was the same board used in the ambient tests. The procedures for checking the thin-skin calorimeters before testing were the same. An additional step to prepare for experiments was to focus the IR camera. In order to do this, a metal bracket was heated using a butane blow torch and then placed on the experimental board beneath the IR camera. The camera was then focused from the computer until the metal bracket

was clear. Otherwise, all procedures for the testing were the same. The wind tunnel was turned on and set to the correct velocity at the same time as the data acquisition was begun. Again tests were stopped when thin-skin calorimeter readings decreased below 27°C.

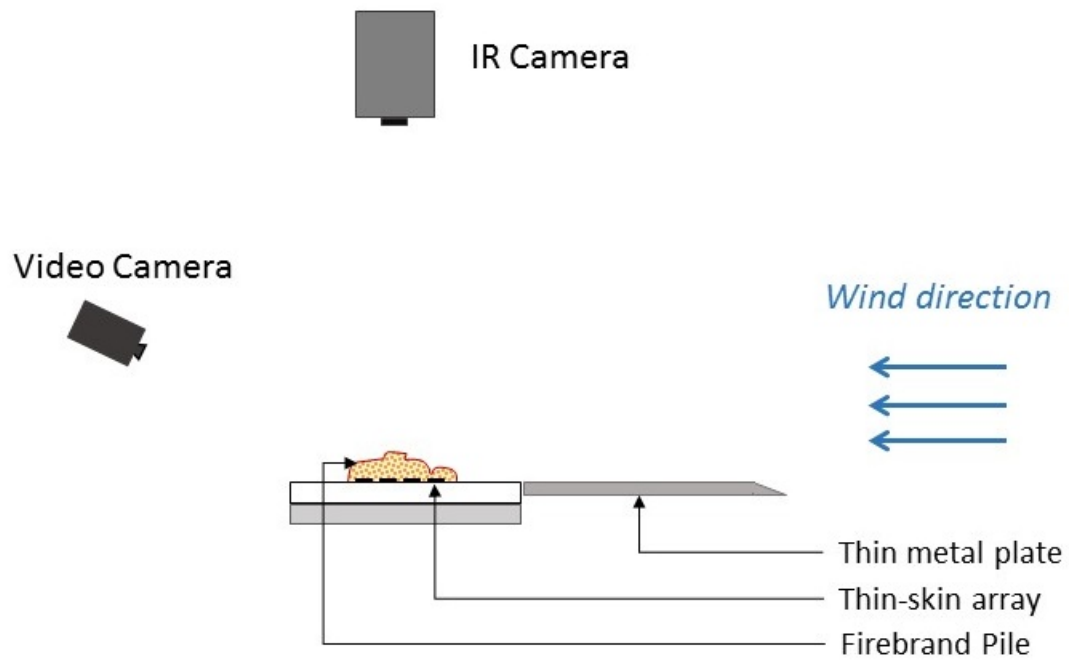


Figure 3.6: Schematic side view of wind tunnel set-up for thin-skin calorimeter heat flux tests, showing direction of wind and angles of cameras. Not drawn to scale.

Chapter 4: Measurement Techniques and Calibration Results

4.1 Overview

Two sets of experiments were described in the previous chapter: firebrand pile tests using a water-cooled heat flux gauge and using thin-skin calorimeters and ignition experiments. Key quantities were acquired for the different experiments: temperature, heat flux, visual observations, and mass. Two measurement methods were used to obtain temperatures: thermocouples and an IR camera. Likewise, two measurement methods were used to acquire heat flux: thin-skin calorimeters and a water-cooled heat flux gauge. During all tests using thin-skin calorimeters, thermocouples also measured temperature of the firebrands. A load cell was used for thin-skin calorimeter tests under ambient conditions. Video recording was taken of all experiments,

4.2 Heat Flux: Water-Cooled Heat Flux Gauge

As a result of the uncertainties associated with the use of thin-skin calorimeters, a water-cooled heat flux gauge was also used to measure heat flux during these experiments. The water-cooled heat flux gauge was a 1.27 cm (1/2 in) Medtherm

GTW-7-32-485A heat flux transducer. The water-cooled heat flux gauge had a linear calibration with voltage and was re-calibrated on a cone calorimeter against a reference gauge. In preliminary experiments, a 2.54 cm Medtherm heat flux gauge was also used; however, this gauge was not used during any experiments described in the Results section.

4.2.1 Results of Gauge Size Comparison

Initially, a larger heat flux gauge of 2.54 cm diameter was used to conduct preliminary tests. Due to a sharp drop-off in heat flux after an initial high peak, it was determined that the water cooling of the heat flux gauge could potentially be cooling the firebrand piles, particularly for smaller mass tests, such as those using a single firebrand.

A comparison of 50 g tests (shown in Figure 4.1) using both the 2.54 cm and 1.27 cm water-cooled heat flux gauges show that the heat fluxes measured by the larger gauge are all lower than the average heat flux of the two gauges, while the smaller gauge recorded higher heat fluxes over the entire test length. It was inferred that cooling at these high masses would indicate even more cooling at lower mass piles. At longer times for larger piles (e.g. after 500 s), it is possible that some local cooling could occur as the mass and temperature of the pile decrease; however, it is expected that the cooling will be decreased with the smaller gauge.

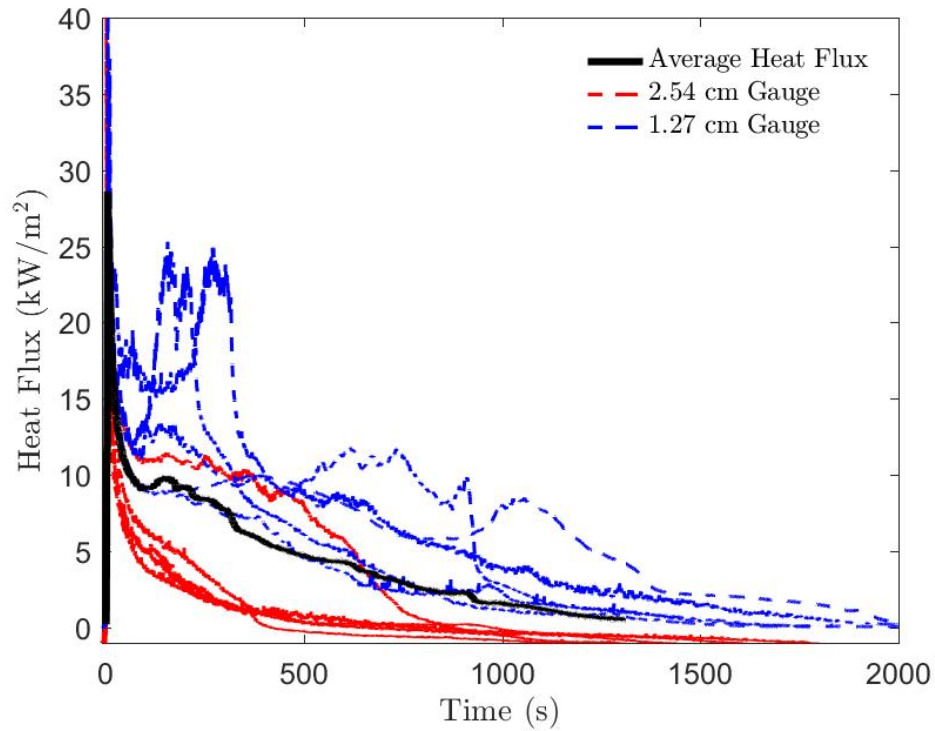


Figure 4.1: Comparison of heat fluxes measured for a 50 g initial mass 12.7 mm diameter firebrand pile.

4.3 Heat Flux: Thin-Skin Calorimeters

Thin-skin calorimeters were used to measure the spatial distribution of heat flux beneath the firebrand piles. Because the thin-skin calorimeters were fabricated and calibrated in-house, the following sections provide details on the fabrication, calibration, and method of calculating heat flux from the temperatures measured on the backside of the thin-skin calorimeters.

4.3.1 Fabrication

Thin-skin calorimeters were fabricated using 0.25 mm K-type wire and Inconel alloy 625, a nickel-chromium alloy, used for its high thermal-fatigue strength and melting temperature above 1290°C [47]. The thermocouple wires were welded to the back surface of the calorimeter using a HOT SPOT TC spot welder used to make thermocouples. Wires were spaced 1.6 mm apart in accordance with ASTM E459 [46]. The area of the calorimeter surface was 1 cm². It was important to decrease the area of the thin-skin surface because the calculation of heat flux from a thin-skin calorimeter uses the assumption of lumped capacitance. The thickness, δ , of the Inconel was 0.508 mm. ASTM E459 [46] provides an equation to calculate the optimum thickness for the calorimeter:

$$\delta_{opt} = \frac{3}{5} \frac{k(T_{max} - T_0)}{q} \quad (4.1)$$

where k is the thermal conductivity of the thin-skin calorimeter in W/mK, T_{max} is the maximum temperature of the thin-skin calorimeter in K, T_0 is the initial temperature, and q is the heat flux in W/m². An average thermal conductivity value was taken by averaging the values of k at the maximum and initial temperatures (values found in [47]). A maximum temperature of 760°C was chosen as a typical average maximum value for large pile tests and an initial temperature of room temperature, 21°C, was used. The k values for these temperatures are 20.8 W/m°C and 9.8 W/m°C, respectively [47]. Results of tests using the water-cooled heat flux gauge found maximum heat fluxes around 60 kW/m². When these values are

substituted into Equation 4.1, a value of 0.113 m (113 mm) for δ_{opt} is found. The δ_{opt} value is based on optimizing the maximum exposure time; however, because the sensors continued to measure heat fluxes comparable to the water-cooled gauge throughout experiments, it was assumed that exposure time was sufficient for this application.

As the optimum thickness is unrealistic for the small-scale experiments, metals of three thickness (1.27 mm, 0.8128 mm, 0.508 mm) were compared for accuracy and time response. These thicknesses were chosen based on availability. Thin-skin calorimeters of all thicknesses tested produced similar heat flux readings when tested in a cone calorimeter at a set heat flux; however, the thicker calorimeters had a slower time response, making the thinnest calorimeter more useful for transient readings. Although the 0.508 mm thick calorimeters produced the shortest time response, the thickness of the calorimeter is on the order of the diameter of the thermocouple wire, introducing an additional potential error.

After fabrication, thin-skin calorimeters were exposed to a butane blow torch flame for five minutes in order to tarnish the surface of the metal. Flame exposure was conducted because the metal naturally became tarnished when the thin-skin calorimeters were beneath the firebrand pile. Because the emissivity of the metal was expected to change when it became tarnished, the metal was exposed before testing in an attempt to keep the emissivity fairly constant between early and late tests. One large source of uncertainty was the emissivity of the tarnished metal. This uncertainty was accounted for by using a correction factor in the calculation of heat flux, described in Section 4.3.3.

For preliminary tests, the surface of the thin-skin calorimeter was painted using Zynolyte[®] Hi-Temp paint with a known emissivity of approximately 0.94 [48]. Due to issues obtaining additional paint from the same manufacturer, this paint was not available for the thin-skin calorimeters used in the majority of experiments. Medtherm high temperature optical black coating, also of emissivity 0.94, was briefly tested as a potential substitute; however, the paint underwent a reaction when in contact with the firebrands, changing color and, thus, emissivity. As a result, the tarnished thin-skins with unknown emissivity were used for all experiments described in the Results section. Emissivity may change with temperature for this metal; however, the temperature dependence is also unknown.

4.3.2 Calibration

The ASTM E459 standard [46] describes the use of thin-skin calorimeters in radiative and convective environments. Even in these environments, calibration is necessary to ensure that the calorimeters produce accurate heat fluxes. Hildalgo *et al.*, for example, show the initial discrepancies between a known incident radiant heat flux and heat fluxes measured by a thin-skin calorimeter [38]. Uncertainties regarding the heat flux readings arise out of the difficulty of not having a complete knowledge of all of the components of the heat transfer processes. In particular, the thin-skin calorimeter heat transfer is calculated with assumptions of lumped capacitance, one-dimensional heat transfer, known material properties, and a constant emissivity [46]. In order to account for these uncertainties, thin-skin calorimeters

were calibrated using a radiant propane heater. A cone calorimeter was used once as a comparison, but this method was not used extensively enough to provide a solid calibration.

The calibration with the radiant heater required that the thin-skin calorimeter be oriented in a vertical position, while the thin-skin calorimeters in the test array were oriented horizontally. This difference has an effect on the convective losses from the gauge. Although the Nusselt number correlation was changed for the vertical and horizontal orientations, an additional calibration was conducted using a cone calorimeter. Two thin-skin calorimeters were calibrated using this method. In this calibration, a reference water-cooled heat flux gauge and the thin-skin calorimeter to be calibrated were placed adjacent to one another beneath the center of the cone. For one calibration, the thin-skin calorimeter was calibrated separately at two point heat fluxes. For the other calibration, one thin-skin calorimeter was calibrated at seven heat fluxes from 3-53 kW/m², chosen to cover the range of heat fluxes expected. In the first calibration, a painted thin-skin calorimeter was used; however, the second calibration was for a tarnished thin-skin calorimeter, similar to those used in the tests. Use of the radiant heater allowed a greater number of gauges to be calibrated, thus providing a larger sample size for comparison.

There are still uncertainties associated with this calibration method. It uses an incident radiant heat flux; however, the calorimeters are exposed to conductive heat fluxes as well during the firebrand experiments. A method for conductive calibration was not developed for comparison. Additionally, in the vertical set-up, there is a significant convective component. On the other hand, in the experiment,

the assumption is made that, during firebrand pile tests, convective losses from covered thin-skin calorimeters are negligible.

4.3.3 Theoretical Formulation

Rather than measuring heat flux, the thin-skin calorimeter measures temperature, which can then be used to calculate heat flux. An equation for the total heat flux from the firebrand pile to the thin-skin calorimeter can be found by conducting an energy balance on a control volume of the thin-skin calorimeter, as shown in Figure 4.2.

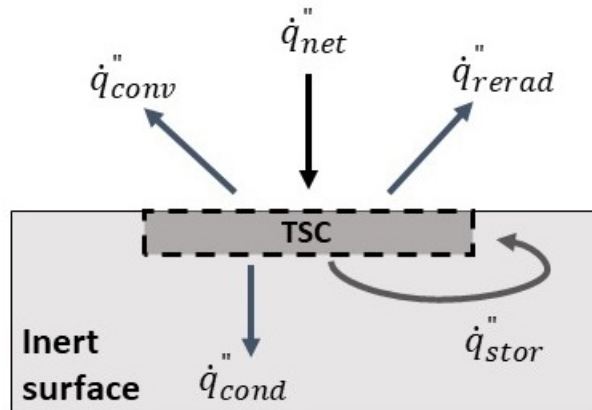


Figure 4.2: Energy balance around control volume of a single thin-skin calorimeter.

$$\dot{E}_{stor} = \dot{E}_{in} - \dot{E}_{out} \quad (4.2)$$

where \dot{E}_{in} denotes the energy flux into the control volume and \dot{E}_{out} denotes the energy flux out of the control volume. Using Equation 4.2 for a general energy balance and the heat transfer terms from Figure 4.2 produces the heat transfer balance shown in Equation 4.3.

$$\dot{q}''_{net} - \dot{q}''_{conv} - \dot{q}''_{rerad} - \dot{q}''_{stor} - \dot{q}''_{cond} = 0 \quad (4.3)$$

where \dot{q}''_{net} is the net heat transferred into the thin-skin calorimeter from the firebrand pile, \dot{q}''_{conv} is the energy transferred away from the thin-skin calorimeter via natural convective cooling, \dot{q}''_{rerad} is heat reradiated from the thin-skin calorimeter to the environment (or to the firebrand pile), \dot{q}''_{stor} is stored heat, and \dot{q}''_{cond} is heat conducted through the thin-skin calorimeter to the wire and insulation, with all quantities measured in W/m².

Convective cooling occurs from the thin-skin calorimeter array to the environment via

$$\dot{q}''_{conv} = h(T_{TS} - T_{\infty}) \quad (4.4)$$

where h is the convective heat transfer coefficient in W/m²K, T_{TS} is the temperature of the thin-skin calorimeter in K, and T_{∞} is the ambient air temperature in K.

The thin-skin calorimeter radiates heat following the Stefan-Boltzmann Law:

$$\dot{q}''_{rerad} = \varepsilon\sigma(T_{TS}^4 - T_{\infty}^4) \quad (4.5)$$

where ε is the emissivity of the Inconel metal and σ is the Stefan-Boltzmann constant.

The heat storage rate is defined as

$$\dot{q}''_{stor} = \rho c_p \delta \frac{dT}{dt} \quad (4.6)$$

where ρ and c_p are the density (in kg/m³) and specific heat (in J/kg K), respectively, of the Inconel metal, both provided as a function of thin-skin calorimeter temperature in [47], and δ is the thickness of the thin-skin calorimeter in m.

A correction term is calculated in place of the conductive heat transfer rate to the surrounding insulation. This correction term is assumed to be a fraction of the incident radiative heat flux as it should be small and both are assumed to be temperature dependent. The correction thus also takes into account that the emissivity of the tarnished metal is unknown, as is the conduction. The correction heat rate is calculated as:

$$\dot{q}''_{cond} = C\alpha_{TS}\dot{q}''_{rerad} \quad (4.7)$$

where C is the C-factor as a function of temperature found by calibration as described in 4.3.2, α_{TS} is the absorptivity of the Inconel metal.

Another method of calculating the correction factor is presented in Hidalgo, *et al.* [38]:

$$\dot{q}''_{cond} = C\alpha_{TS}\dot{q}''_{rerad} \quad (4.8)$$

where $\dot{q}''_{inc,rad}$ is the incident radiant heat flux in W/m² calculated as

$$\dot{q}''_{inc,rad} = \frac{1}{\alpha_{TS}(1-C)} [\dot{q}''_{stor} + \dot{q}''_{rerad} + \dot{q}''_{conv}] \quad (4.9)$$

following Equation 11 from [38]. In this case, the C-factor method of calculating \dot{q}''_{cond} is used because the conduction into the wires is unknown, the temperature of the insulation board is unknown, as is the final emissivity of the Inconel metal.

When the expressions from Equations 4.4 - 4.8 are substituted into Equation 4.3 (with the expression for $\dot{q}''_{inc,rad}$ substituted into the expression for \dot{q}''_{cond} , the following expression for \dot{q}''_{net} can be found:

$$\dot{q}''_{net} = \frac{1}{1 - C} [\dot{q}''_{stor} + \dot{q}''_{rerad} + \dot{q}''_{conv}] \quad (4.10)$$

4.3.4 Results of Calibration

The purpose of the calibration was to find a correction factor which could be applied to the heat flux calculations in the experimental use of the thin-skin calorimeters. The C described in the previous sections was found following the method of Hidalgo *et al.* where

$$C = \frac{\alpha_{TS}\dot{q}''_{inc} - \dot{q}''_{losses}}{\alpha_{TS}\dot{q}''_{inc}} \quad (4.11)$$

where \dot{q}''_{inc} is the incident heat flux measured by the reference water-cooled heat flux gauge. This term differs from $\dot{q}''_{inc,rad}$, which is theoretically what a reference gauge would measure during an experiment, whereas \dot{q}''_{inc} is what the reference water-cooled heat flux gauge measures during the calibration.

$$\dot{q}''_{losses} = \dot{q}''_{stor} + \dot{q}''_{rerad} + \dot{q}''_{conv} \quad (4.12)$$

which are calculated as described in the Section 4.3.3, previously.

The correction factor was applied to the \dot{q}''_{cond} term, which could better be described as a correction term to take into account the uncertainties associated with the emissivity of the Inconel when tarnished and the conduction into the insulation and into the wires of the thin-skin calorimeter. A comparison of the corrected

net heat flux, \dot{q}_{net}'' , was plotted against \dot{q}_{inc}'' to determine the effectiveness of the correction factor. An example of such a plot is shown in Figure 4.3.

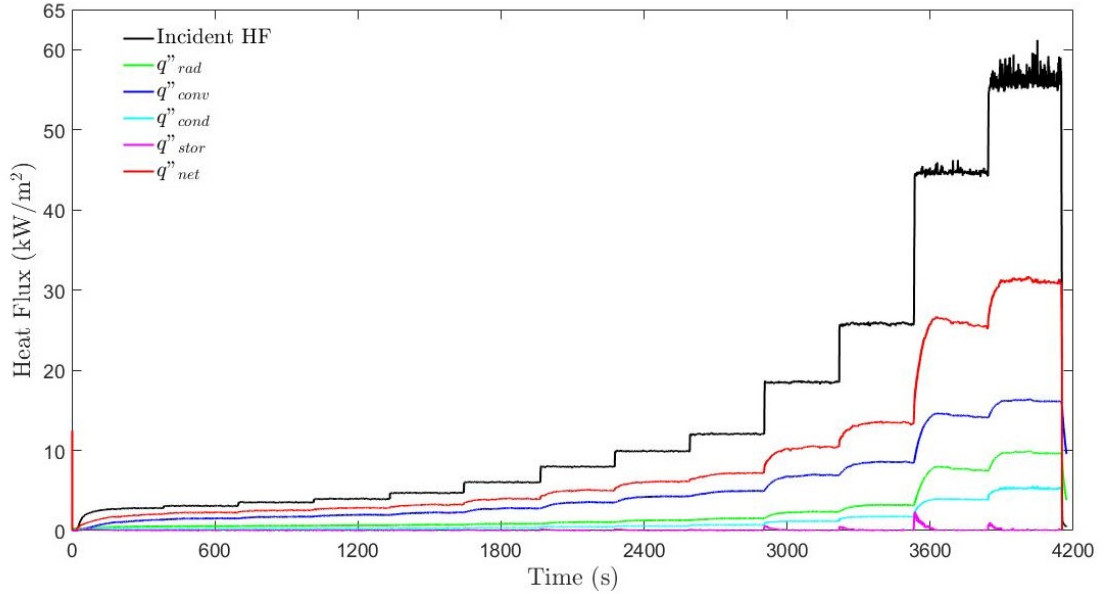


Figure 4.3: Components of heat flux for one radiant heater thin-skin calorimeter calibration test.

It is clear that the correction factor does not adequately correct to the full incident heat flux in this environment. This difference is caused by the use of a correction based on reradiation, rather than the incident heat flux. As a result, the thin-skin calorimeter measurements are taken only as a qualitative indication of trends; however, it is important to note that, even were the incident radiant heat flux used to calculate the correction, the results would still only be qualitative due to uncertainties that will be discussed in further sections. A comparison of different C-factors found that the dependence on C-factor is so great that minor changes have a large impact on the total correction. Due to the uncertainty in the calibration, the heat flux calculated using the correction factor is expected to have

a high uncertainty. The problems and uncertainties associated with the calibration will be discussed further in the Conclusions and Future Work, Chapter 8.

The correction factor was plotted as a function of temperature and fitted in order to get C as a function of temperature to apply during the calculation of heat flux in experiments. For the fit, the spike at the low and high temperatures were disregarded. These spikes occurred when the calibration data recorded ambient temperatures after the rest of the calibration was finished.

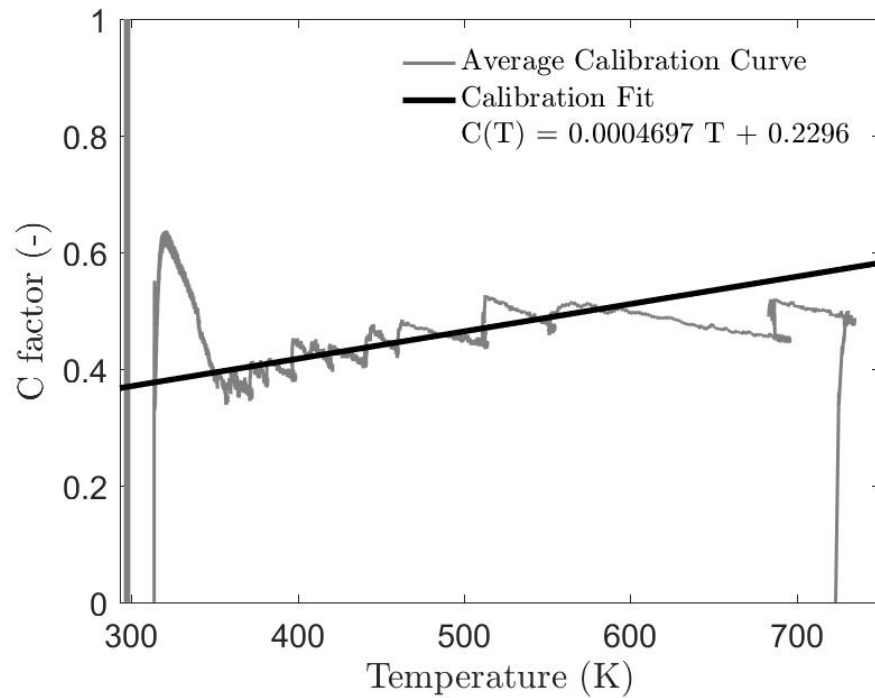


Figure 4.4: Linear fit to correction factor.

4.3.5 Application of Calibration to Experiments

Due to the uncertainties associated with the calibration method, the heat flux values obtained using the thin-skin calorimeters have potentially high uncertainties.

Comparison with results from the water-cooled heat flux gauge is used to show that, despite the uncertainty, heat flux values from the thin-skin calorimeters follow similar trends. As a result, the important contribution of the thin-skin calorimeter data is the illustration of qualitative trends and spatial heating.

The thin-skin calorimeters measured temperature as a function of time. A plot of the time-dependent temperature for all sixteen thin-skins calorimeters in the array can be seen in Figure 4.5. This figure and subsequent figures will be shown of a single test of 12.7 mm diameter firebrands with a deposited pile mass of 9.6 g.

Using these temperatures, heat flux as a function of time was calculated for each individual thin-skin calorimeter. The total heat flux was calculated as:

$$\dot{q}''_{net} = \dot{q}''_{rerad} + \dot{q}''_{stor} + \dot{q}''_{cond} \quad (4.13)$$

where \dot{q}''_{rerad} , \dot{q}''_{stor} , and \dot{q}''_{cond} are calculated as described in Section 4.3.3, and \dot{q}''_{cond} is the correction term using the C-factor found via calibration.

Convective losses were not considered for the firebrand pile experiments, except during single brand experiments, as most sensors were blocked for part of the test. Later in the test, as firebrands turned to ash, it is likely that convective cooling occurred. Additionally, convective losses from the sensors were certainly present for exposed sensors. Considering these losses negligible could potentially result in lower net heat fluxes later in the test and for exposed thin-skin calorimeters. Figure 4.6 shows the raw heat flux calculated using the thin-skin temperatures for the same test shown in the previous figure.

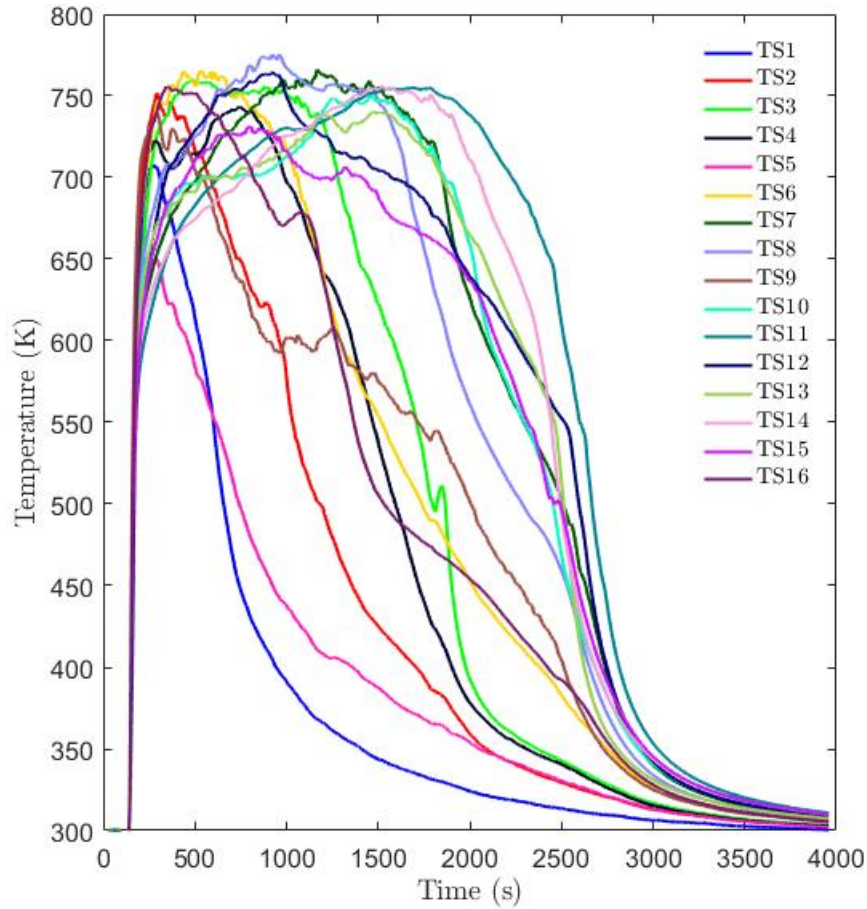


Figure 4.5: Thin-skin calorimeter temperature as a function of time for 16 thin-skinned in array. Thin-skin calorimeter locations can be found in Figure 3.3.

The water-cooled heat flux gauge results were used to help determine the accuracy of the thin-skin calorimeter measurements. Figure 4.7 shows a plot of the average heat fluxes measured using the water-cooled heat flux gauge for a test of the same pile size and diameter firebrand as shown previously for the thin-skin calorimeters. Figure 4.8 shows a magnified version of Figure 4.7 to capture the long-time behavior.

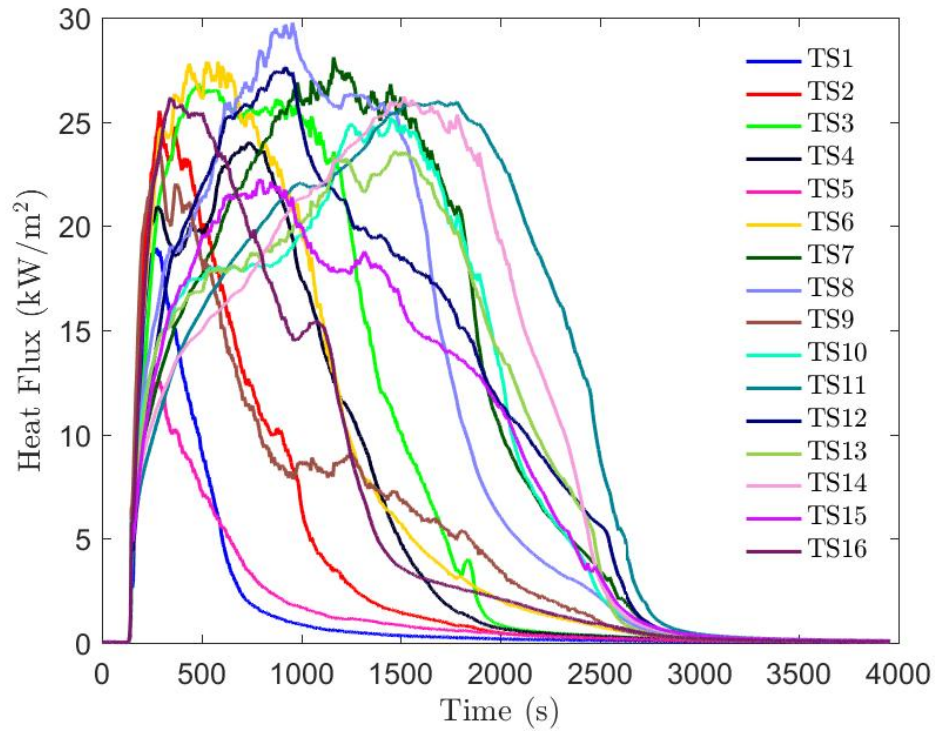


Figure 4.6: Total heat flux imparted to the thin-skin calorimeters, calculated using measured thin-skin calorimeter temperatures.

In order to compare thin-skin calorimeter heat flux results with those obtained using the water-cooled heat flux gauge, time averages were taken of the covered thin-skins for each test. A further description of this procedure can be found in Chapter 5, Section 5.4. Figure 4.9 shows this comparison between heat flux measured by the thin-skin calorimeters and heat flux measured by the water-cooled heat flux gauge. The averages are taken over five test repetitions for the water-cooled heat flux gauge and over nineteen test repetitions for the thin-skin calorimeters in this particular configuration.

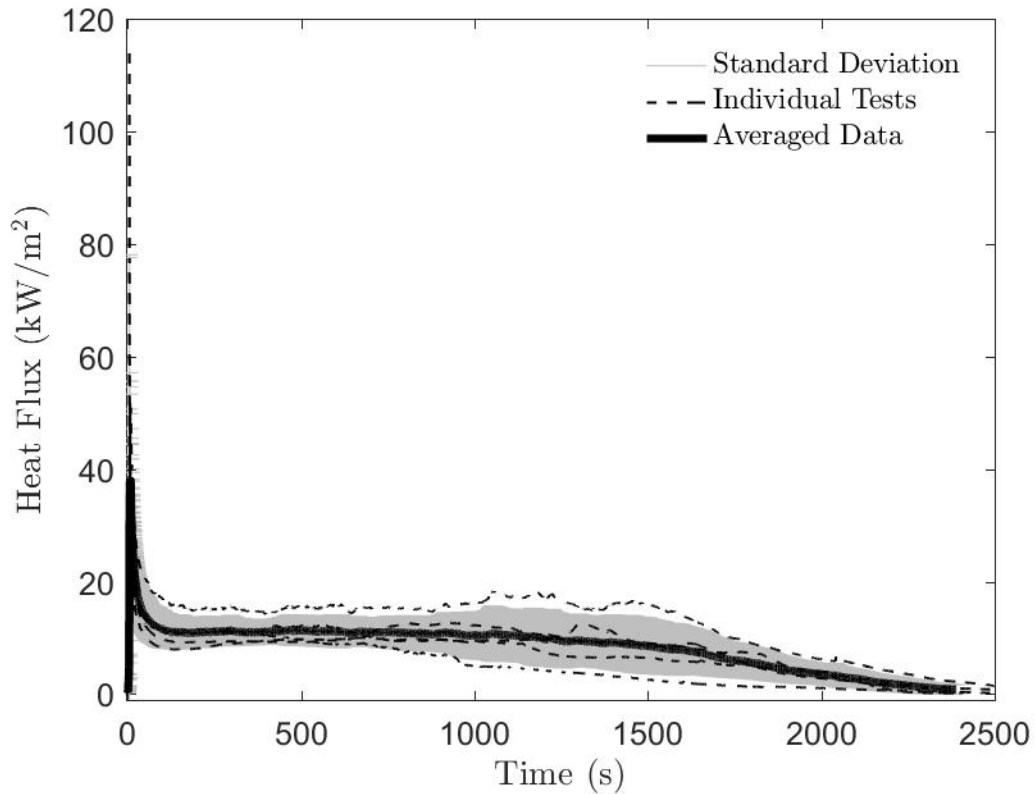


Figure 4.7: Averaged heat flux results for a 12.7 mm diameter firebrand, 9.6 g deposited mass pile, measured using the water-cooled heat flux gauge.

Figure 4.9 shows a representative trend comparison between the two heat flux measurement methods that can be seen in all pile sizes except the single brand. The water-cooled gauge peaks early, then drops to a steady value, before decreasing again at the end of the test as the firebrands cool. The thin-skin calorimeters peak later in the test, which is consistent with the slower time response. They sustain a higher heat flux value than the water-cooled heat flux gauge for the rest of the test.

The lower heat flux from the water-cooled heat flux gauge could be consistent with potential cooling or the difference in heat transfer between a cold object (the gauge) and hot object, as opposed to the thin-skin calorimeters, which increase in

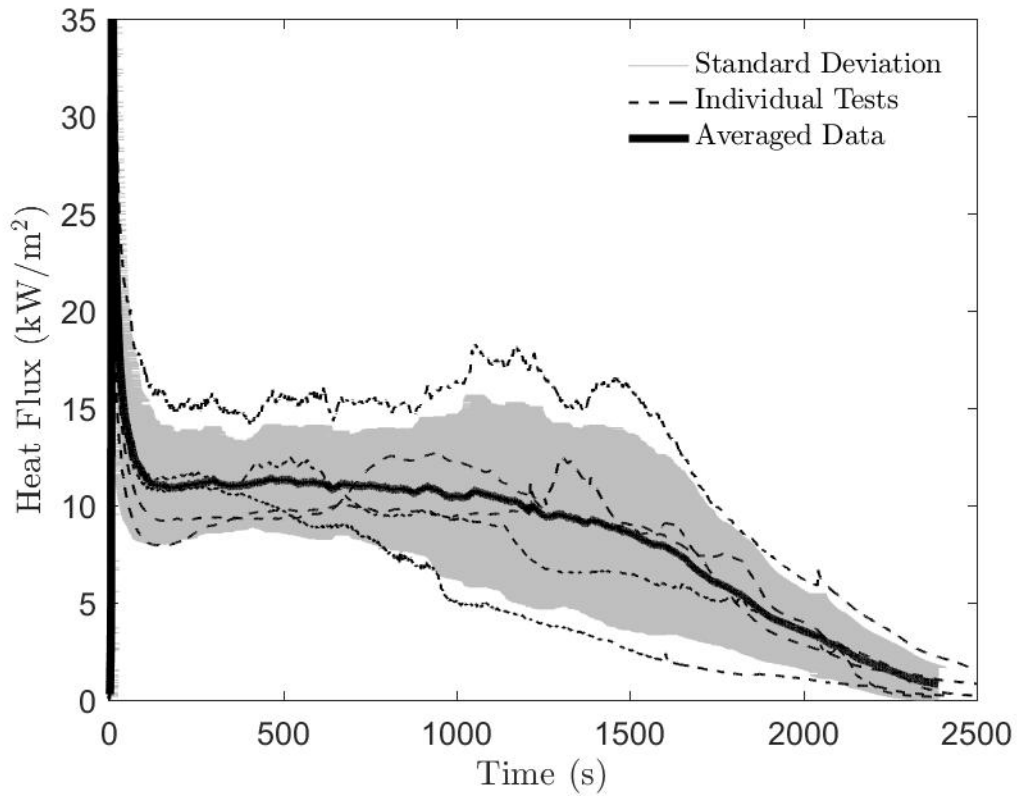


Figure 4.8: Magnified replication of previous figure of averaged heat flux results for a 12.7 mm diameter firebrand, 9.6 g deposited mass pile, measured using the water-cooled heat flux gauge, showing long-time trends.

temperature throughout the duration of the test. Despite the problems with the calibration, the thin-skin calorimeters read heat fluxes broadly comparable to those measured using the water-cooled heat flux gauge.

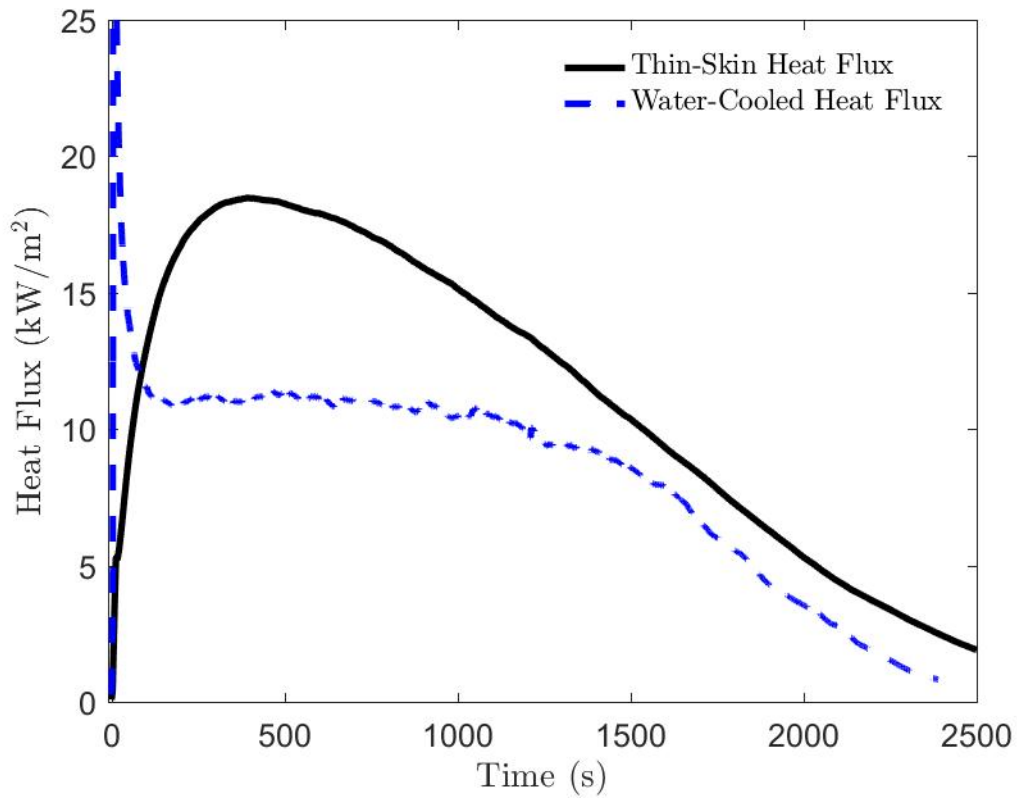


Figure 4.9: Plot of averaged heat flux over all repetitions for a 12.7 mm, 9.6 g test to compare heat fluxes obtained using thin-skin calorimeters and the water-cooled heat flux gauge.

Chapter 5: Results of Firebrand Pile Tests

5.1 Overview

Several types of data were acquired throughout the different categories of tests, as described in Chapter 4. Firebrand pile tests under ambient conditions were conducted using both thin-skin calorimeters and a water-cooled heat flux gauge. The main results obtained for both sets of tests are heat flux versus time curves. Results obtained using the thin-skin calorimeter array also included temperature measurements from the thermocouple and thin-skin calorimeter and spatial distributions of heat flux over the entire array. Initial time series heat flux curves were presented at the end of Chapter 4. Results in this chapter will include visual observations, the thin-skin calorimeter and thermocouple temperatures, components of heat flux measured by thin-skin calorimeters, spatial distributions of heat flux, and methods of comparing heating from piles.

5.2 Visual Observations

Visual observations provided interesting information regarding the burning of firebrand piles. Although all of the firebrands were fabricated together, there

were differences between firebrands even when they were first deposited on the test board. Some firebrands appeared to be mostly charred, while others glowed completely throughout the entire brand. The most common behavior was glowing at both tips of the firebrand. The varieties of glowing can be seen in Figure 5.1, which shows single firebrands and firebrand piles immediately after deposition on the experimental board.

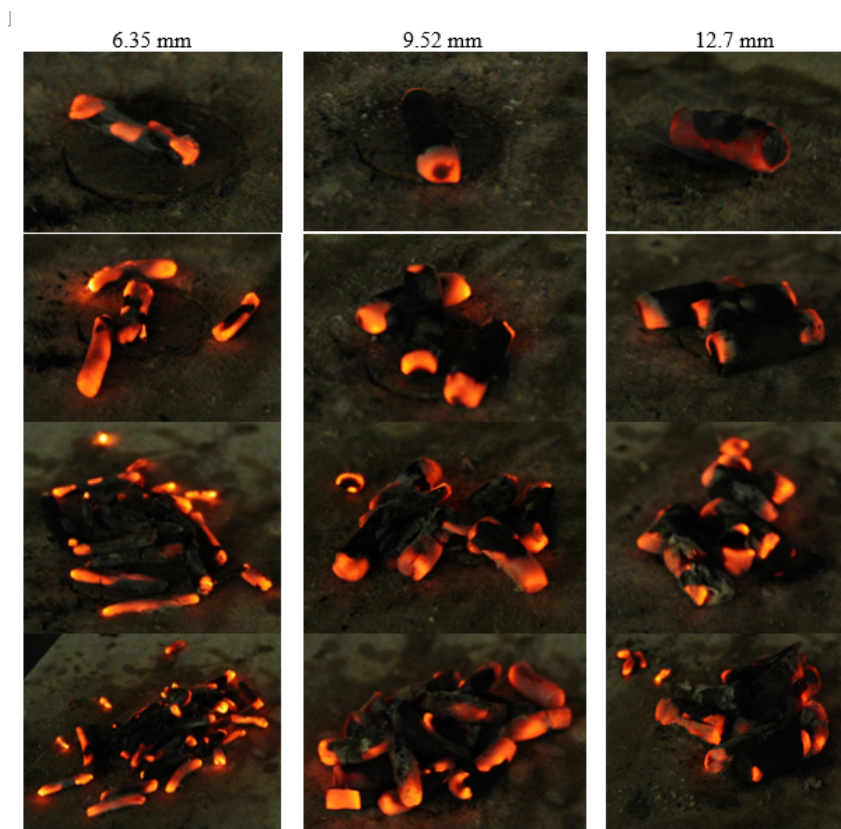


Figure 5.1: Image sequence showing varying firebrand pile sizes, increasing in diameter from left to right and increasing in pile mass from top to bottom.

Though firebrands were at first deposited in a glowing state, they quickly transitioned to ash in many tests. The beginnings of this transition can be seen in Figure 6.2 in the following chapter. In many cases, the entire top of the pile would

turn to ash, which can be seen in Figure 6.4 in the following chapter. It was assumed that the ash indicated that the test would be coming to an end; however, the ash was later thought to insulate hotter glowing cores of firebrands. This phenomenon was especially apparent in wind tunnel tests. At times the wind blew away sections of ashy material revealing glowing firebrands beneath. This behavior may explain differences in temperature measured by the IR camera, a surface thermocouple, and the thin-skin calorimeters.

5.3 Thermocouple and Thin-Skin Calorimeter Temperature Results

Both the thin-skin calorimeters and a thermocouple measured temperatures during the thin-skin calorimeter tests. The temperatures measured by these two instruments are compared in order to determine whether the thin-skin calorimeters can provide a realistic spatial distribution of temperature beneath the firebrand pile.

Figures 5.2–5.4 show three methods of comparing the temperatures obtained by the thermocouple and the thin-skin calorimeters. The figures show a 9.6 g deposited mass pile of 12.7 mm diameter firebrands under ambient conditions. Figure 5.2 shows the temperatures from all sixteen thin-skin calorimeters alongside the temperature from the thermocouple as a function of time.

It is clear from Figure 5.2 that the thermocouple experiences a much faster time response than the thin-skin calorimeters. This result is expected, as the time response of the thermocouple should be approximately 10 s, based on the wire gauge, and the response of the thin-skin calorimeters was found to be on the order

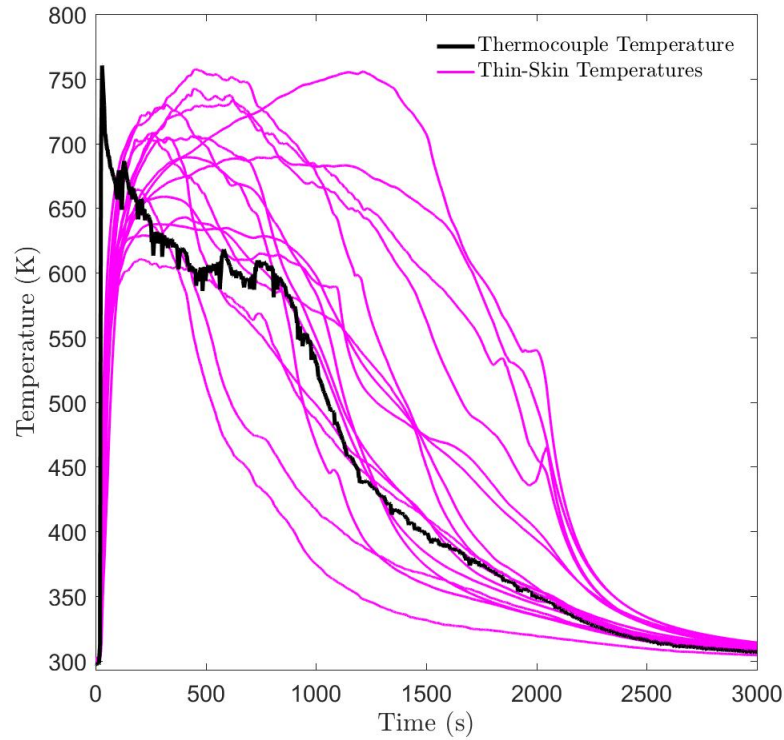


Figure 5.2: Temperature as a function of time as measured by thin-skin calorimeters and thermocouple beneath 12.7 mm diameter firebrand pile of 9.6 g deposited mass. of 100–150 s. The thin-skin calorimeters also continue reading high temperatures for a much longer period of time. There are two potential reasons for this behavior. First, the thin-skin calorimeters are larger and thus store more heat. Second, as different parts of the firebrand pile heat and cool, the thermocouple may not always be in the optimum location to measure the pile temperature. It is relevant to note that peak temperatures from the thin-skin calorimeters and from the thermocouple are similar.

In order to obtain a clearer picture of the heating in the pile, the thermocouple temperature was plotted with the temperatures of the four surrounding thin-skin

calorimeters. These results are shown in Figure 5.3. This figure shows similar trends to the previous plot (Figure 5.2) of all thin-skin calorimeter temperatures; however, in this case, two of the thin-skin calorimeters nearest to the thermocouple follow almost the same temperature trend as the thermocouple itself. The thin-skin calorimeters with this general trend do not capture the same peak temperature, but capture the same cooling behavior.

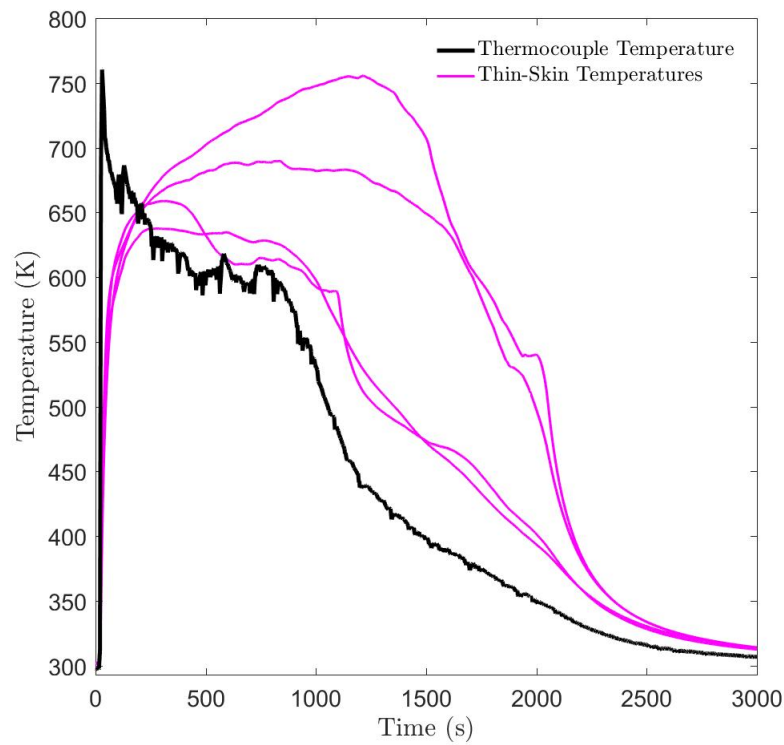


Figure 5.3: Temperature as a function of time as measured by the thermocouple and its four immediate nearest thin-skin calorimeters for a 12.7 mm diameter firebrand pile of 9.6 g deposited mass.

Figure 5.4 shows a further comparison of temperatures using the averaged temperature for all covered thin-skin calorimeters in this test. Although peak tempera-

tures are not captured, the thin-skin calorimeters capture the general temperature trend. This trend suggests that thin-skin calorimeters may function as a relatively accurate representation of the temperature beneath a firebrand pile at long times. As a matter of fact, the thin-skin calorimeters could provide more accurate surface temperatures than they do heat fluxes.

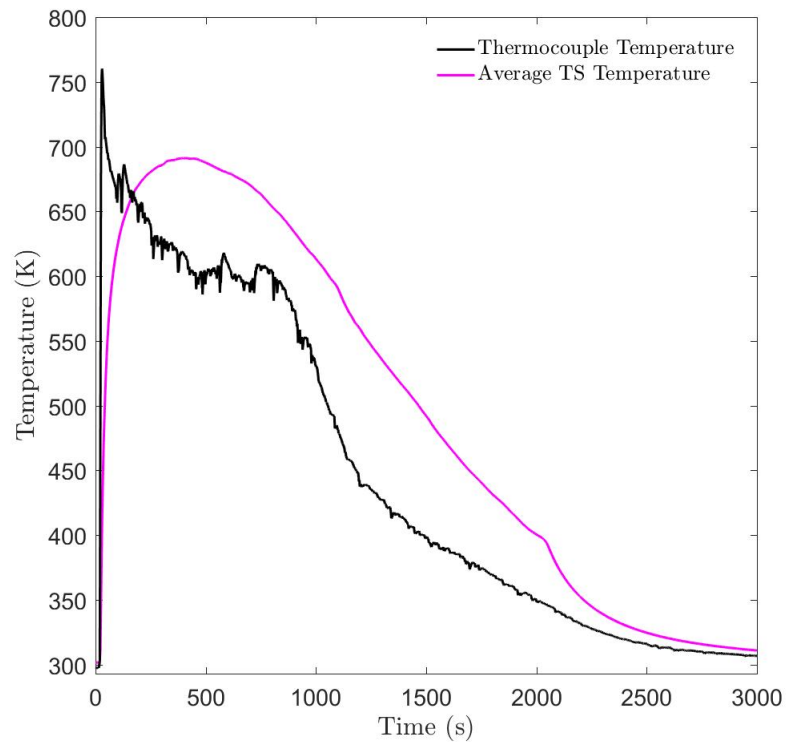


Figure 5.4: A comparison of temperature as a function of time for the thermocouple and an average temperature of the thin-skin calorimeters initially covered by the firebrand pile for a 12.7 mm diameter firebrand pile of 9.6 g deposited mass.

5.4 Heat Flux Results

Different aspects of the heat flux measurements show important trends. Using the thin-skin calorimeter data, we can see the relative magnitude of the different heat transfer components. The thin-skin calorimeters also provide a spatial distribution of heat flux as a function of time throughout the test. Finally, comparisons can be drawn between the methods of measuring heat flux.

5.4.1 Components of Heat Transfer

In order to calculate net heat flux imparted to each individual thin-skin calorimeter, individual components of heat flux were calculated as functions of time and summed. Figure 5.5 shows the components of heat transfer for a single thin-skin calorimeter central to a large firebrand pile. These values give an example of the approximate magnitudes of heat flux components calculated for piles. Re-radiation plays an important role in the heating, which is consistent with the high temperatures and glowing observed. Unfortunately, the conduction correction term dominates, indicating that the thin-skin calorimeters can be subject to large errors given the high dependence of the correction term on individual heat transfer components (e.g. radiation). This calibration may then compound uncertainty in the emissivity value.

Convection losses were not included when calculating the net heat flux for piled configurations as most sensors were covered; however, convection was added to the calculations for a single firebrand, as this configuration left most of the thin-

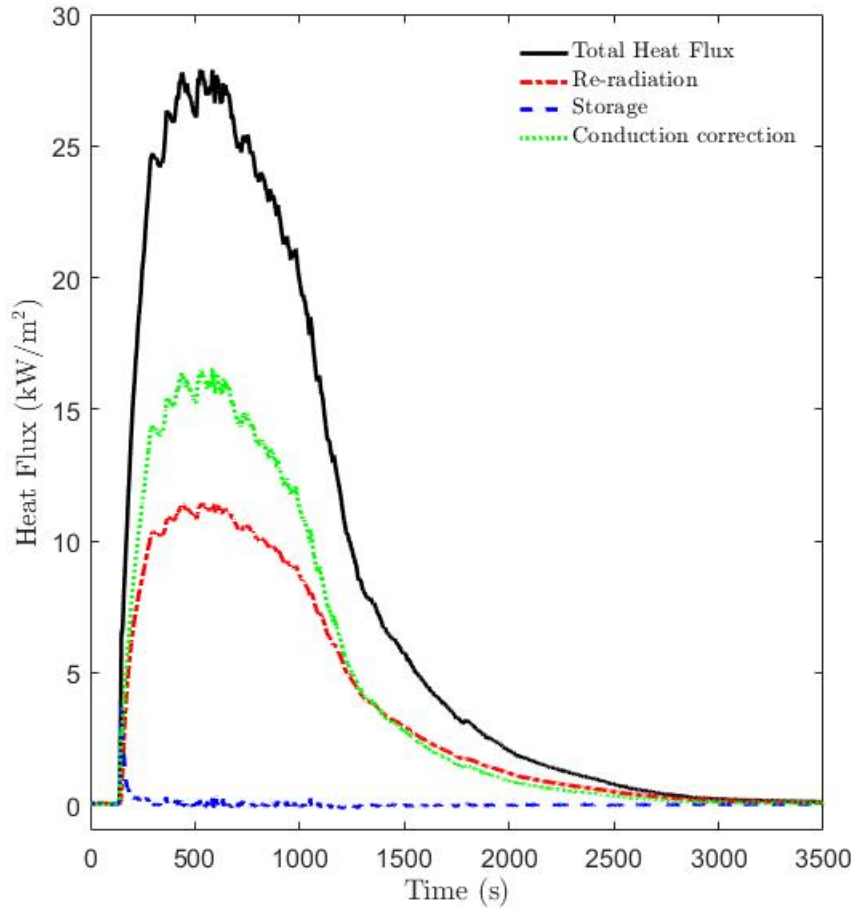


Figure 5.5: Components of heat transfer for a single thin-skin calorimeter during a piled test.

skin array exposed. Figure 5.6 shows a similar plot of heat flux components for a test using a single 12.7 mm firebrand. Here convective losses form the main portion of the heat transfer, though re-radiation is also important.

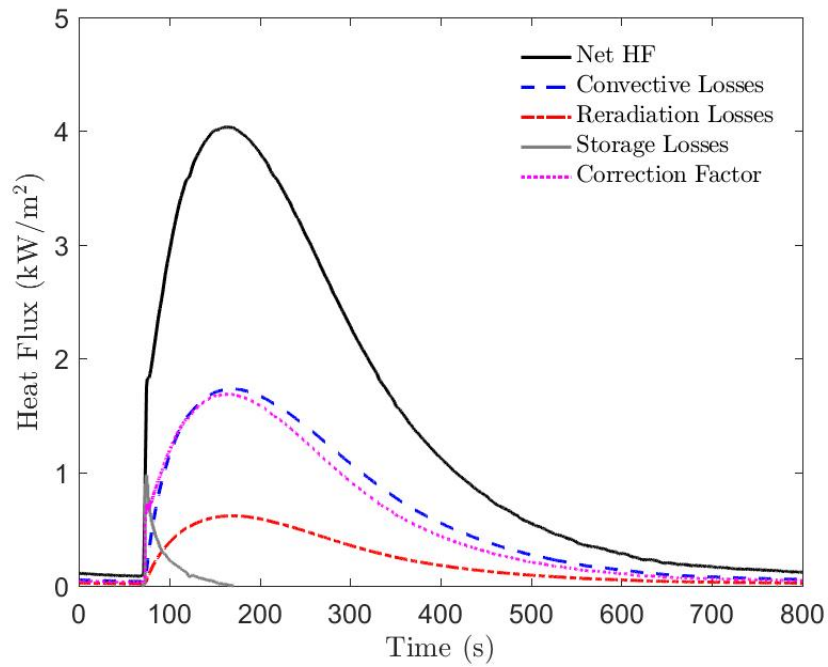


Figure 5.6: Components of heat transfer for the covered thin-skin calorimeter of a single firebrand test.

5.4.2 Spatial Distribution of Heat Flux

Figure 4.6 in the previous chapter shows a wide distribution of heat flux behaviors for different thin-skin calorimeters. Some thin-skin calorimeters reach a peak heat flux and drop off quickly, while others sustain a peak heat flux for over 500 s. Some calorimeters also peak later in the test. In order to understand these trends, video data was analyzed to determine which thin-skins were completely covered by firebrands at the beginning of the test, which were partially covered by firebrands, and which were completely exposed or not covered at all. Figure 4.6 was re-plotted

as Figure 5.7 showing which thin-skin calorimeters fell into each of these categories of coverage.

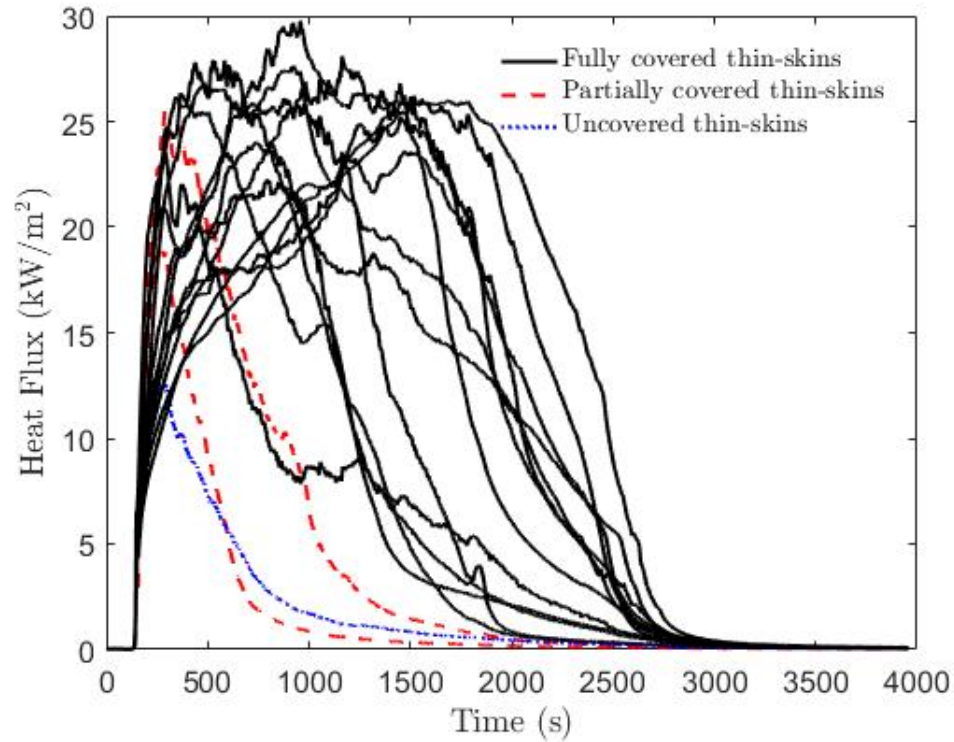


Figure 5.7: Heat flux as a function of time for a 12.7 mm diameter, 9.6 g deposited mass test, measured using the thin-skin calorimeter array with coverage of thin-skins denoted.

The majority of the array is covered at the beginning of this test; however, similar plots of tests with smaller firebrand masses show different proportions of coverage. In order to compare the effect of coverage, as well as compare curves between plots, averages were taken of temperatures and heat fluxes based on the three coverage levels identified. These averages can be seen for this test for temperature and heat flux, in Figure 5.8 and Figure 5.9, respectively.

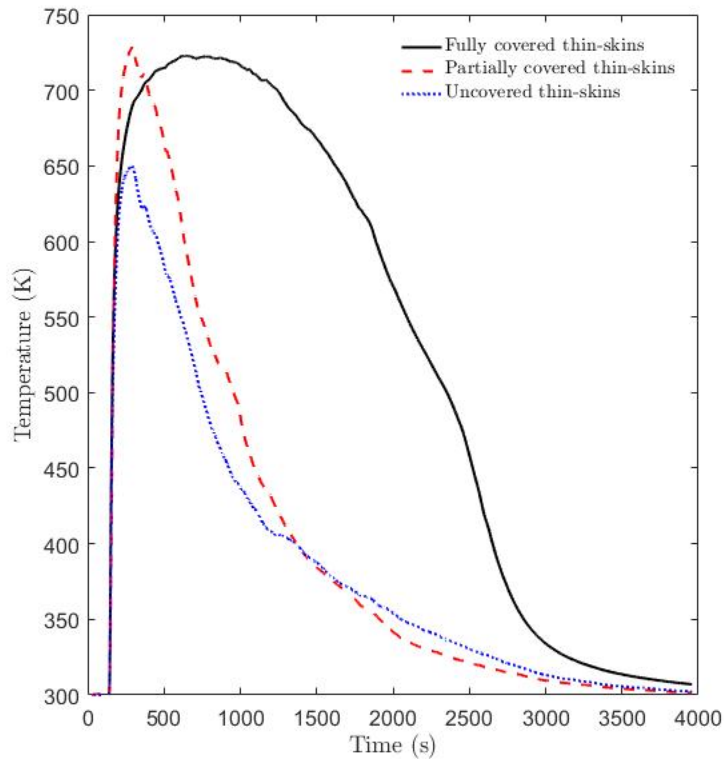


Figure 5.8: Averaged temperatures of thin-skin calorimeters based on coverage: full, partial, or no coverage (12.7 mm diameter, 9.6 g deposited mass test).

Figures 5.8 and 5.9 use the coverage from the firebrand pile of the thin-skin calorimeter array at the beginning of the test. This method produces trends with how long different heat fluxes last.

Another way to visualize these trends is by looking at the spatial distribution of heat flux. The thin-skin calorimeter array provides a way to look at how heating changes based on pile location. Figure 5.10 shows how heat flux evolves spatially throughout a single test. The areas of highest heat flux change throughout the test. The first time step shows two areas beginning to heat which are further heated in the following time step. At the third time step, though, the area of highest heat

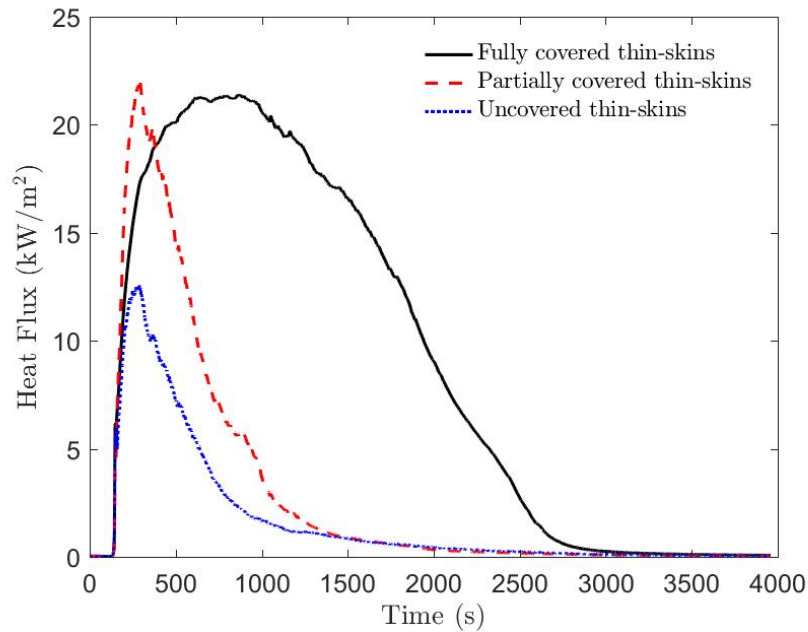


Figure 5.9: Averaged heat flux of thin-skin calorimeters based on coverage: full, partial, or no coverage (12.7 mm diameter, 9.6 g deposited mass test).

flux has shifted towards the middle of the array. The middle area continues to have the highest heat flux for the rest of the test. The dashed lines represent 14 kW/m^2 , a critical heat flux condition for radiant ignition of wood.

Figure 5.11 shows three spatial maps of heat flux for a single firebrand and for a pile of 9.6 g of firebrands. The comparison shows an instantaneous snapshot of heat flux, the average heat flux throughout the test, and the maximum heat flux for the entire test. The single firebrand heats a large area, indicating the importance of re-radiation from the firebrand. The heating in the large pile does not show the same trends. Similar to Figure 5.10, the heated area changes. For these figures, the color scale changes between figures to show the heated area trends optimally.

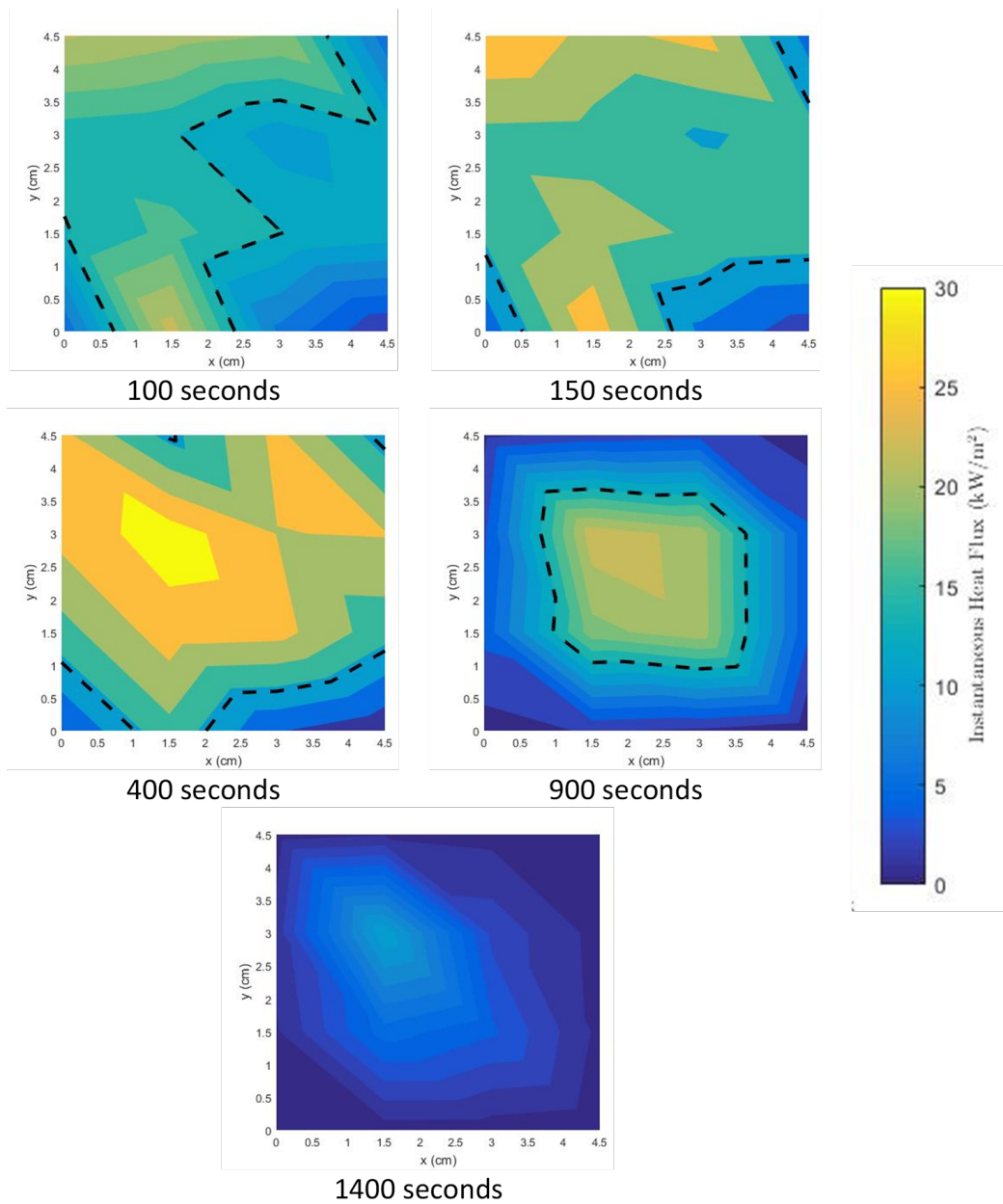


Figure 5.10: Evolution of spatial distribution of heat flux for a 5 g deposited mass pile of 12.7 mm at 100 s, 150 s, 400 s, 900 s, and 1400 s after firebrands are deposited.

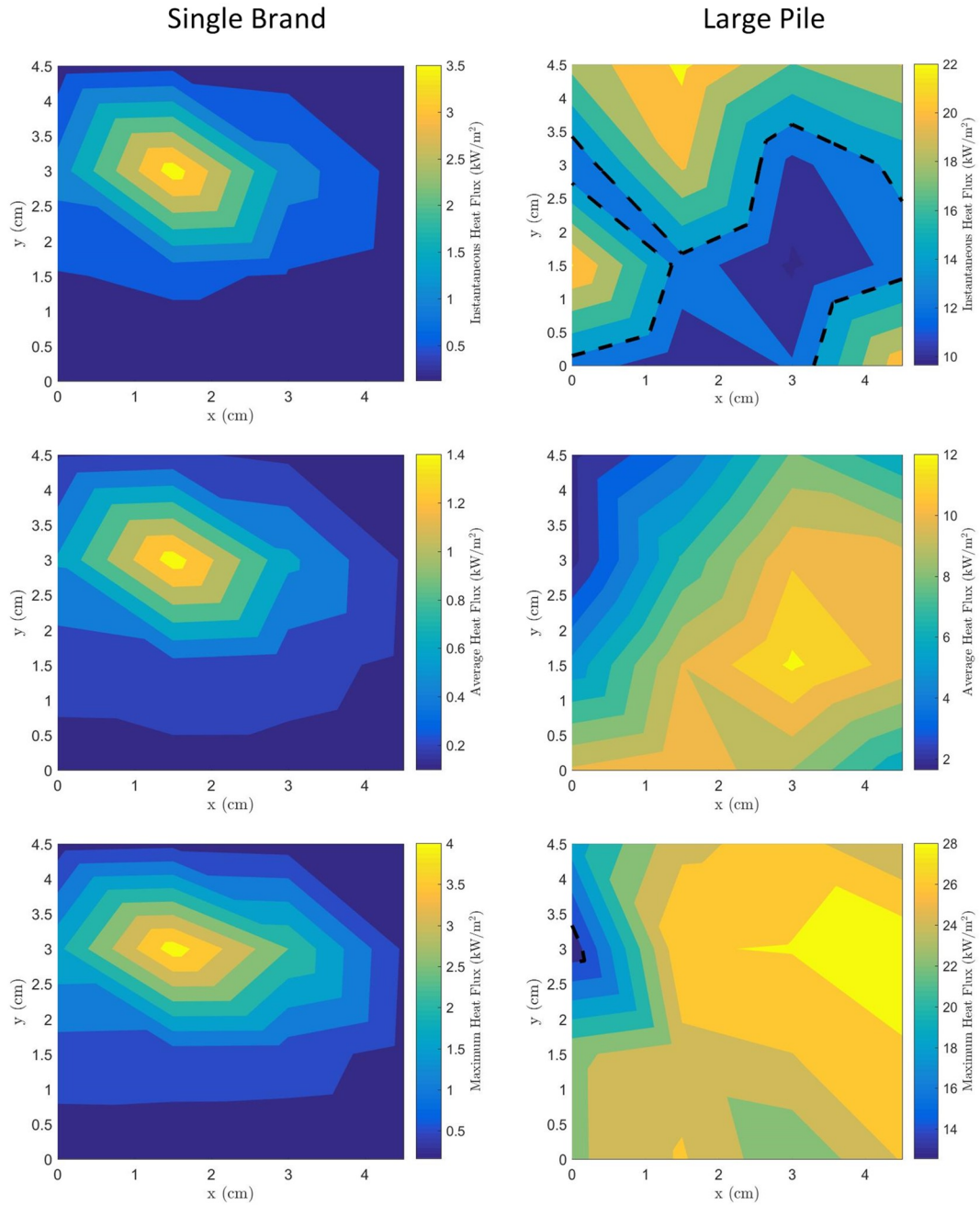


Figure 5.11: Comparison of spatial heat flux maps for (left) a single firebrand, and (right) the largest pile size, 9.6 g deposited mass. From top to bottom, heat flux maps shown an instantaneous heat flux approximately 1 min into the test, averaged heat flux over the entire test, and maximum heat flux for each location. Due to large heat flux differences, the color bar values change for each plot.

5.5 A Comparison of Heating From Piles

Two main quantities of interest were varied during firebrand pile experiments to determine what parameters affected heat flux values the most: firebrand diameter and pile size (measured as mass – initial or deposited – and as number of firebrands per pile). The following sections shows the comparison of heat flux curves as a function of firebrand diameter and deposited pile mass. Subsequent sections will compare point values for these tests as a function of diameter and pile mass.

5.5.1 Effect of Brand Diameter

Firebrand size was found to be important in previous studies using a single or a very small number of firebrands [18, 34]. Throughout these tests, firebrand diameter was varied to determine whether it was an important parameter affecting heat flux. Figures 5.12 through 5.15 show results of comparing diameters for a single pile size. These results were plotted using the average heat flux curve over all of the repetitions of a given test measured using the water-cooled heat flux gauge.

A slight variation (up to 0.2 g) between pile sizes can be noted; however, uncertainty in pile mass due to load cell readings and differences between individual tests make the masses shown comparable within the uncertainty of mass measurements. For these comparisons, the pile size used is the deposited rather than initial mass; however, the experimental matrix was produced using initial masses. Since different diameter firebrands lose different proportions of mass when burning, a similar initial mass does not necessarily translate to a similar deposited mass. Deposited

mass is used due to trends found between heating and deposited mass, which will be discussed in Section 5.5.3.

For a single firebrand (Figure 5.12), the larger diameter produced a higher heat flux over time and continued heating for longer than the smaller diameter did. This result is consistent with literature results that found that a single larger firebrand could initiate ignition in a porous fuel bed when a smaller firebrand could not [18].

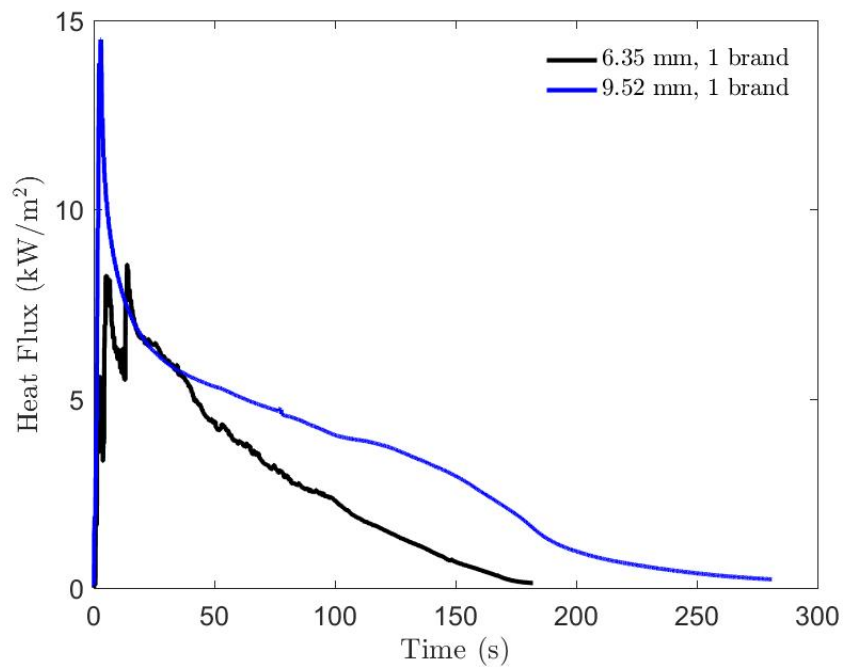


Figure 5.12: A comparison of averaged point measurements from the water-cooled heat flux gauge of 6.35 mm and 9.52 mm diameter firebrands for a single firebrand. The larger diameter produces a higher heat flux and lasts longer.

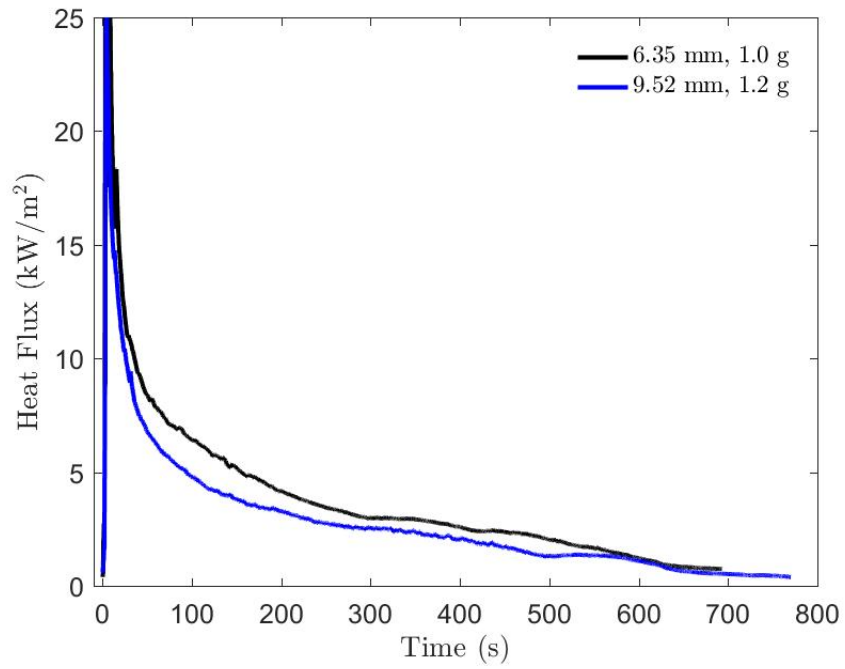


Figure 5.13: A comparison of averaged point measurements from the water-cooled heat flux gauge of 6.35 mm and 9.52 mm diameter firebrands for a 1 g pile, deposited mass. Differences in heat flux are well within the standard deviation of the average.

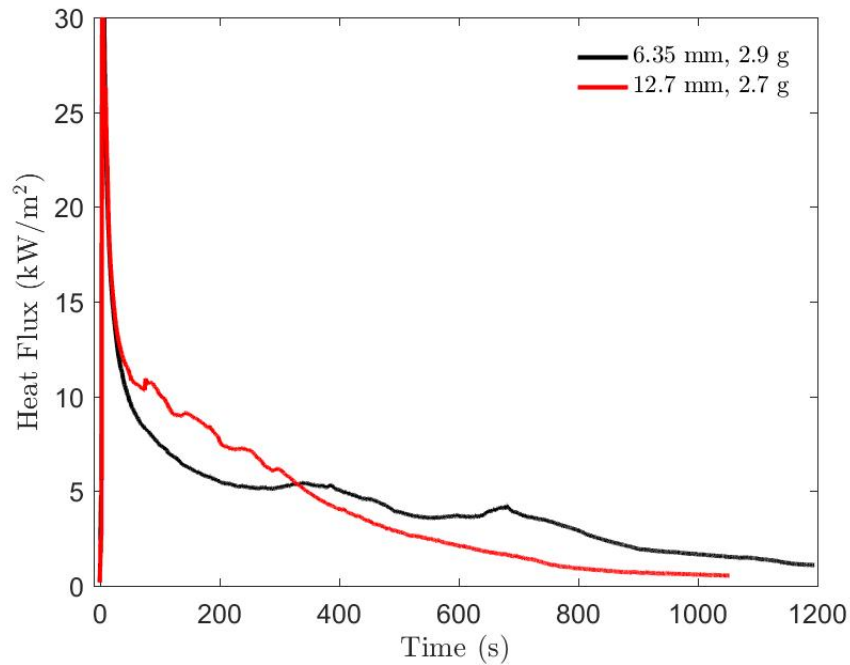


Figure 5.14: A comparison of averaged point measurements from the water-cooled heat flux gauge of 6.35 mm and 12.7 mm diameter firebrands for a 2.8 g pile, deposited mass. There is no trend apparent between heat flux and diameter.

For the largest pile compared here (Figure 5.15), the larger diameter firebrands produce higher heat fluxes; however, this trend does not hold for the medium size piles (Figures 5.13 and 5.14). For these piles, the differences are well within the standard deviation of the test. Despite a possible trend for the large piles, there is not sufficient difference to indicate that larger diameters produce higher heat fluxes. It is possible that the contact from individual firebrands becomes less important in a pile where re-radiation within the pile could provide more heating to a recipient fuel. Section 5.5.2 will show that, while diameter does not produce a strong trend, deposited mass appears to show a better trend with heating.

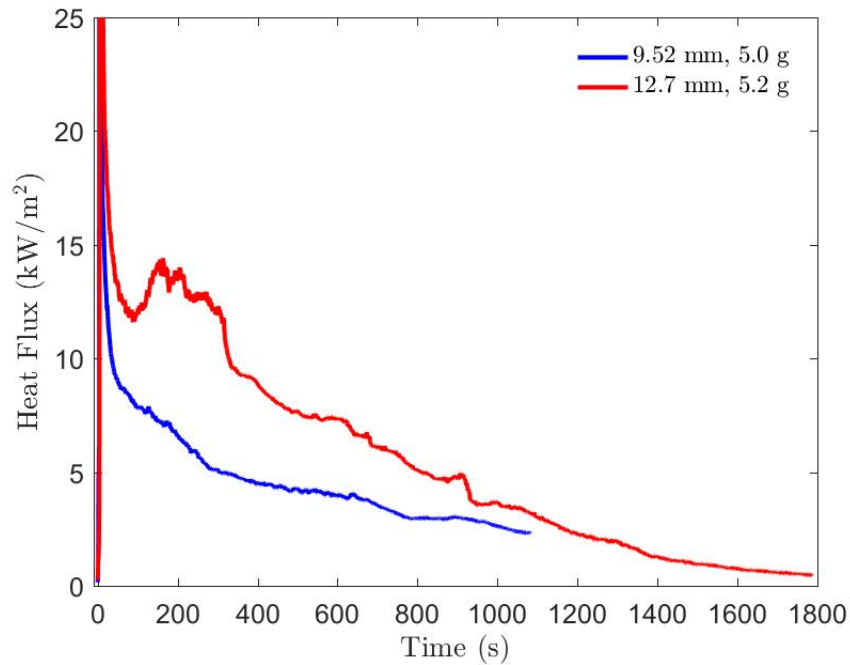


Figure 5.15: A comparison of averaged point measurements from the water-cooled heat flux gauge of 9.52 mm and 12.7 mm diameter brands for a 5 g pile, deposited mass. The drop-off of the 9.52 mm curve is due to averaging; the average heat flux curve was calculated only as long as the shortest test. The larger diameter produces higher heat fluxes.

5.5.2 Effect of Pile Mass

Larger masses of firebrands produced raised temperatures and heat fluxes for a longer period of time. This fact was observed qualitatively during testing, but shown quantitatively by comparing experiments using the same firebrand diameter, but different masses. Figures 5.16-5.19 show heat flux as a function of time for

averaged curves of the four pile masses tested, for 6.35 mm, 9.52 mm, and 12.7 mm firebrand diameters, respectively.

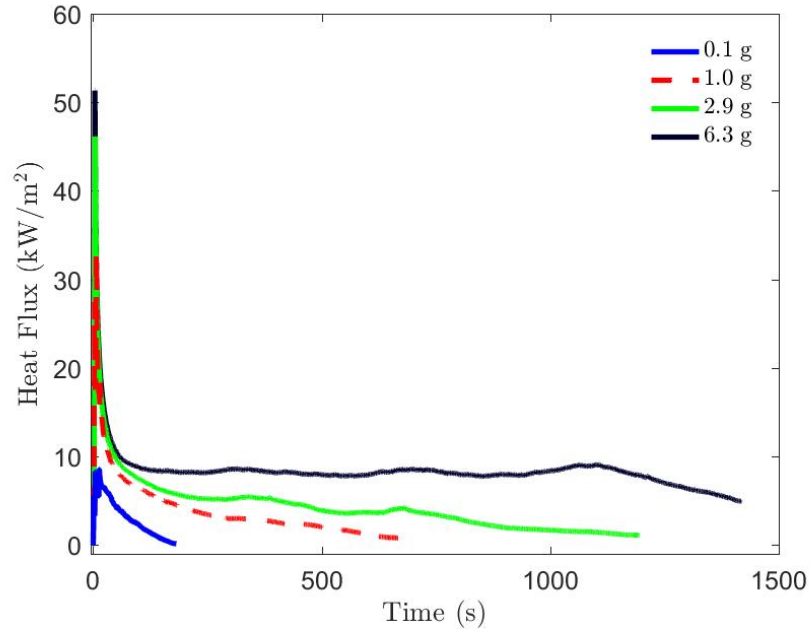


Figure 5.16: A comparison of averaged heat flux curves obtained using the water-cooled heat flux gauge as deposited pile mass increases for 6.35 mm firebrand piles.

In all cases, the the steady heat flux value after the peak increased with increasing pile size. It should also be noted that the largest pile size for each diameter had the longest semi-steady period of heat flux. Tests with higher masses also produced heating longer than tests with smaller masses. The averages do not always end at ambient conditions. This cut-off is a result of averaging over all test repetitions – some tests lasted longer than others, even at the same diameter.

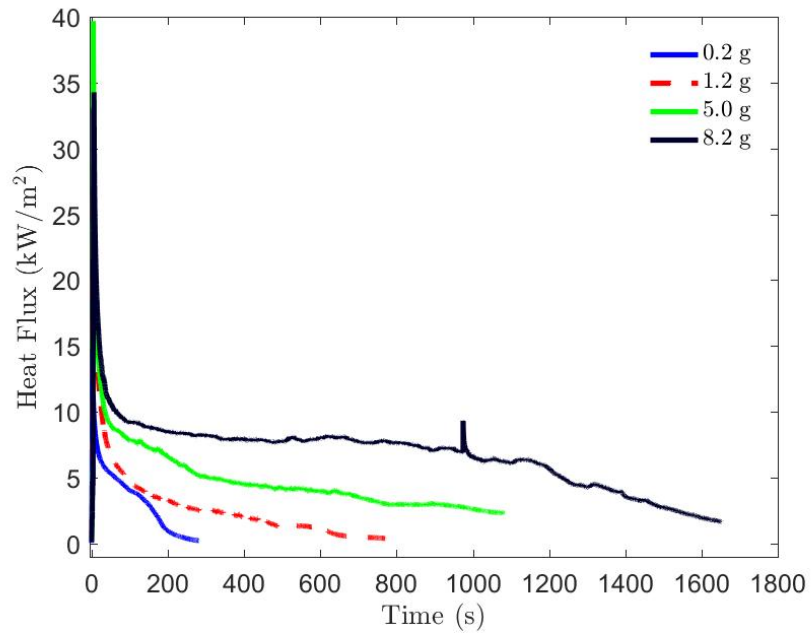


Figure 5.17: A comparison of averaged heat flux curves obtained using the water-cooled heat flux gauge as deposited pile mass increases for 9.52 mm firebrand piles.

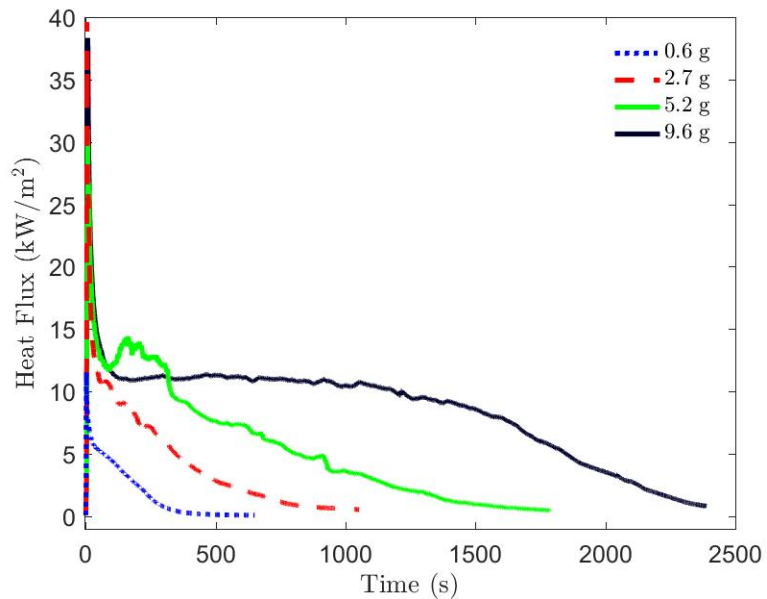


Figure 5.18: A comparison of averaged heat flux curves obtained using the water-cooled heat flux gauge as deposited pile mass increases for 12.7 mm firebrand piles.

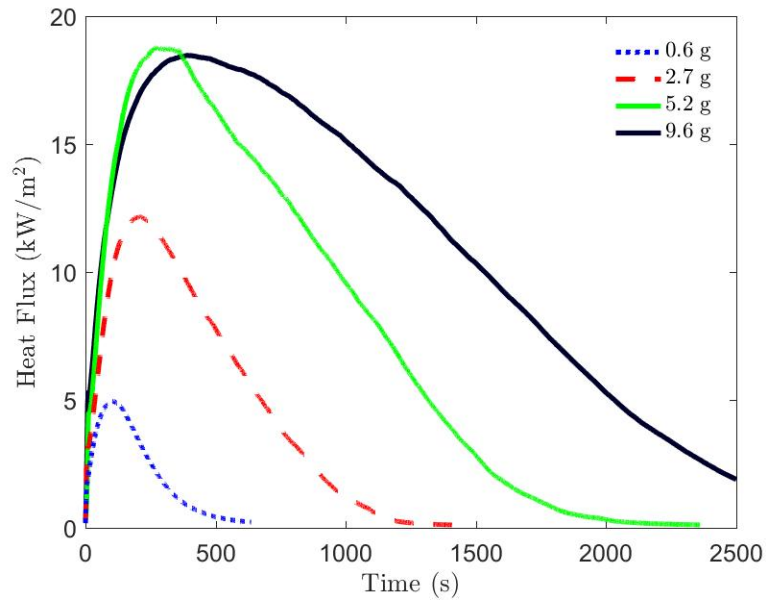


Figure 5.19: A comparison of averaged heat flux curves obtained using the thin-skin calorimeters as deposited pile mass increases for 12.7 mm firebrand piles.

5.5.3 Peak Heat Flux and Net Heating

Initial results provided heat fluxes as a function of time; however, it would be helpful to have a parameter which could be used to quantify and compare the overall heating between different tests. Such a parameter would be particularly helpful in smoothing out the different shapes of the heat flux curves for the water-cooled heat flux gauge and the thin-skin calorimeter array. Initially, the peak heat flux was used as a comparison between tests. The peak heat flux was plotted against firebrand diameter and deposited mass. Figures 5.20–5.23 show these results for both thin-skin calorimeters and the water-cooled heat flux gauge.

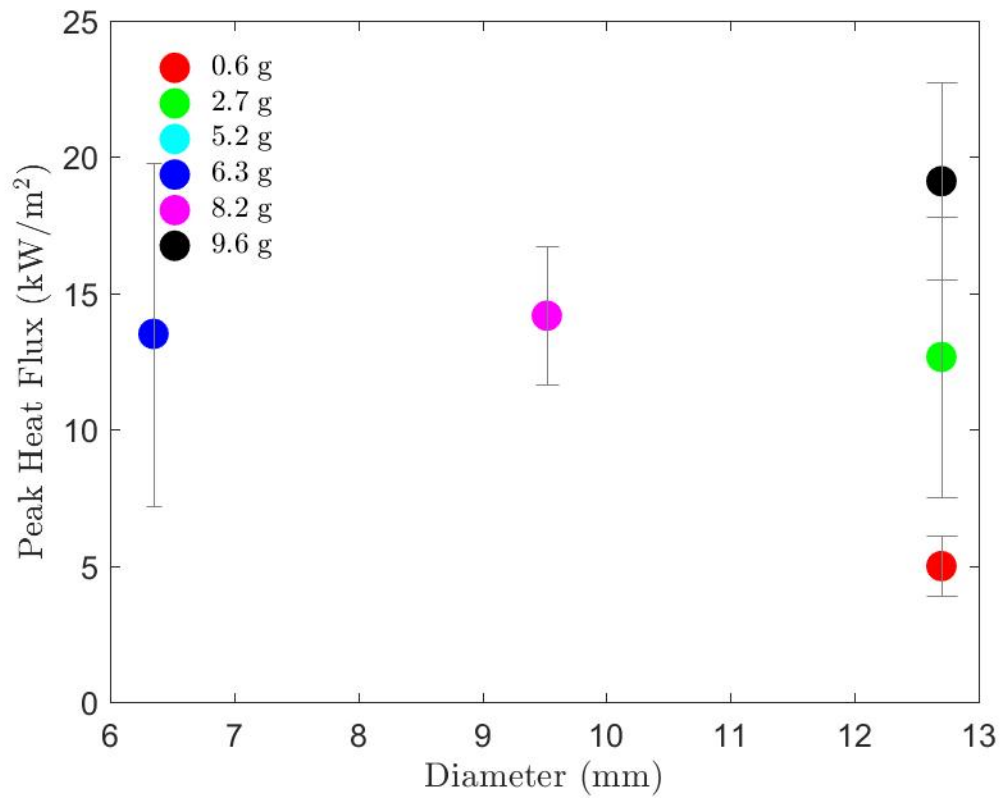


Figure 5.20: Peak heat flux as a function of firebrand diameter from thin-skin calorimeter tests.

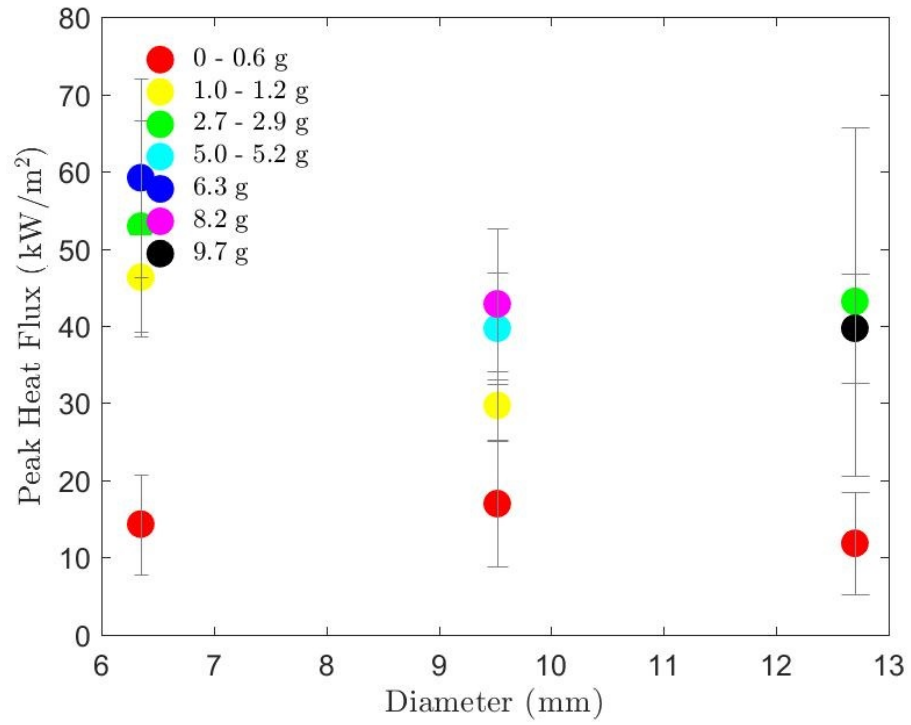


Figure 5.21: Peak heat flux as a function of firebrand diameter from water-cooled heat flux gauge tests.

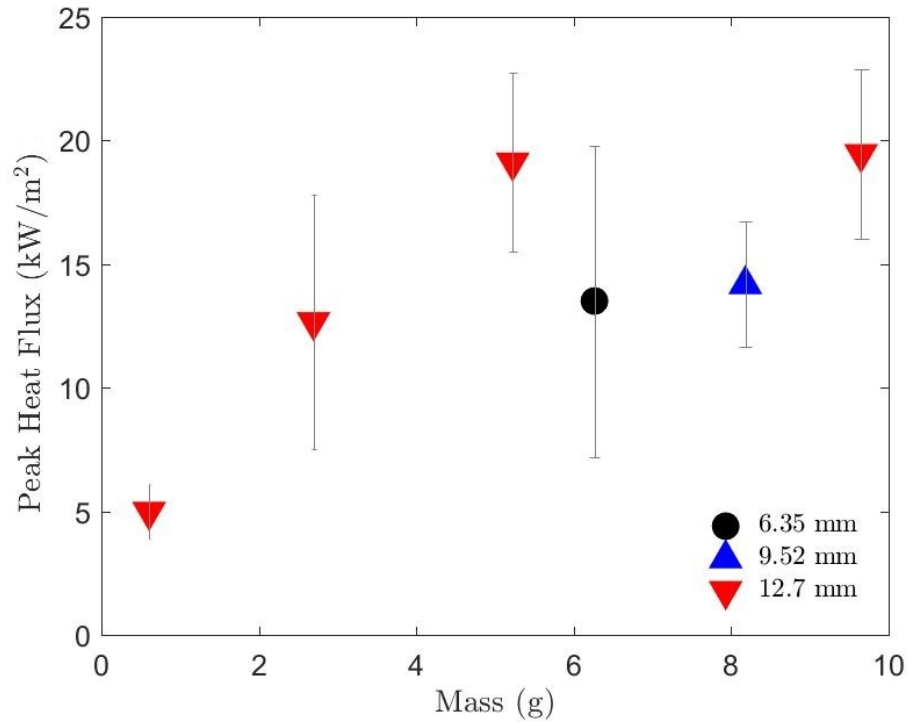


Figure 5.22: Peak heat flux as a function of deposited mass from thin-skin calorimeter tests.

Plotting the peak heat flux as a function of either firebrand diameter or mass deposited does not produce informative results. The peak heat flux increases when a pile, rather than a single firebrand, is deposited; however, the values of peak heat flux for piles do not vary significantly, and the variation is typically within the standard deviation for a given diameter. This trend is particularly clear in Figure 5.23.

As the peak heat flux does not produce the most telling results, a net heating parameter was introduced to compare tests. The net heating parameter was calculated as the area under the heat flux versus time curve and represents the total heat

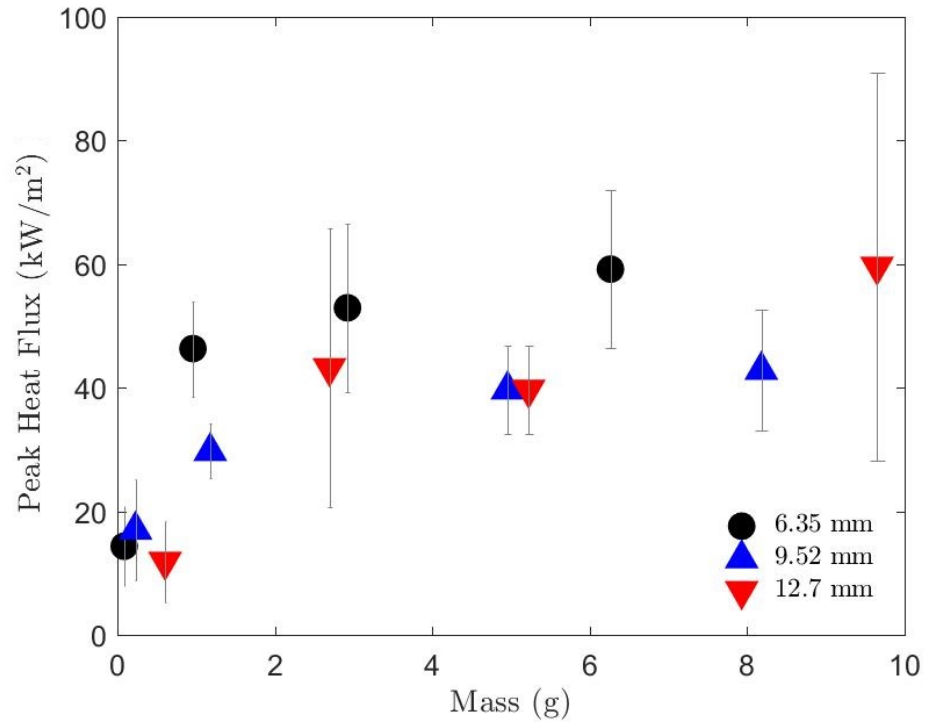


Figure 5.23: Peak heat flux as a function of deposited mass from water-cooled heat flux gauge tests.

imparted from the firebrand pile to the heat flux gauge throughout the test. The results of plotting the net heating parameter as a function of diameter and deposited pile mass are shown in Figures 5.24-5.26. Figure 5.26 shows that plotting the net heating parameter as a function of pile mass results in a linear relationship, where the total heat imparted by the firebrand pile increases as the pile size increases. This result is expected as a larger mass of firebrands has a larger potential chemical energy to release over time.

There is a question about an appropriate way to measure firebrand pile size. Results using mass deposited have been used in the figures so far shown; however, measuring the number of firebrands in a pile has been suggested as a potential

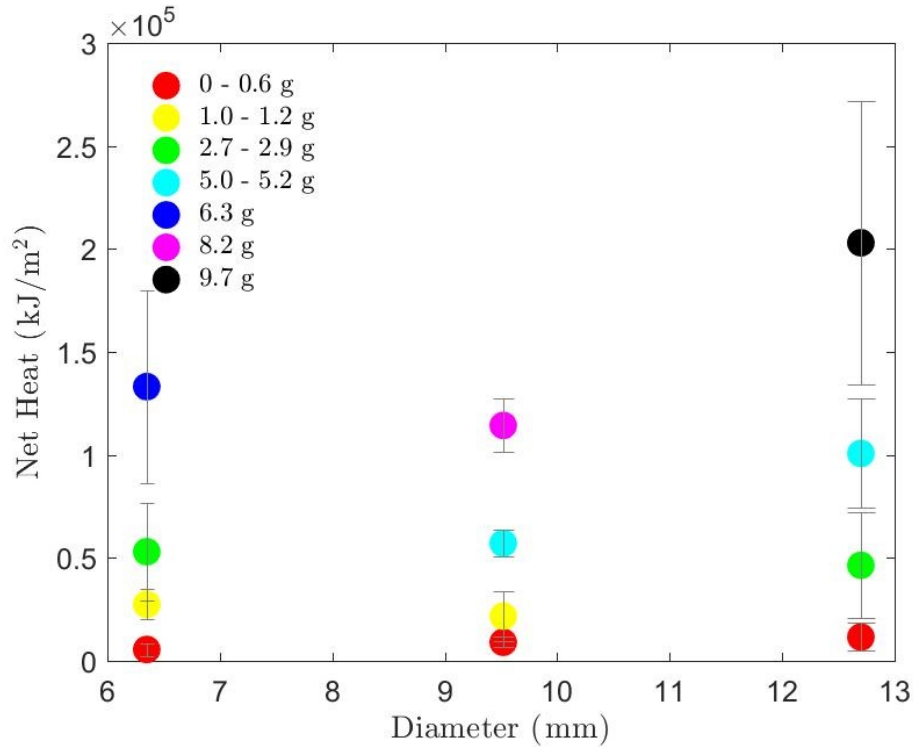


Figure 5.24: Net heating parameter as a function of firebrand diameter for water-cooled heat flux gauge tests.

option. The net heating parameter from the water-cooled heat flux gauge tests was plotted against the total number of firebrands in a pile in order to compare these two methods of measuring pile size. Figure 5.27 shows net heating as a function of number of firebrands in a pile.

Despite the fact that Figure 5.27 shows an approximately linear relationship between number of firebrands and net heat released for each diameter, the trend clearly varies with diameter. Figure 5.26 shows that the different trends of the diameters collapses towards a single linear trend when plotted as a function of deposited mass. These results indicate that mass may be a better metric than firebrand number to describe pile sizes. As the number of firebrands for a given

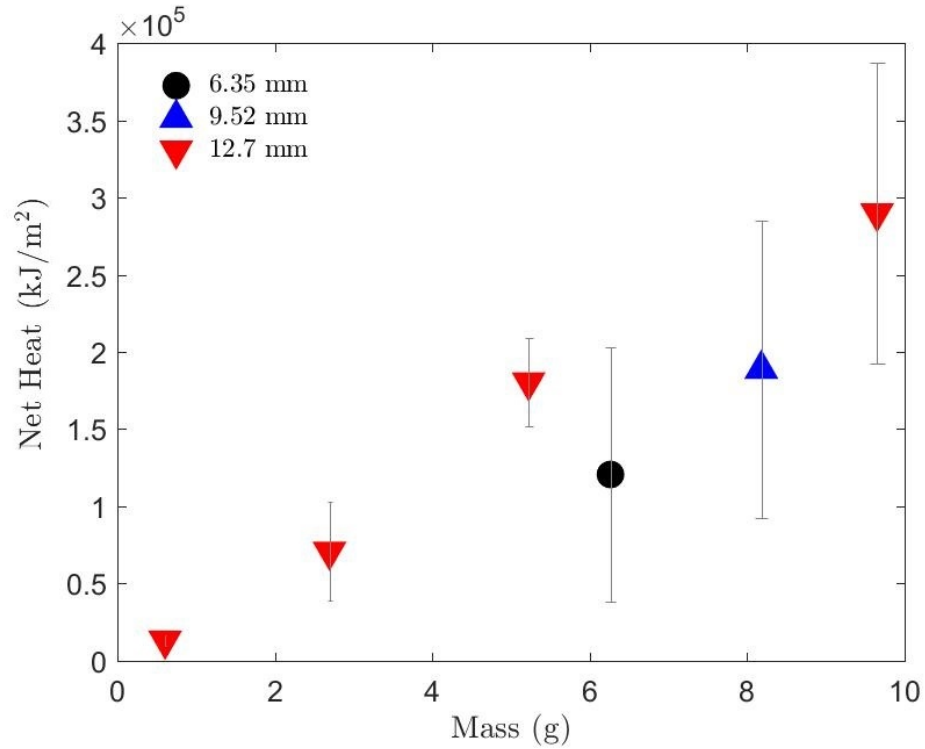


Figure 5.25: Net heating parameter as a function of deposited pile mass for thin-skin calorimeter tests.

mass pile varies significantly with brand diameter, it is unsurprising that pile mass provides a better metric. For example, 37 wooden dowel pieces of 12.7 mm diameter were required to produce 70 g of wood, whereas 142 pieces of 6.35 mm diameter were required to produce the same initial mass.

Although the net heating parameter provides some potentially useful information, it is calculated over an entire test. Taking the heating over an entire tests does not take into account the fact that a critical condition (e.g. heat flux) is needed to ignite a material. Previous experiments of both flaming and smoldering ignition [10, 22, 23] have found that it is necessary to maintain a critical heat flux (or temperature) for a given time in order to ignite a material. The time to ignition

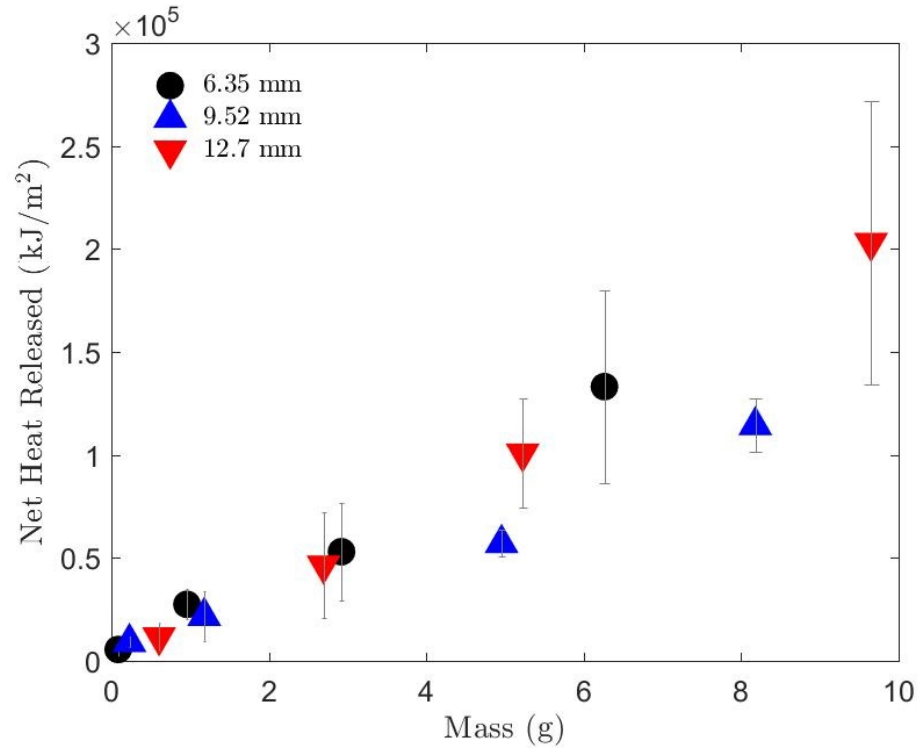


Figure 5.26: Net heating parameter as a function of deposited pile mass for water-cooled heat flux gauge tests.

is dependent on the heat flux and time to ignition decreases as heat flux increases; however, below a critical heat flux, ignition will not occur.

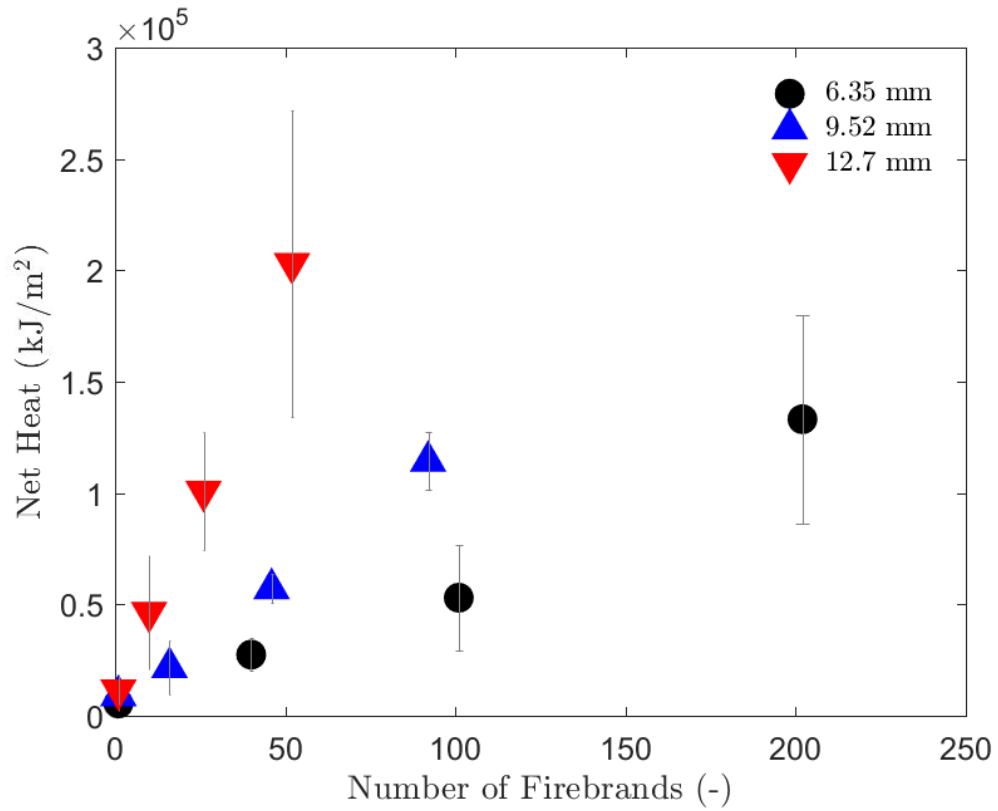


Figure 5.27: Net heating parameter as a function of number of firebrands in the pile. Each marker is an average of all repetitions conducted for a specific test condition. Error bars are the standard deviation of the repetitions.

Chapter 6: Results of Ignition Tests

6.1 Overview

The following chapter describes the results of a series of ignition tests. Two sets of tests were completed: tests using OSB as a recipient fuel using two firebrand pile sizes and a set wind velocity. All initial tests using OSB found smoldering, so flaming ignition was sought. A second set of tests replicated the pile size and wind velocity, but were conducted on an inert surface so that heat flux and temperature measurements beneath the pile could be made. Pile sizes were approximately 5 g and 10 g deposited mass of 12.7 mm firebrands. The wind velocity was 1.84 m/s.

6.2 Visual Observations

When firebrand piles were initially deposited onto the recipient fuel, immediate flaming occurred briefly, but was not sustained. This flaming occurred when the firebrands were exposed to the external flow, and thus flames were sometimes present upon deposition. This occurred for tests both with and without the recipient fuel. Figure 6.1 shows this phenomenon – a small flame is visible on the top right hand side of the image.



Figure 6.1: Side view of a flat ignition experiment immediately after firebrand pile is deposited. A small flame occurs in the upper right hand portion of the image. Wind direction right to left.

Although this initial flaming occurs, the flames last very briefly. Thus it is not supposed that the flames from the firebrands directly cause ignition of dense thermally thick fuels. Additionally, the immediate deposition of the entire firebrand pile is unlikely to be found in a WUI fire. It is more likely that single firebrands would gradually deposit on a pile over time.

Within one minute of the beginning of the test, flaming is visible on the sides of the firebrand pile. Approximately a minute and a half into the test, a flame anchored to the recipient fuel is visible, as shown in Figure 6.2. A visual sign of potential smoldering is a spreading char front in areas not directly in contact with firebrands. This charring could, possibly, also be the effect of high radiant heat fluxes from the pile; however, in this case, blue flames are visible on the bottom left hand corner of the pile and on the top left hand corner in the image. A bright

yellow flame is also visible anchored to the OSB directly to the right of the glowing core of the firebrand pile.



Figure 6.2: Side view of flat ignition experiment over OSB 1 min into experiment. Flames anchored to the fuel surface are visible. The wind direction is from right to left.

As the experiment progresses, flaming continues from several locations on the surface of the fuel on the side of the firebrand pile. Flaming of the glowing core of the firebrand pile also occurs intermittently. Flaming of the fuel is sustained for approximately 10 min. Figure 6.3 shows the same test as the previous figures at the 10 min mark.

After about 15 min, the test ceases flaming and the firebrand pile is blown over the test section (see Figure 6.4). This likely occurs as the firebrand pile has mostly turned to ash, becoming light enough to be lofted by the wind. The fuel continues to smolder for nearly an hour with intermittent reheating. This test lasted approximately an hour. Other flat tests followed the same approximate trends.



Figure 6.3: Side view of a flat ignition experiment over OSB 10 min into the experiment. Flaming combustion is sustained for the recipient fuel. The wind direction is from right to left.

6.2.1 Description of the Ignition Process

Initially, three possible processes for ignition were hypothesized. Figure 6.5 shows a conceptualization of possible processes. The first possible process identified is that glowing or smoldering firebrands could transition to flaming and the flaming firebrands could ignite the recipient fuel. The second possible process is that the smoldering firebrands could heat the recipient fuel directly and cause the recipient fuel to begin smoldering. In this case, it is supposed that the recipient fuel would itself transition to flaming, possibly in front of the firebrands where there is more oxygen available. The third possible process would be a long-term heating of the recipient fuel, which would later transition to flaming ignition somewhere over the surface of the fuel.



Figure 6.4: Side view of flat ignition experiment over OSB 15 min into the experiment. Flaming combustion has ceased. The wind direction is from right to left.

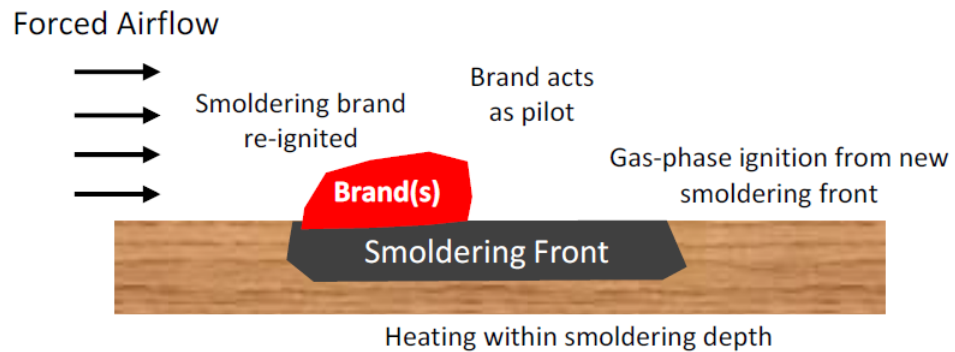


Figure 6.5: Conceptualization of possible ignition processes that occur when firebrands ignite a recipient fuel.

Based on visual and IR observations of the tests, it appears that some form of the second process described is most likely. The first process does not seem to fit the behavior, as sustained flaming of firebrands did not occur for tests without a recipient fuel, including those tests conducted under the exact same wind and pile size configurations. On the other hand, the recipient fuel ignited fairly early in the test, indicating that long-term heating before ignition may not accurately represent the ignition process in this experimental scenario.

Figure 6.2 shows flaming ignition of the recipient fuel in two locations. On the close edge of the OSB, blue flames are visible over a charred section of fuel. Towards the center of the firebrand pile, a charred section of wood is visible in front of the brightly glowing firebrands, and a flamelet appears to be anchored in this location. Based on this description, it appears recipient fuel has been heated directly. Flaming of firebrands for brief periods may have acted as a pilot ignition source for the potentially smoldering fuel.

6.3 Thermal Characteristics at Ignition

For each ignition test, IR video was recorded in order to provide a qualitative picture of the changing surface temperature. The video was used mostly for qualitative purposes because of the unknown emissivity of the firebrands. IR video was also recorded during tests with a nearly adiabatic surface used to measure heat fluxes leading up to ignition. Other thermal characteristics obtained for ignition experiments included the temperature beneath the firebrand pile, measured using a thermocouple, and the thin-skin calorimeter array measuring the heat flux beneath the pile.

6.3.1 Temperatures

Frames from the IR video were obtained for the key times described in the visual observations section previously. They are shown in Figure 6.6 next to the

corresponding visual image. The top row shows some heating surrounding the firebrand pile, but the highest temperature is in the firebrand pile.

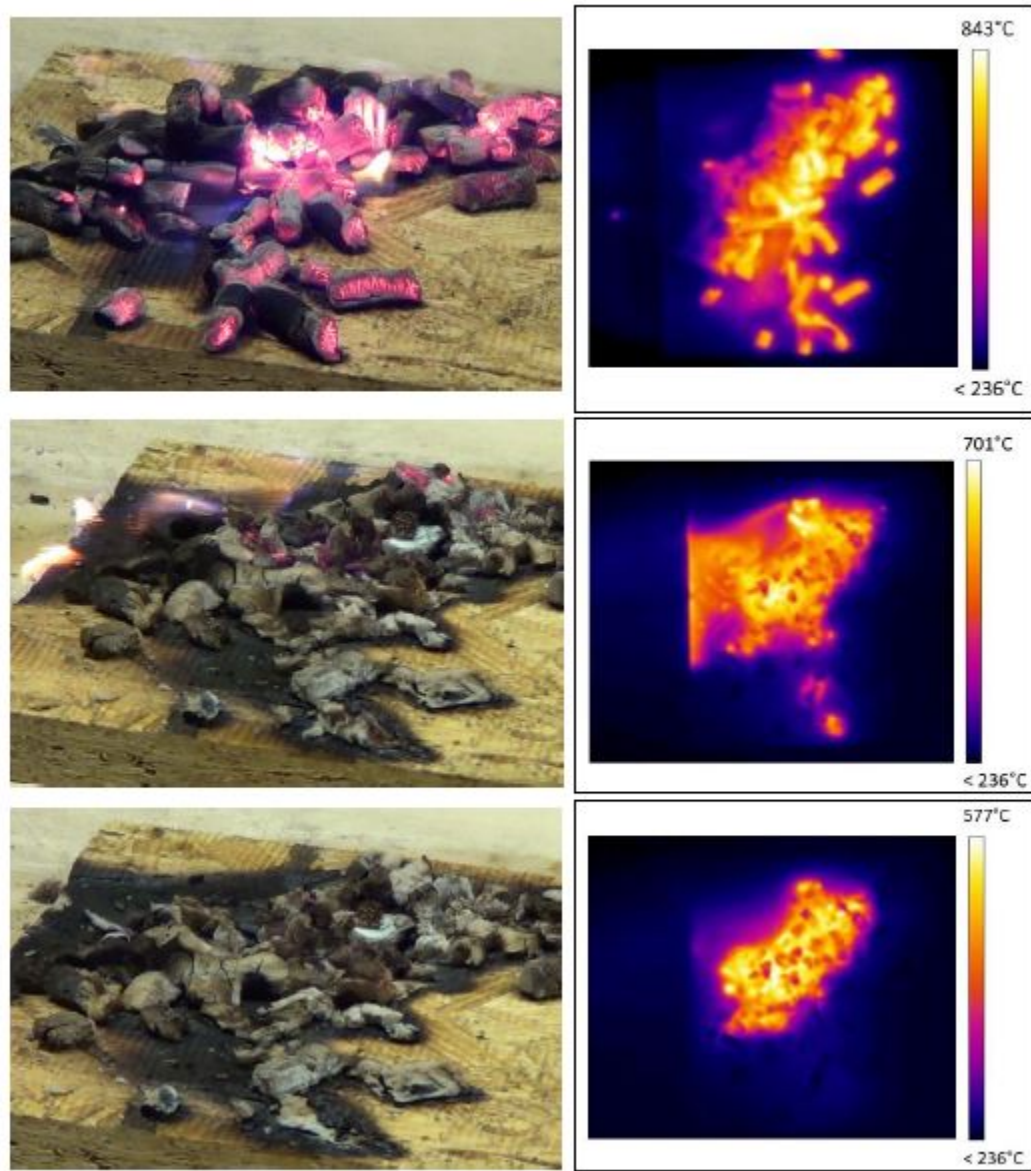


Figure 6.6: Visual image (left) and IR image (right) captures for, from top to bottom: 1 min, 10 min, and 15 min into an ignition test. Note the changed scales on the IR images. The wind is from the right side of images.

The middle image shows the ignited fuel at the back of the firebrand pile. The bottom image shows the high temperatures of remaining firebrands, despite an ashy pile with no visible combustion.

Thermocouple and thin-skin calorimeter temperatures were also measured during these tests and are plotted in Figures 6.7 and 6.8. Figure 6.7 shows the overall averaged temperature for covered thin-skin calorimeters, and Figure 6.8 shows the four thin-skin calorimeters immediately nearest the thermocouple.

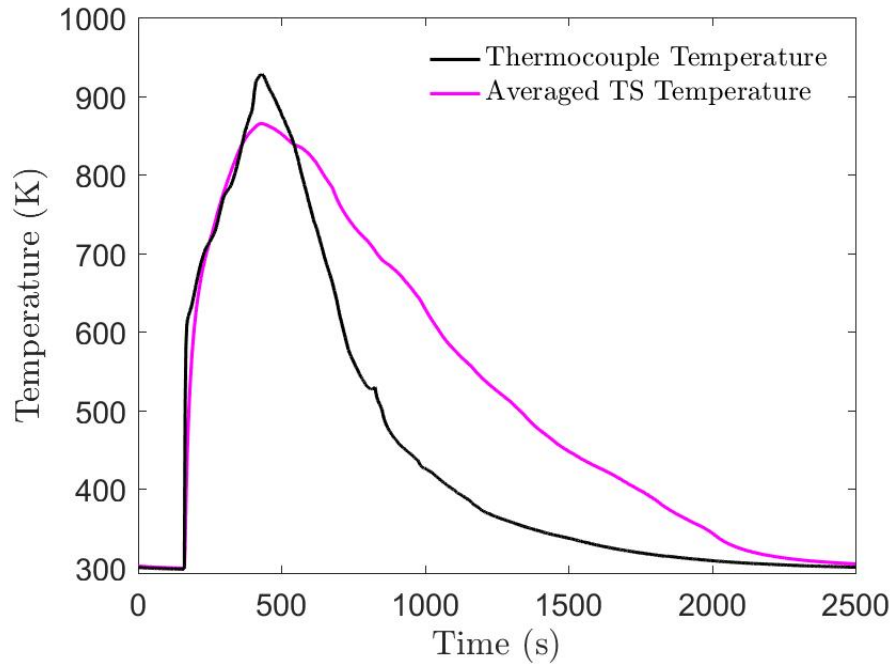


Figure 6.7: A comparison of the thermocouple temperatures and thin-skin temperatures averaged over all covered thin-skins for one test of 10 g deposited mass.

Both the thin-skin calorimeters and the thermocouple reach higher temperatures than the IR camera, which is perhaps reasonable given the uncertainty of the emissivity. It is also possible heat losses from the surface and the insulating

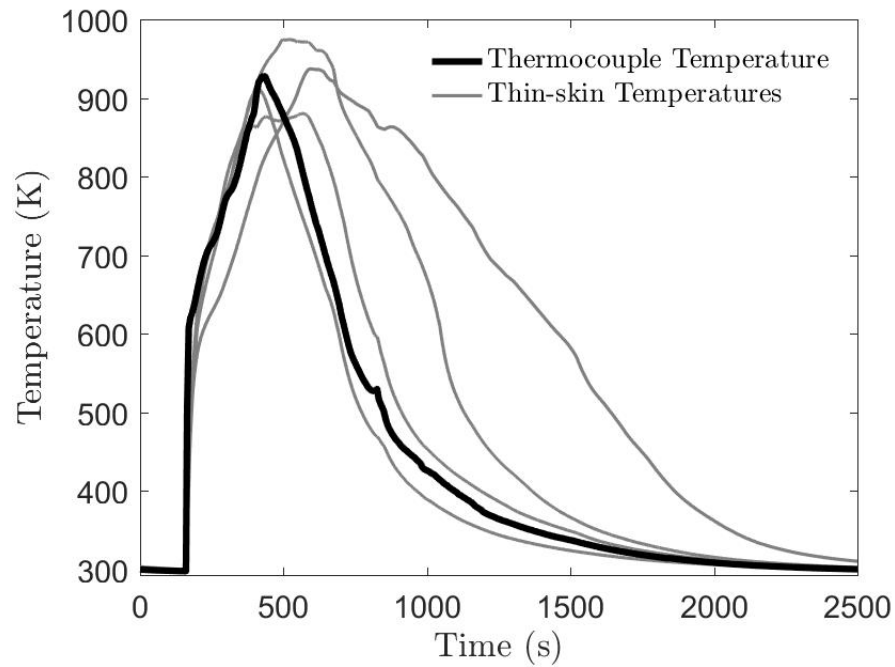


Figure 6.8: A comparison of the thermocouple temperature with the temperatures measured by the four thin-skin calorimeters surrounding the thermocouple for the same test as previous figure.

effect of a pile of brands increases temperatures below the pile. The temperatures of the thin-skin calorimeters remain higher longer than both the thermocouple and IR camera, which is expected due to heat storage. The total time of raised temperatures underneath the pile is approximately 40 min.

6.3.2 Heat Flux

Heat flux was measured under piles of 5 g and 10 g deposited mass under the 1.84 m/s external airflow. Figure 6.9 shows the heat flux measured from all

sixteen thin-skin calorimeters for a single 10 g test. Heat flux results presented in this section are for the same test presented in the previous section on temperature.

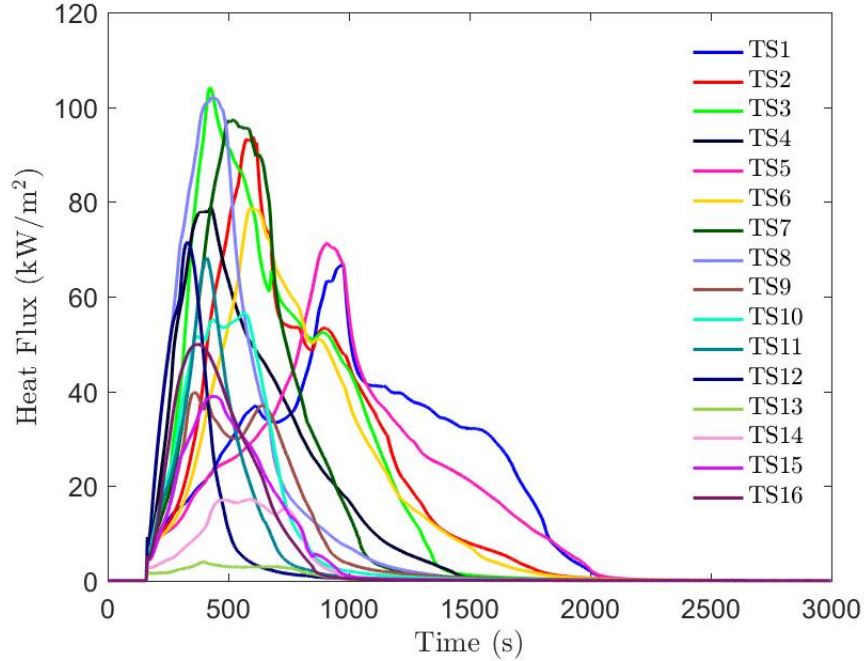


Figure 6.9: Heat flux as a function of time for the full thin-skin calorimeter array for a 10 g deposited mass test with applied wind.

One aspect that heat flux measurements highlight is the spatial difference in heat fluxes. In Figure 6.9, most of the thin-skin calorimeters peak around 500 s; however, two thin-skin calorimeters (TSC 1 and TSC 5) peak more than 500 s later. This difference in timing of the heat flux peaks may be a result of areas of the firebrand pile reheating and the wind blowing the pile as more of it turns to ash.

Figure 6.10 shows the average heat flux as a function of time averaged for six tests at 10 g deposited mass. There is high variation in the measured heat flux using the thin-skin calorimeters.

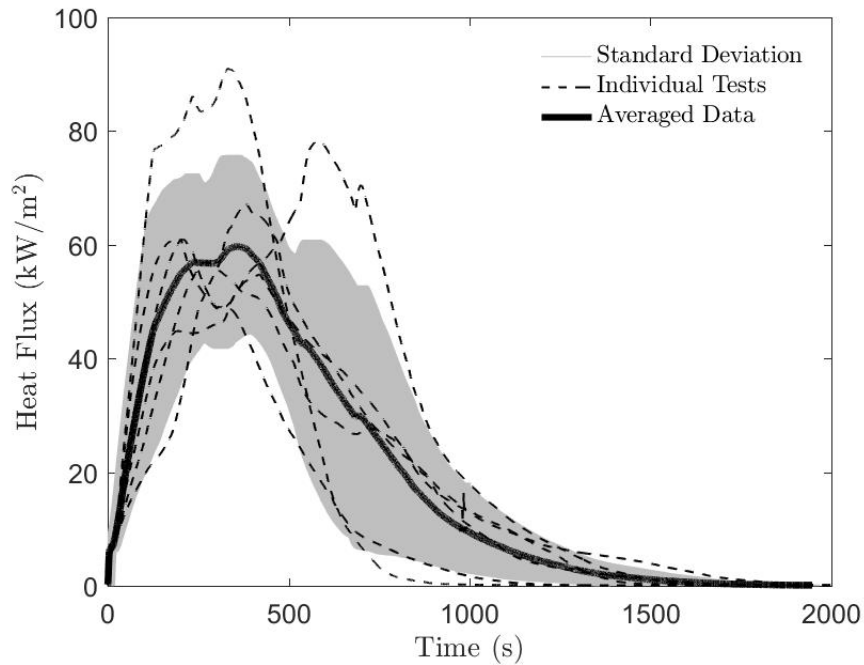


Figure 6.10: Averaged heat flux curves for 10 g deposited mass tests with wind.

6.3.3 Spatial Distribution of Heat Flux

One phenomenon noticed in these tests was a reheating in different parts of the firebrand pile. This trend was obvious in the IR video temperatures and the time-dependent heat flux curves. The following series of spatial distributions of the heat flux for a single test show how heat flux develops in different parts of the firebrand pile.

Figure 6.11 shows the spatial distribution of heat flux approximately a minute into one test, when ignition is expected. Figure 6.12 shows the same test over ten minutes into the test. In this case, there is no recipient fuel. Nonetheless, the location of heating has changed, as has the total heat. A different hot spot has developed here. Note that the scales are with respect to the maximum and

minimum heat flux measured at a given time. The dashed line represents 14 kW/m^2 , a minimum threshold for radiant ignition of wood.

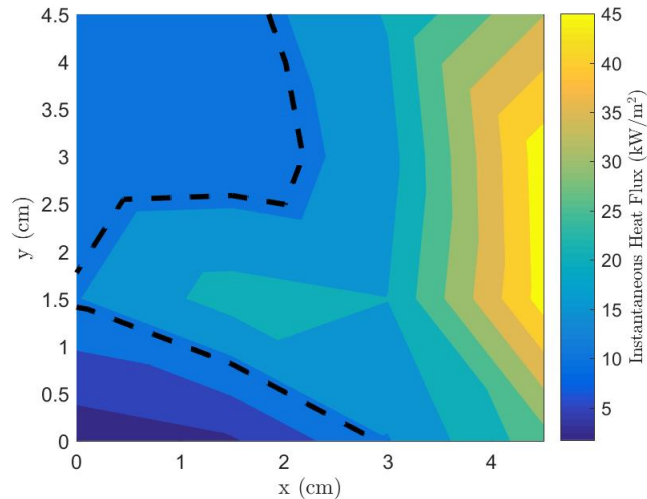


Figure 6.11: Spatial distribution of heat flux approximately 1 min into a test with 10 g deposited pile mass. Wind direction right to left.

Figures 6.13 and 6.14 show the average and maximum heat fluxes obtained throughout the entire test. The average is taken over the first two thirds of the test to more accurately represent averages during higher active heating. It is interesting to note that the locations of the highest heat fluxes do not necessarily correlate with the locations of overall highest average heat flux.

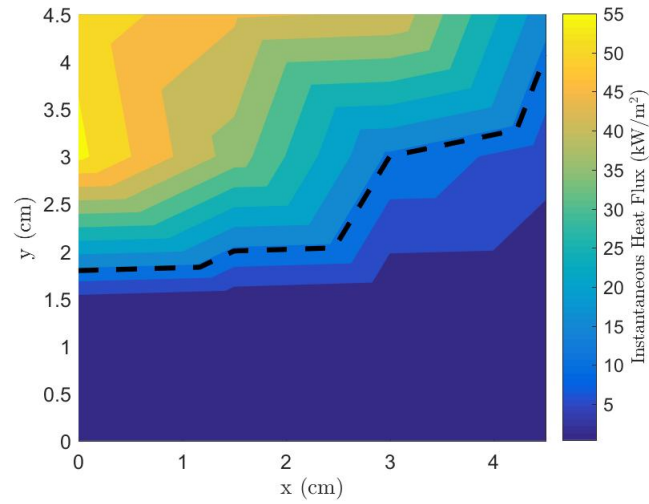


Figure 6.12: Spatial distribution of heat flux over 10 min into the same test with 10 g deposited pile mass. Wind direction right to left.

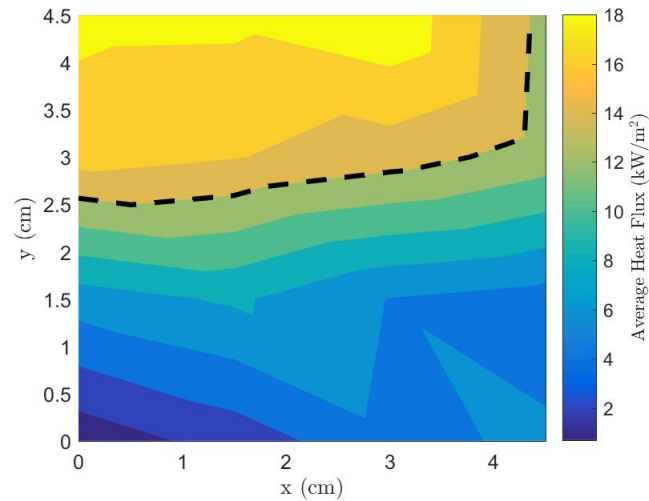


Figure 6.13: Spatial distribution of heat flux averaged over the first two thirds of the forced flow test with a 10 g firebrand mass.

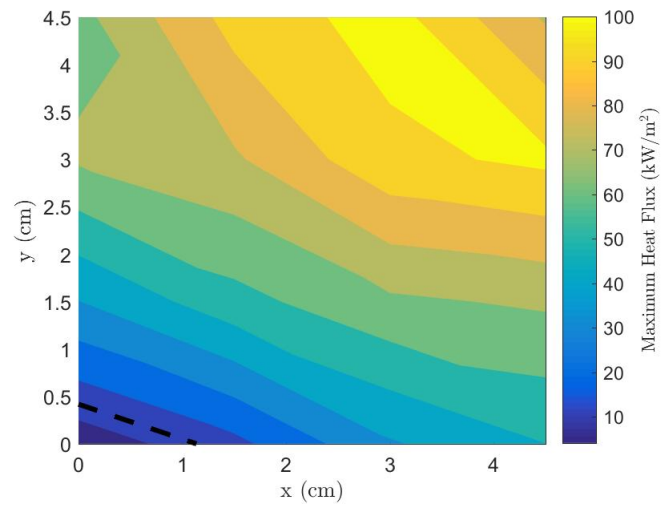


Figure 6.14: Spatial distribution of the maximum heat flux obtained for each point during the forced flow 10 g mass test.

Chapter 7: Discussion

7.1 Firebrand Pile Heat Flux Tests

An initial comparison of heat flux curves found using the thin-skin calorimeters and the water-cooled heat flux gauge shows some clear trends. The shape of the latter heat flux curves includes a sharp spike, which drops off quickly and then steadies, sometimes only briefly, at a much lower value. On the other hand, heat fluxes from the thin-skin calorimeters did not register a similar peak, but peaked later and recorded higher heat flux values for a longer time.

There are definite limitations to both types of heat flux measurement methods used for these tests. The water-cooled gauge may be cooling firebrands, while the calibration of the thin-skin calorimeters has such high uncertainties that the values cannot be taken as accurate quantitative measures. Ultimately, an improved method is needed to measure heat flux if quantitative values, not just trends, are desired; however, trends provide important information on the parameters which influence heating. One possible method would be a high temperature thermopile. A thermopile was not used in this study due to concerns about durability at high temperatures; however, the temperatures measured in these tests (up to 900°C) are below the maximum temperature for one thermopile which was considered (up to

1000°C). There would still be potential issues with a thermopile, but this option may be worth exploring.

The firebrand pile results also found that heat flux was not highly dependent on firebrand diameter for large piles. Previous studies have found that small piles and single firebrands are dependent on size; however, the ignition tests here show the importance of large piles. It would be better to get a wider array of data for a single firebrand diameter or size first. Varying pile mass is a more important parameter and affects heat flux and net heating from tests. This knowledge is critical when determining which parameters are most important to measure in order to estimate a firebrand “flux” which is representative of exposure in WUI fire conditions. The mass of smoldering firebrands deposited in a location, thus far, appears to be the most important parameter.

7.2 Ignition Tests

Ignition tests in the wind tunnel indicated a potential process governing ignition of a recipient fuel from a firebrand pile. This process of ignition highlights the impact of a large mass of heated objects, rather than a single heated object. The re-radiation within the pile also plays a key role, as does reheating. Reheating may be an important parameter to consider in future ignition models, as it resulted in re-initiation of flaming during some tests.

The applied airflow is clearly important as it produced ignition and higher heat fluxes. Although these heat flux values may not be entirely accurate, comparing the

heat fluxes found for ambient and forced flow tests shows a drastic difference (see Figure 7.1). Heat fluxes are seen to peak much higher under forced flow conditions. This is expected to occur as increased airflow induces more oxidation which results in higher heat release and higher temperatures of the brands, ultimately resulting in higher surface temperatures at the test section and higher estimated heat fluxes by thin-skin calorimeters. This heating, however decays much faster than under ambient conditions for similarly-sized tests.

A similar trend can be seen with the net heating parameter when ambient and forced flow tests are compared, particularly for the larger mass pile (Figure 7.2). The difference appears to be that, in the wind-driven tests, the heat is transported over a much smaller time, resulting in higher heat fluxes than with the ambient tests. During ambient tests relatively the same amount of heat is transferred, except that it is transferred over a longer time, resulting in lower heat fluxes.

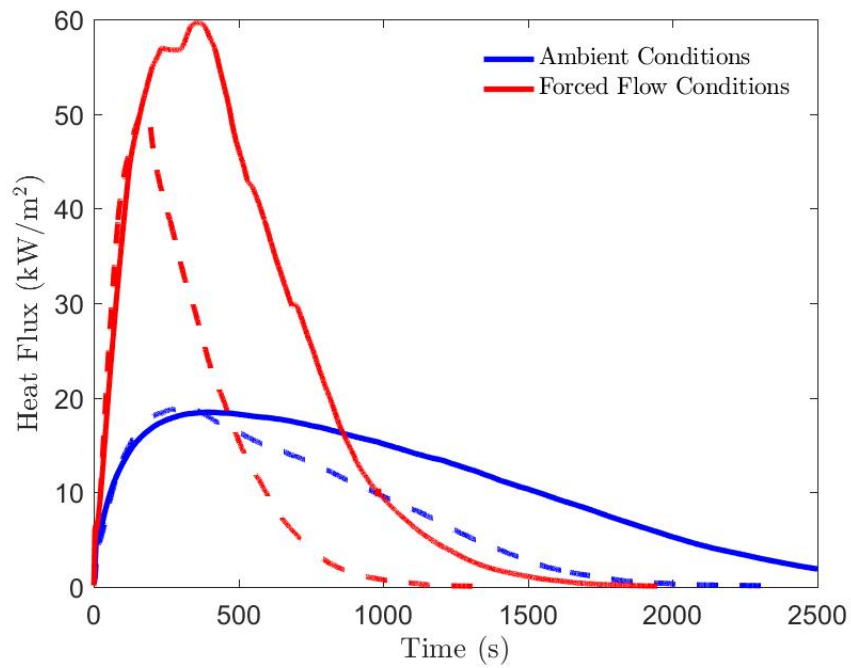


Figure 7.1: A comparison of averaged heat flux curves, measured with thin-skin calorimeters, under ambient and forced flow conditions. The dashed lines represent initial mass 50 g test while the solid lines represent initial mass 100 g tests. All tests use 12.7 mm diameter firebrands.

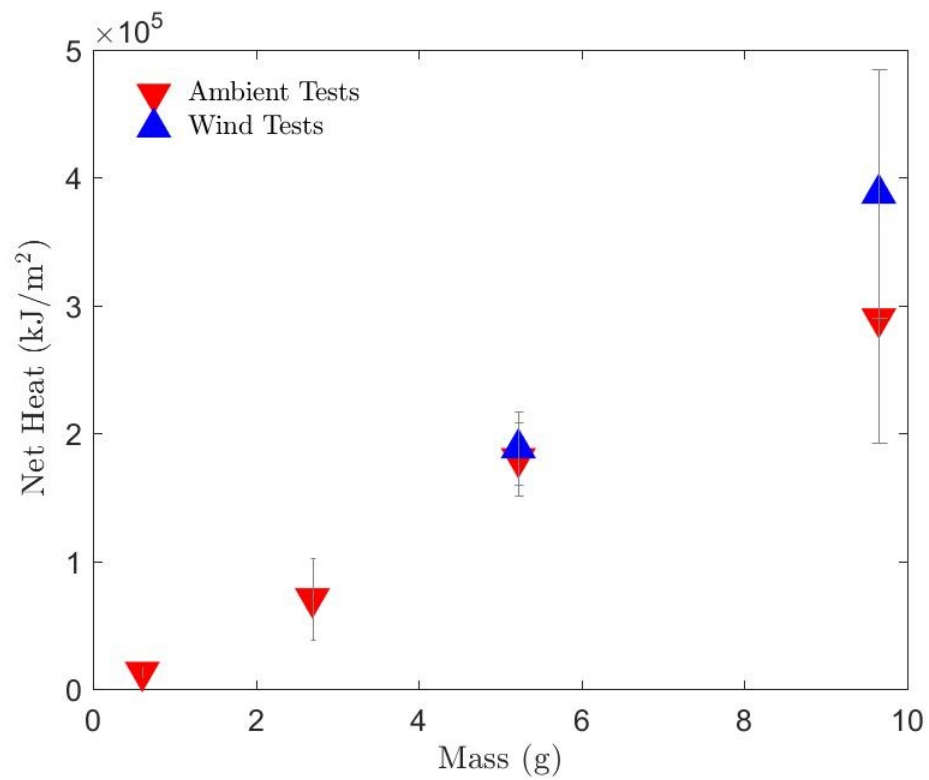


Figure 7.2: Net heating parameter as a function of deposited pile mass for ambient and forced flow experiments using 12.7 mm diameter firebrands.

Chapter 8: Conclusions

8.1 Overview

A methodology for conducting heat flux experiments for firebrand piles has been presented. A reliable method for producing piles without wind has been developed. Heat fluxes from a firebrand pile were measured using both a water-cooled heat flux gauge and an array of thin-skin calorimeters. Heat flux results were connected to an ignition condition and the thermal characteristics of the ignition configuration were described.

8.2 Conclusions

One of the most important aspects that this study highlighted is the difficulty of reliably measuring heat flux from a firebrand pile. Attempts were made to measure heat flux using both a water-cooled heat flux gauge and an array of thin-skin calorimeters; however, these measurements had high uncertainties. They serve better to illustrate trends and the approximate order of the heat flux, rather than exact values. One of the difficulties with measuring heat flux from the thin-skin

calorimeters was the difficulty of applying the calibration due to the dominance of different components of heat transfer in the calibration and in the experiment itself.

Several trends were identified which can motivate decisions on variables to study in future work, both in the laboratory and the in the field. Pile size (mass) was found to be the most important variable affecting heat flux curves and net heating. The results from piled firebrands are also distinctly different than those from a single firebrand, as the re-radiation within the pile appears to play an important role in heating.

Under ambient conditions, diameter was found to have a limited influence on the heat fluxes measured and net heating from firebrand piles, although it is known that firebrand size can be a critical ignition factor for a single firebrand. Ultimately, then, the diameter used for ignition experiments with firebrand piles likely becomes less important than the mass of the pile deposited. This dependence on mass may be critically important in choosing variables to measure during large scale tests or in the design of standard test methods for materials or components.

Finally, this study confirmed the importance of wind for ignition, but it also extended that to show how wind dramatically affects the heat flux that a firebrand pile produces. The ignition of a recipient fuel appears to take place very early after firebrand piles fall. It is possible that brief flaming from firebrands can act as a pilot to ignite the recipient fuel as it heats. These results differ from investigative reports that find that firebrand piles may ignite WUI fuels long after the fire front has passed. One key difference here is that a full firebrand pile is deposited at once

during these experiments, while single firebrands may be added to growing piles during an actual WUI fire.

8.3 Recommendations for Future Work

There are several areas of future work available based on the results of this study. One major drawback of the heat flux measured with the thin-skin calorimeters was the high uncertainty in the energy balance calculations and the applicability of the calibration method to this particular experimental set-up. There are two areas of future work related to measuring heat flux. It should be determined whether there is a better gauge to provide accurate heat flux measurements. It would be worth exploring the possibility of using a high temperature thermopile, which would solve the issue of potential water-cooling. Durability and repeatability would be important aspects to explore in the implementation of a thermopile. Nonetheless, a change in heating with area has been shown using the thin-skin calorimeters. It might be helpful in future tests to provide one good point estimate and a larger area of cost effective sensors (such as thin-skin calorimeters) around a main sensor.

Additionally, the development of a conduction-based calibration method would be one potential approach to using thin-skin calorimeters for quantitative measurements. The current calibration was based on an incident radiant heat flux and had high convective losses. A future calibration might change to a horizontal orientation and include the larger contribution of conductive heating.

This study focused solely on heat fluxes in a flat configuration; however, crevices and L-shaped configurations are also known to be important in structural fuels. Measuring heat fluxes during inert tests at different locations in the geometry will be important to understand the influence of these effects. Coupling this information to ignition conditions for an array of solid fuels typifying the WUI, as well as variations in brands including different shapes, such as wafers, and fuels would help to connect this directly to fire spread and development of standard test methodologies.

Initial results for a single ignition condition showed higher heat fluxes and firebrand piles that cooled and then re-heated. Exploring these trends over a wider range of wind velocities and firebrand pile sizes would be informative for real-world application and in building a model of the ignition process.

Appendix A:

The following Appendix includes additional plots. During the text, examples were given primarily for 12.7 mm diameter firebrands and 9.6 g deposited mass piles. The following provide additional data on other pile sizes and diameters. Included are raw thin-skin calorimeter data, raw water-cooled heat flux gauge data, and comparisons between the thin-skin calorimeters and the water-cooled heat flux gauge.

A.1 Raw Thin-Skin Calorimeter Results

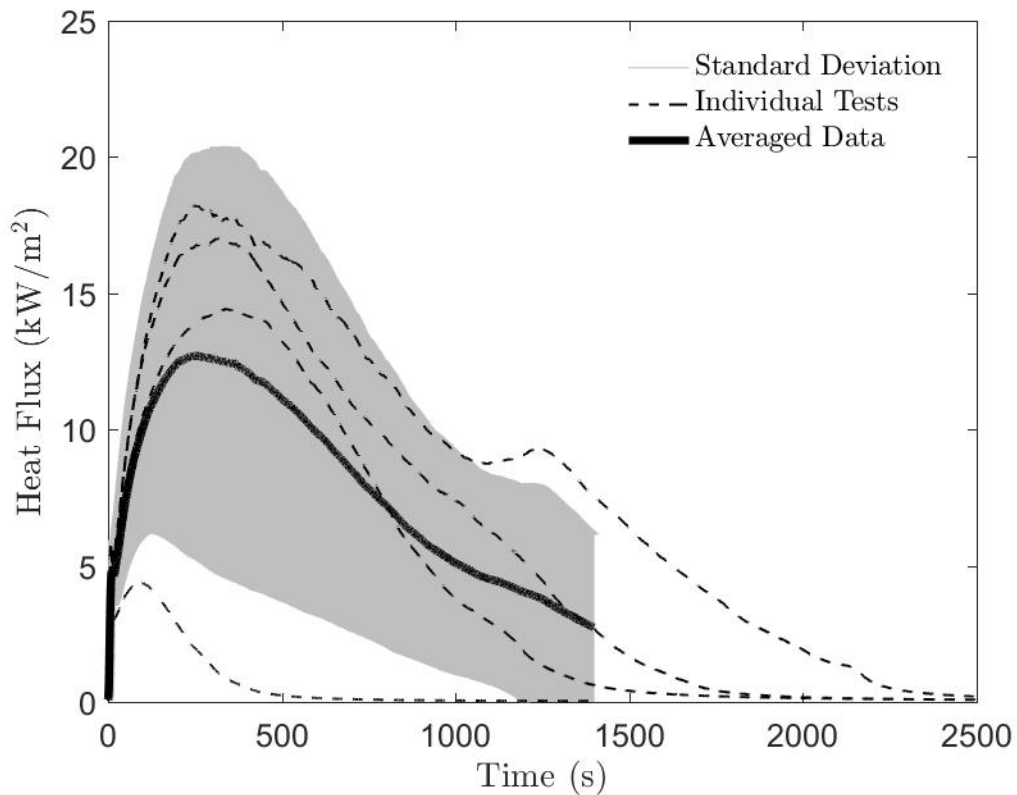


Figure 1: Heat flux as a function of time measured by the thin-skin calorimeter array under ambient conditions for 6.35 mm diameter firebrands of 100 g initial mass.

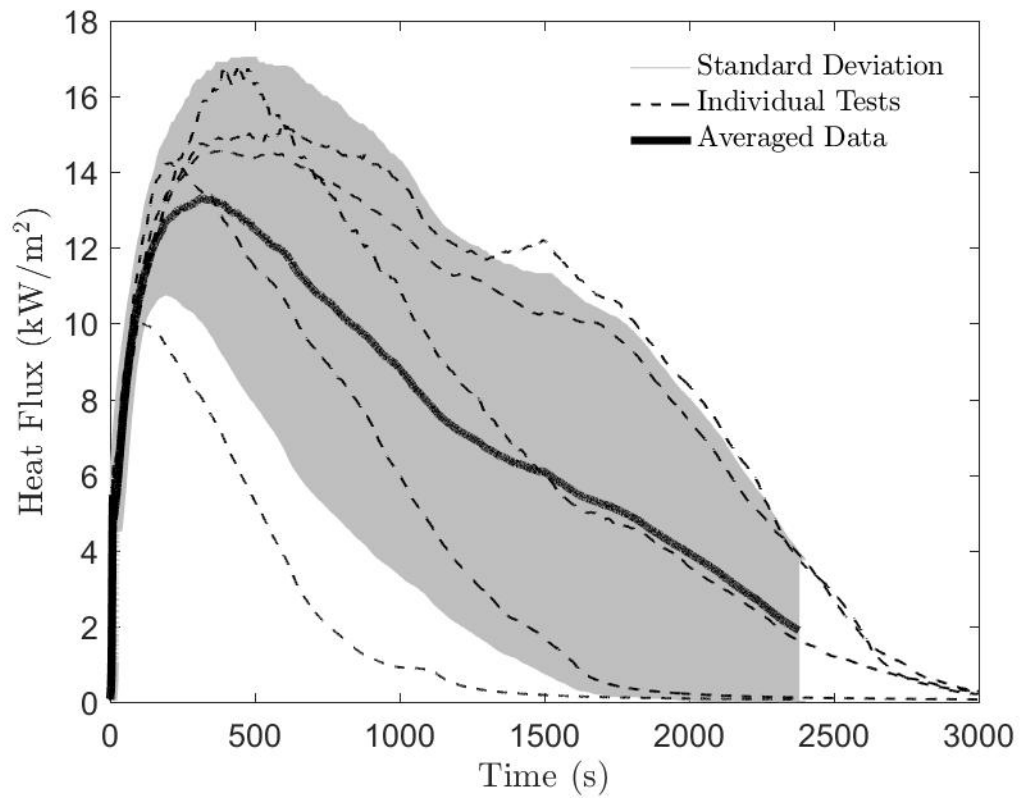


Figure 2: Heat flux as a function of time measured by the thin-skin calorimeter array under ambient conditions for 9.52 mm diameter firebrands of 100 g initial mass.

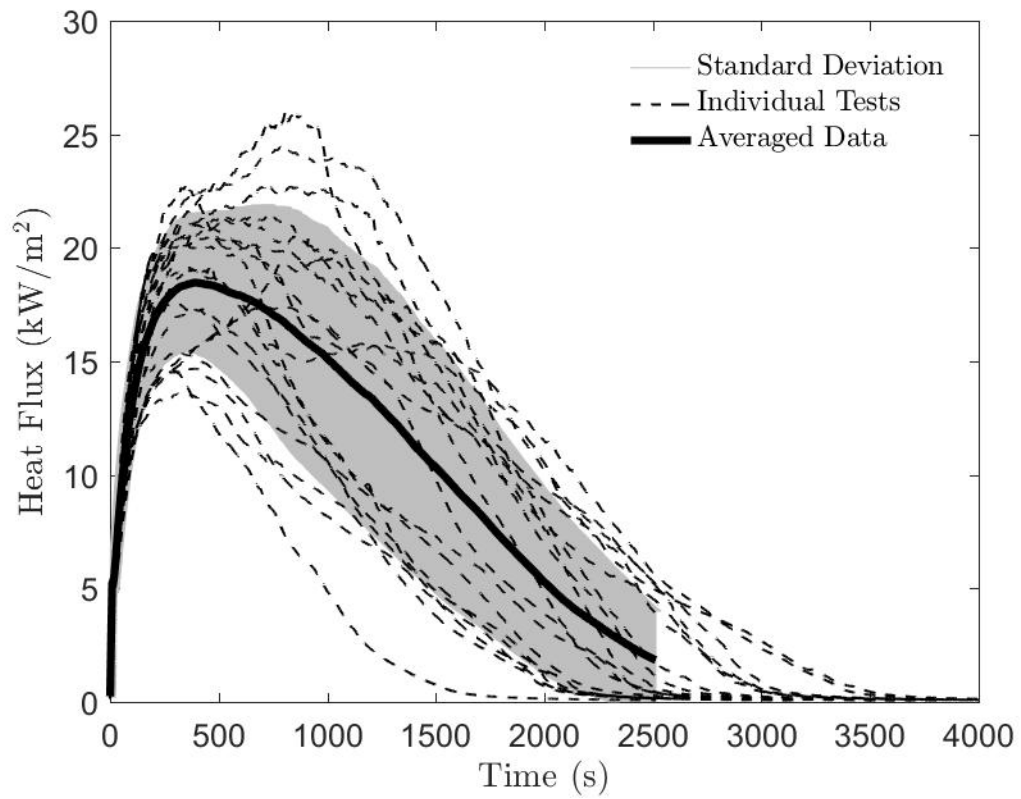


Figure 3: Heat flux as a function of time measured by the thin-skin calorimeter array under ambient conditions for 12.7 mm diameter firebrands of 100 g initial mass.

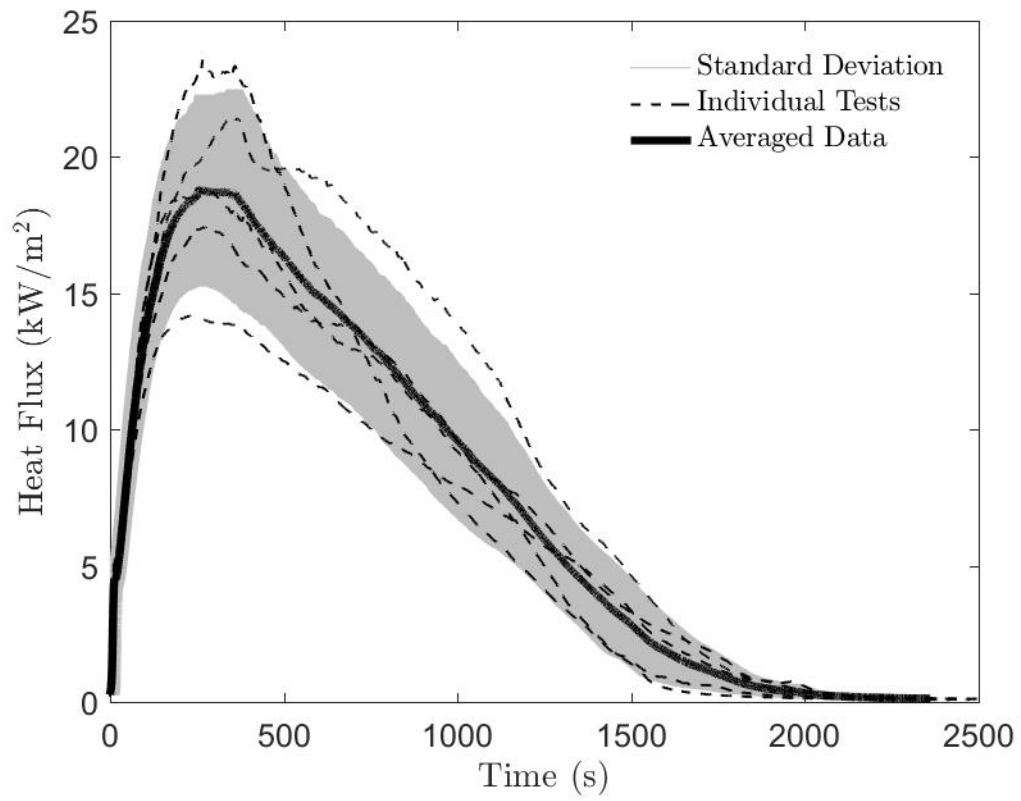


Figure 4: Heat flux as a function of time measured by the thin-skin calorimeter array under ambient conditions for 12.7 mm diameter firebrands of 50 g initial mass.

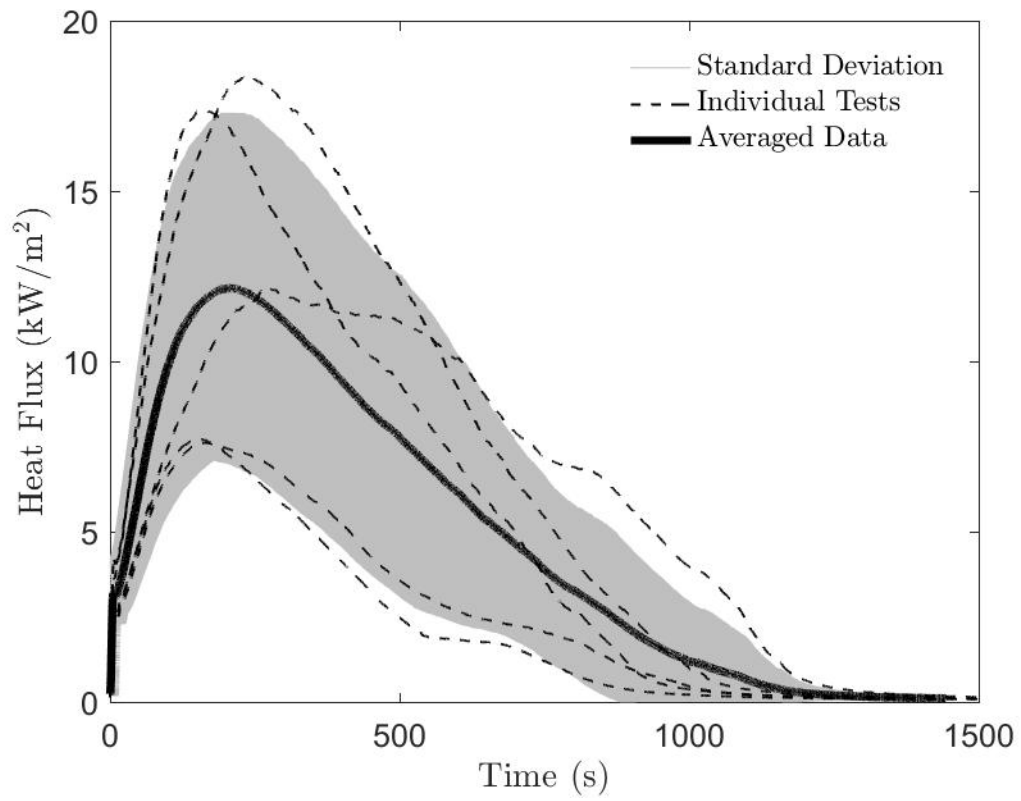


Figure 5: Heat flux as a function of time measured by the thin-skin calorimeter array under ambient conditions for 12.7 mm diameter firebrands of 20 g initial mass.

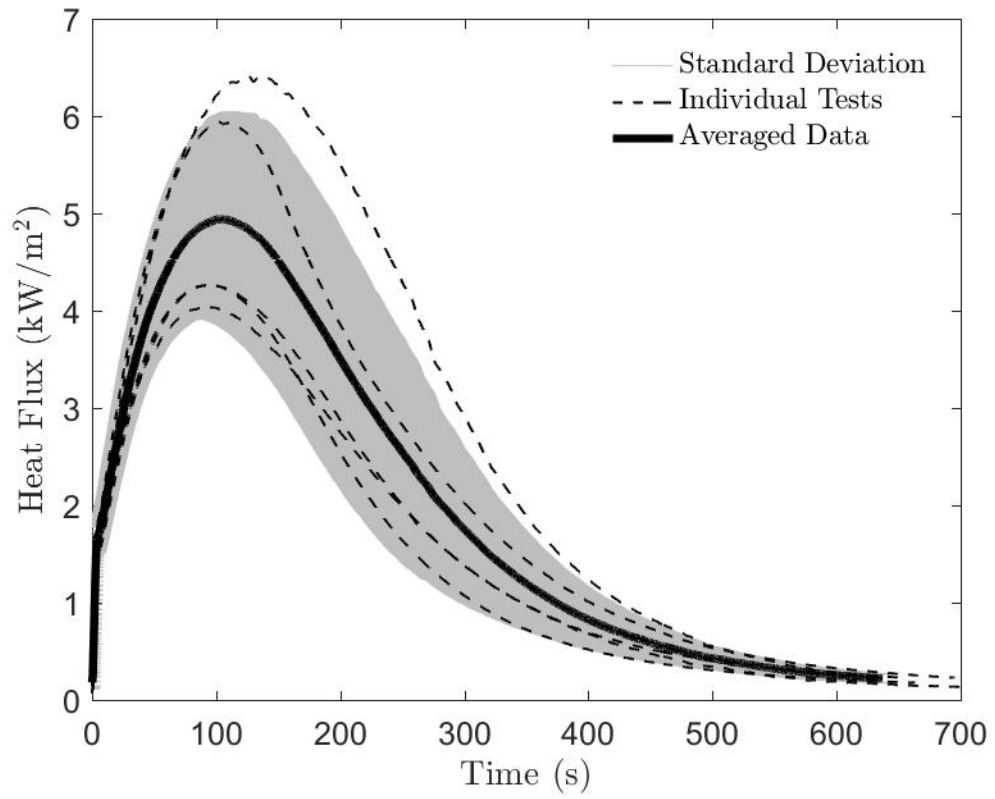


Figure 6: Heat flux as a function of time measured by the thin-skin calorimeter array under ambient conditions for 12.7 mm diameter firebrands of 1 brand.

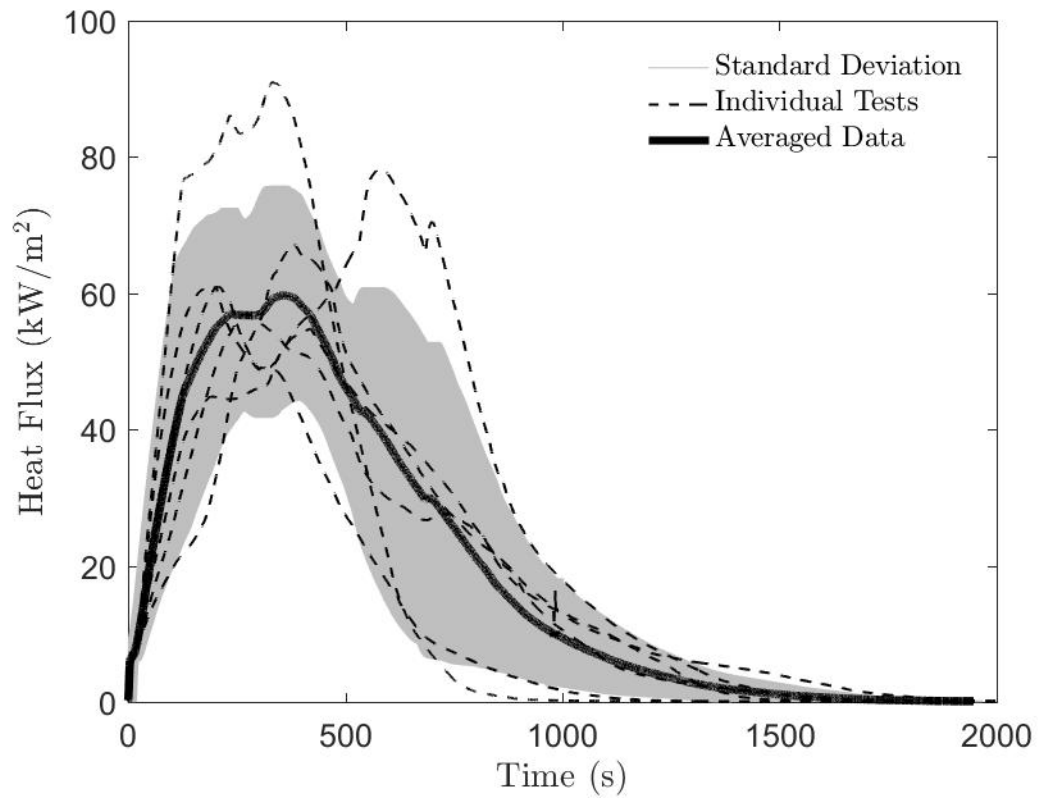


Figure 7: Heat flux as a function of time measured by the thin-skin calorimeter array under forced flow conditions for 12.7 mm diameter firebrands of 100 g initial mass.

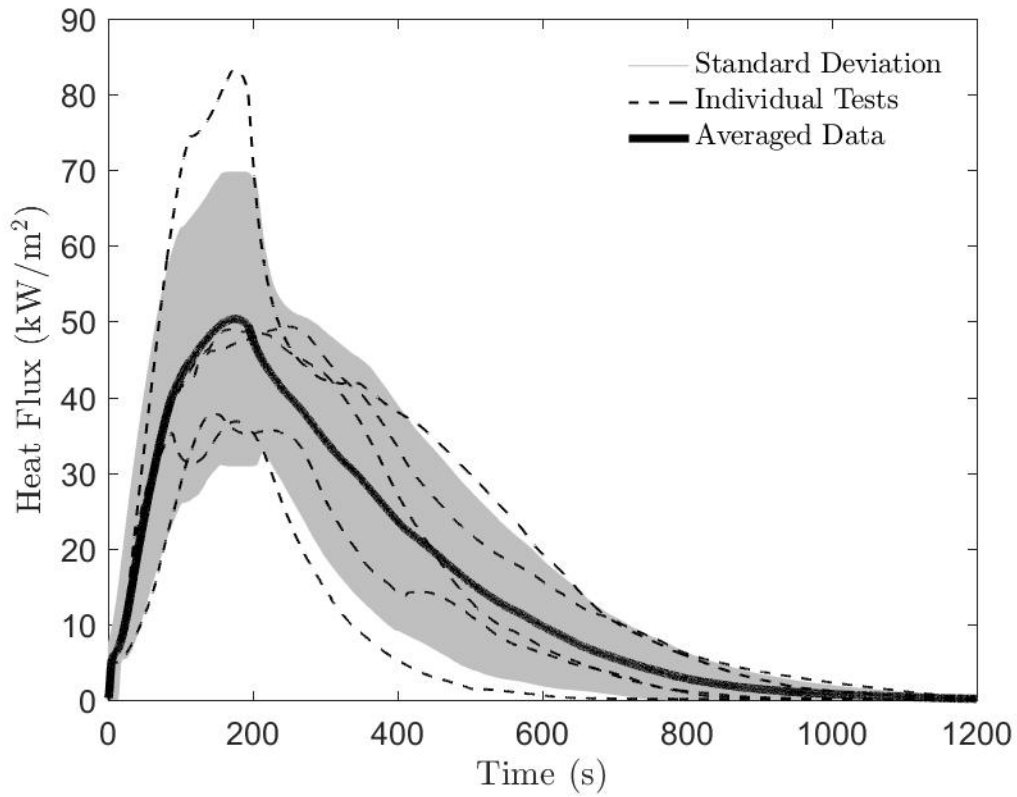


Figure 8: Heat flux as a function of time measured by the thin-skin calorimeter array under forced flow conditions for 12.7 mm diameter firebrands of 50 g initial mass.

A.2 Raw Water-Cooled Heat Flux Gauge Results

The following are raw water-cooled heat flux gauge plots showing all tests, with averages, and uncertainties.

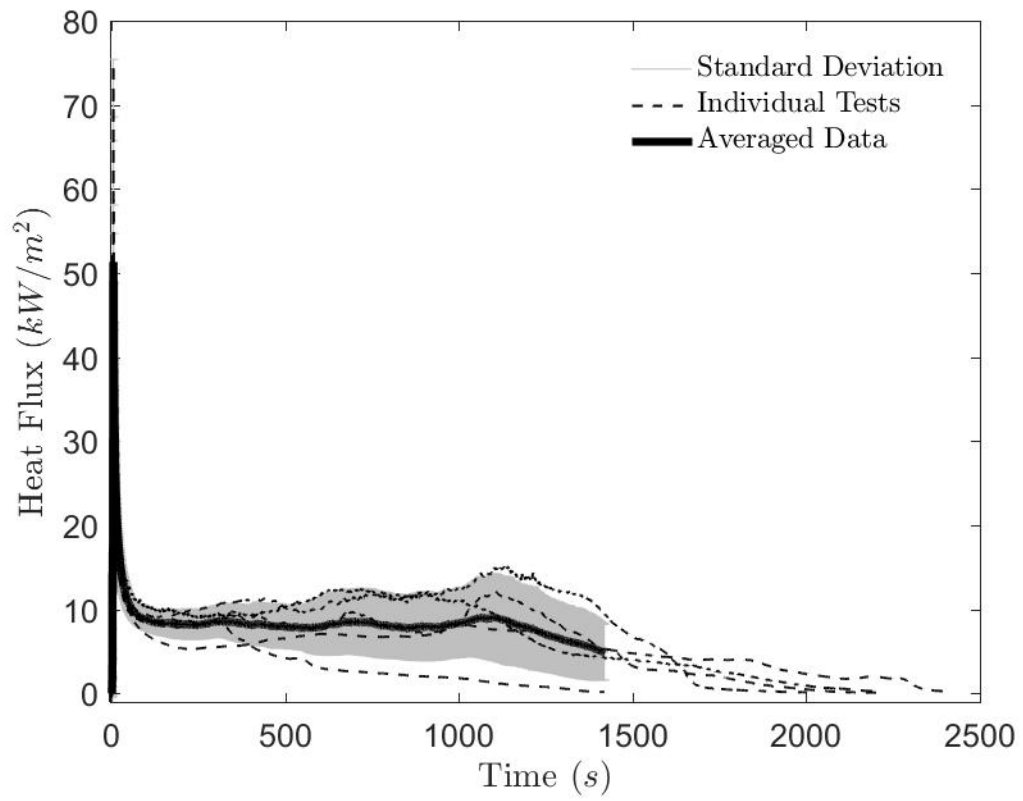


Figure 9: Heat flux as a function of time as measured by the water-cooled heat flux gauge for 6.35 mm firebrands and 6.3 g deposited mass.

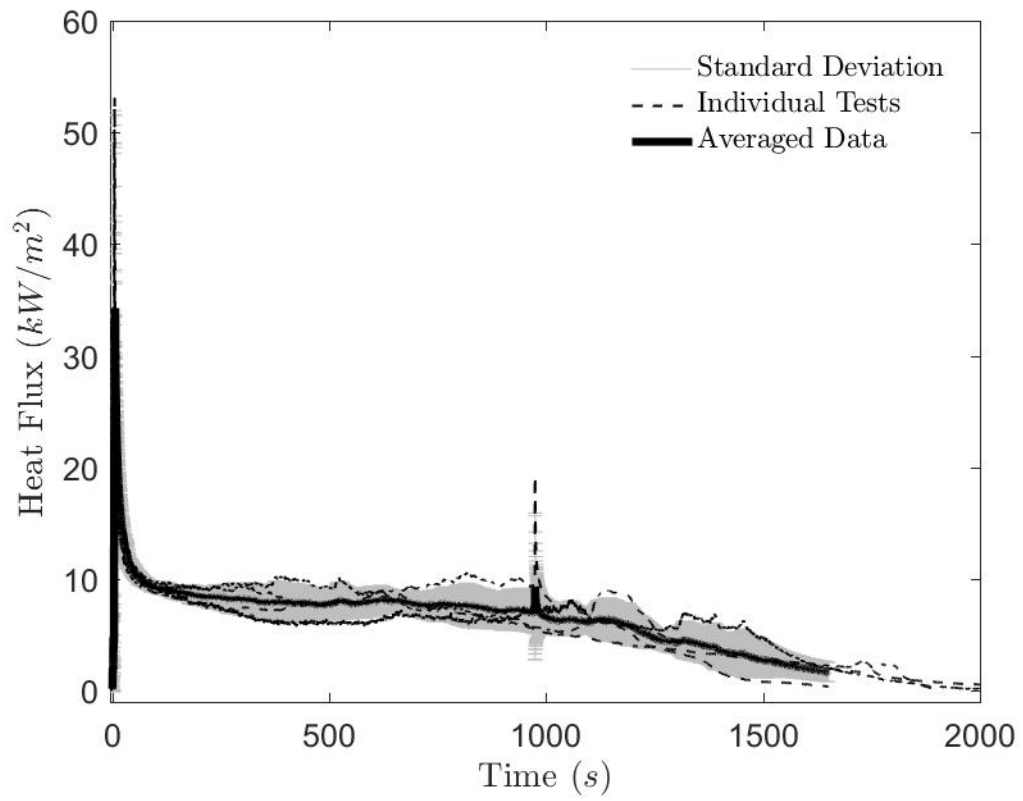


Figure 10: Heat flux as a function of time as measured by the water-cooled heat flux gauge for 9.52 mm firebrands and 8.2 g deposited mass.

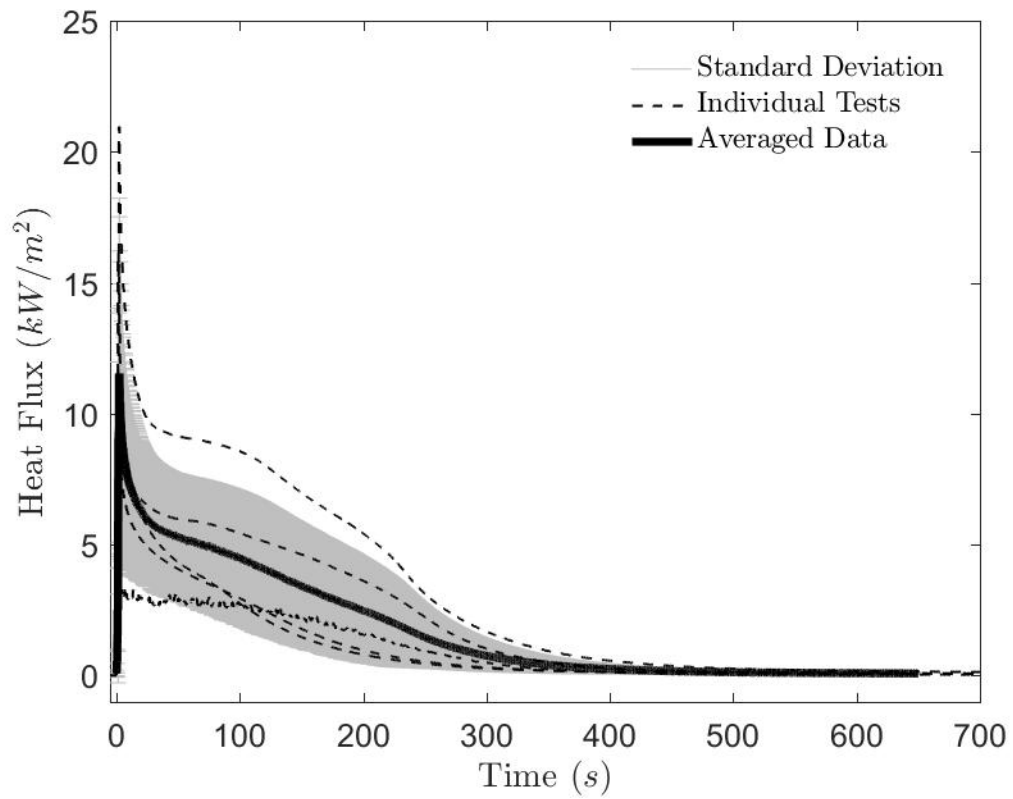


Figure 11: Heat flux as a function of time as measured by the water-cooled heat flux gauge for 12.7 mm firebrands and a single brand test.

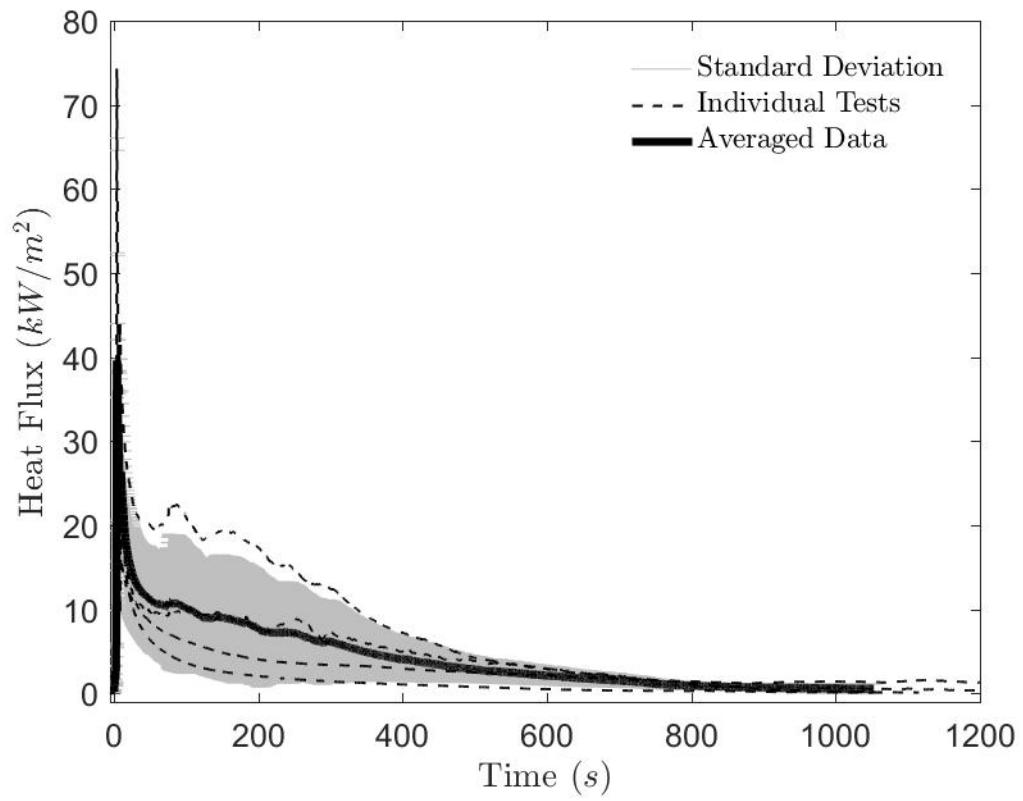


Figure 12: Heat flux as a function of time as measured by the water-cooled heat flux gauge for 12.7 mm firebrands and 2.7 g deposited mass.

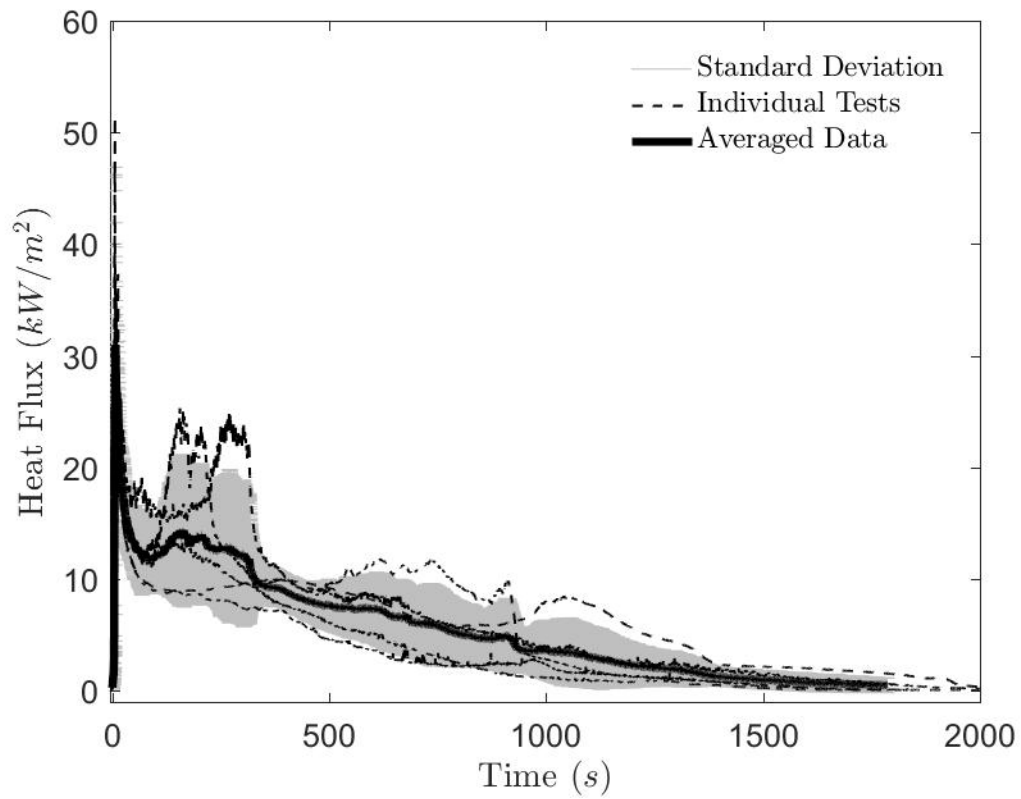


Figure 13: Heat flux as a function of time as measured by the water-cooled heat flux gauge for 12.7 mm firebrands and 5.2 g deposited mass.

A.3 Gauge Comparison Plots

The following are plots comparing the averaged results of the thin-skin calorimeters and the water-cooled heat flux gauge.

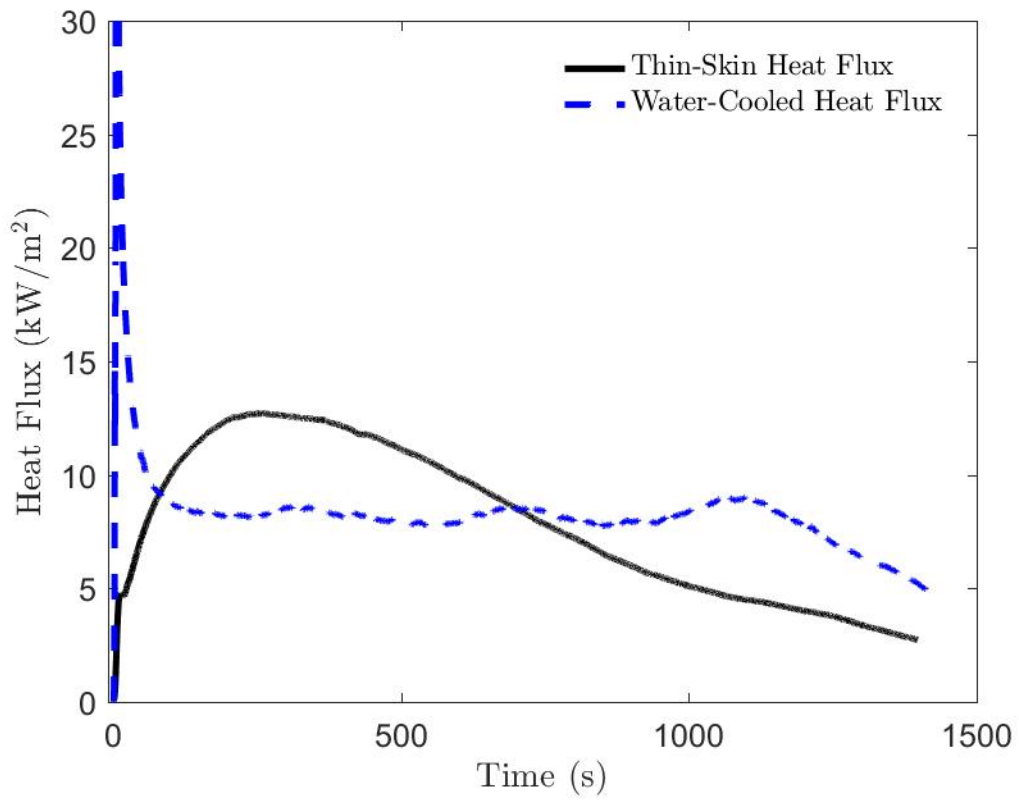


Figure 14: Comparison of average heat flux results using the thin-skin calorimeter array vs. the water-cooled heat flux gauge. 6.35 mm diameter, 100 g initial mass.

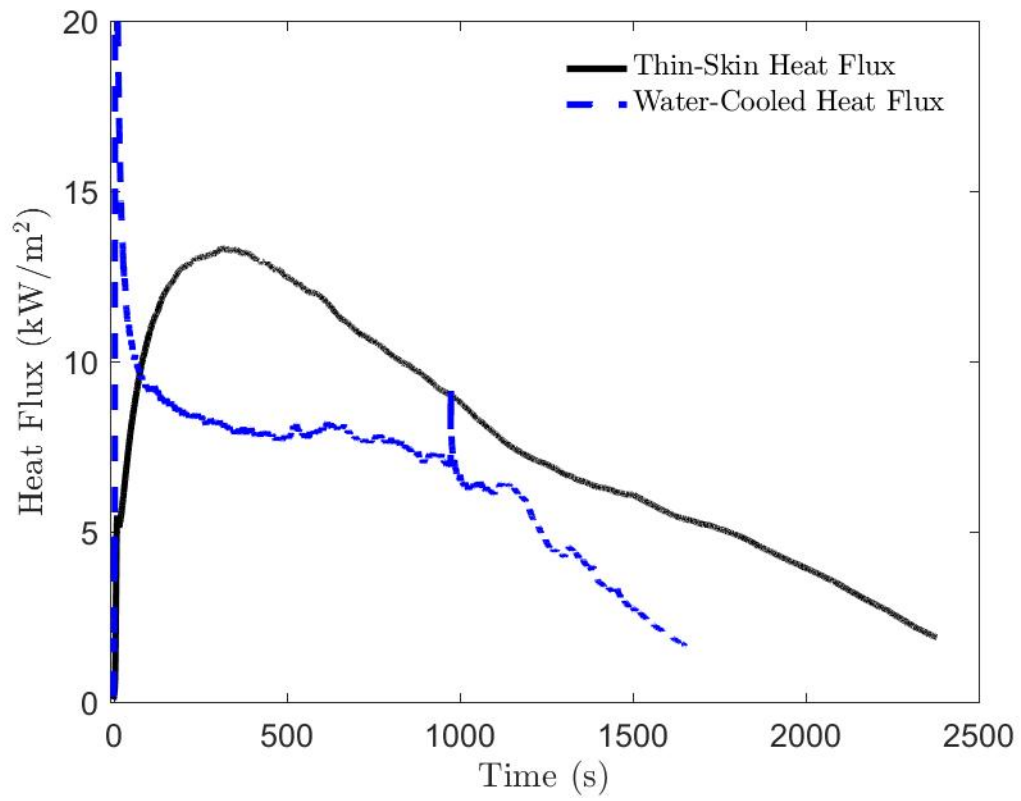


Figure 15: Comparison of average heat flux results using the thin-skin calorimeter array vs. the water-cooled heat flux gauge. 9.52 mm diameter, 100 g initial mass.

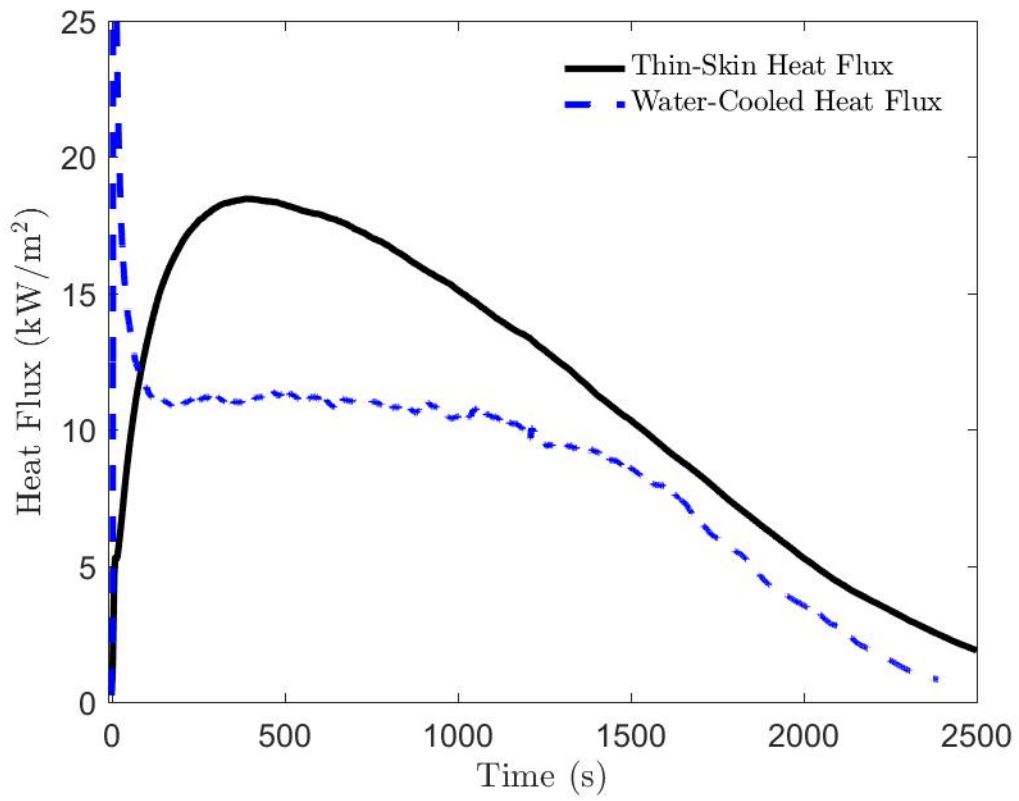


Figure 16: Comparison of average heat flux results using the thin-skin calorimeter array vs. the water-cooled heat flux gauge. 12.7 mm diameter, 100 g initial mass.

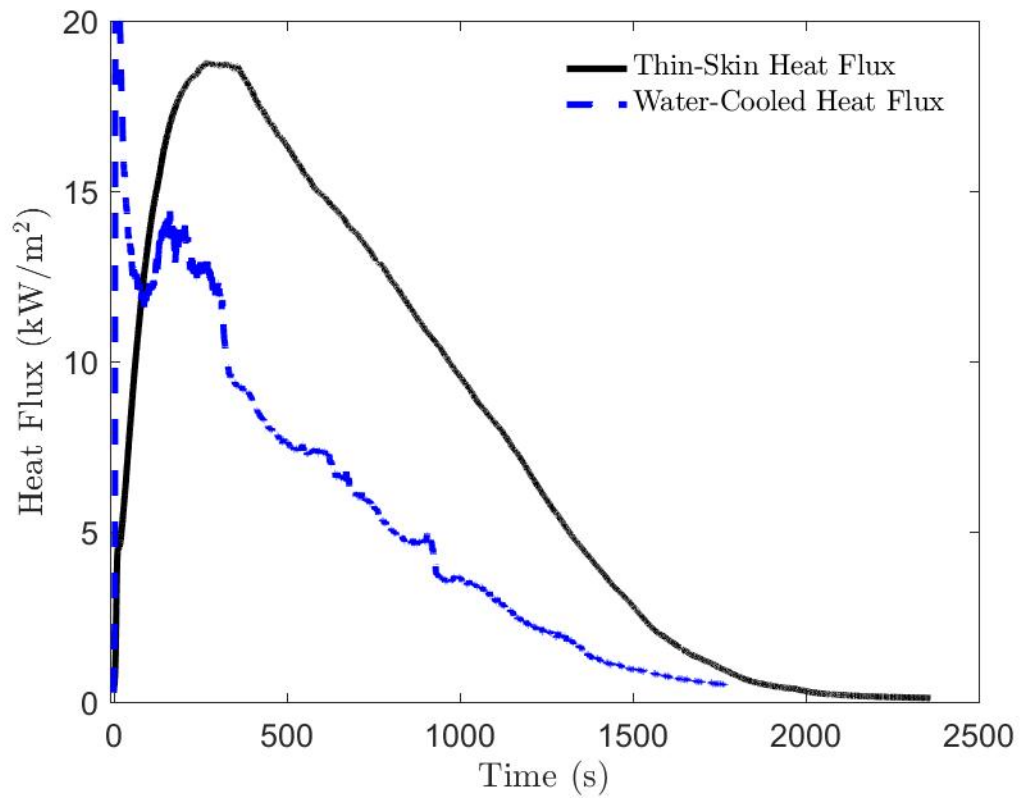


Figure 17: Comparison of average heat flux results using the thin-skin calorimeter array vs. the water-cooled heat flux gauge. 12.7 mm diameter, 50 g initial mass.

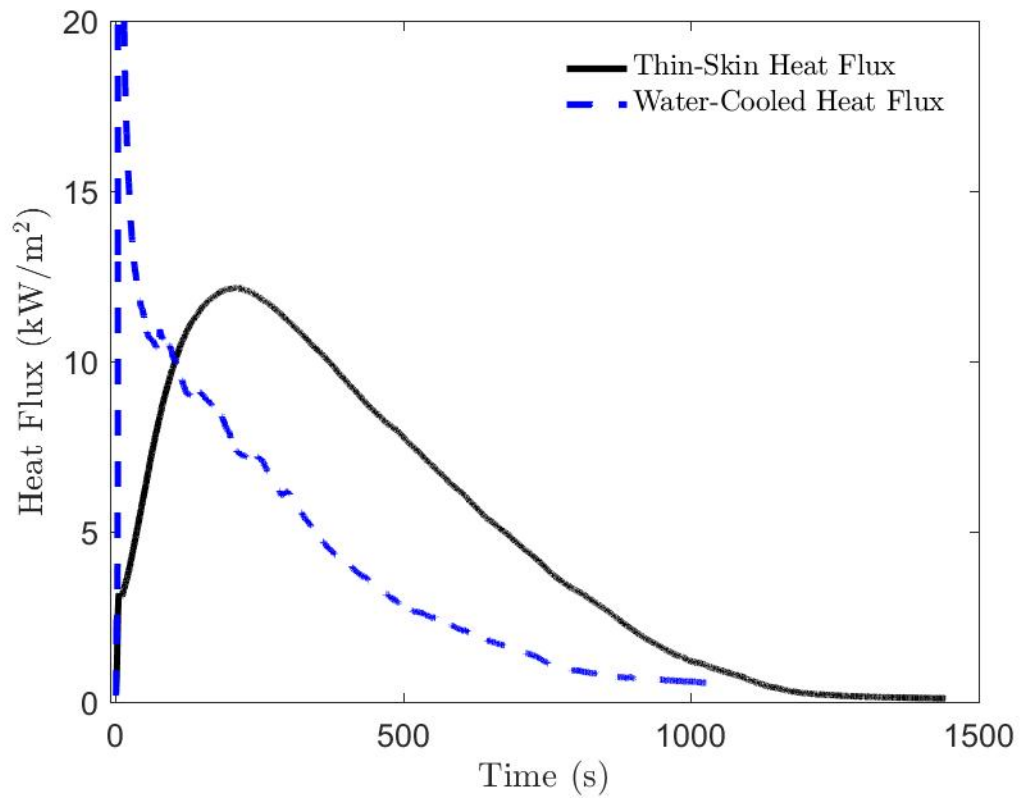


Figure 18: Comparison of average heat flux results using the thin-skin calorimeter array vs. the water-cooled heat flux gauge. 12.7 mm diameter, 20 g initial mass.

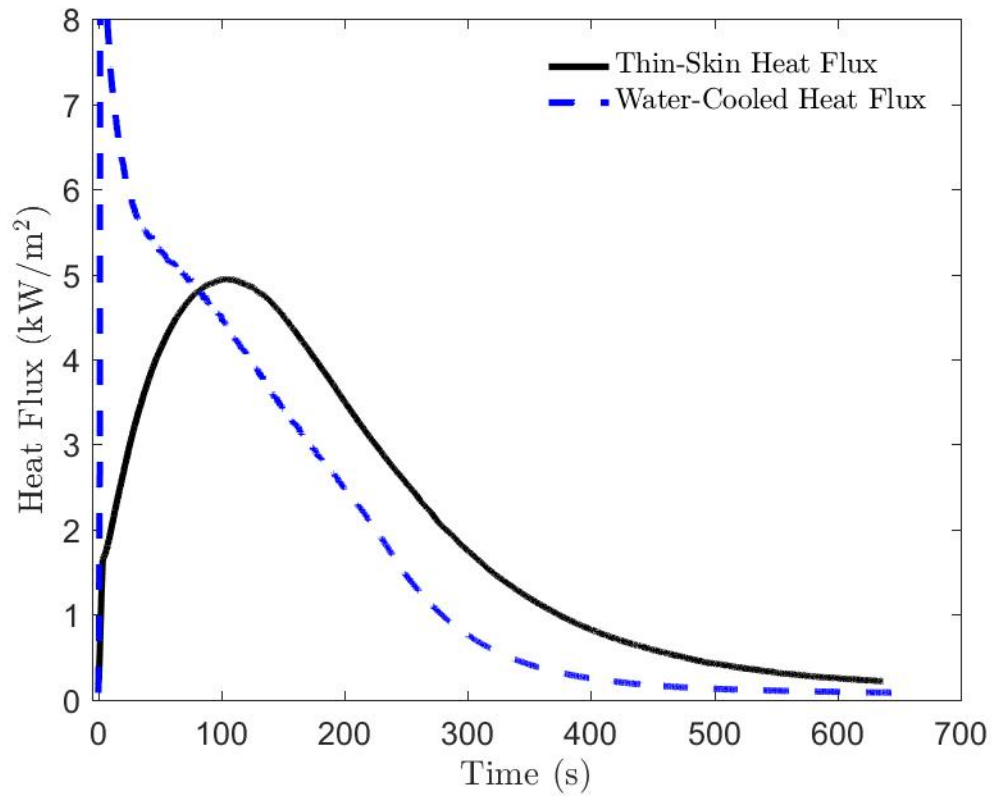


Figure 19: Comparison of average heat flux results using the thin-skin calorimeter array vs. the water-cooled heat flux gauge. 12.7 mm diameter, single brand.

Bibliography

- [1] Manzello, S.L. and S. Suzuki. Exposing Decking Assemblies to Continuous Wind-Driven Firebrand Showers. In: Proceedings of the 11th International Fire Safety Science Symposium, pp. 1339-1352, 2014. DOI: 10.3801/IAFSS.FSS.11-1339.
- [2] Hadden, R.M., S. Scott, C. Lautenberger, and A.C. Fernandez-Pello. Ignition of Combustible Fuel Beds by Hot Particles: An Experimental and Theoretical Study. *Fire Technology*, 47:341-355, 2011. DOI: 10.1007/s10694-010-0181.
- [3] Caton, S. Laboratory Studies on the Generation of Firebrands from Cylindrical Wooden Dowels. Masters Thesis. University of Maryland, College Park, 2016.
- [4] Radeloff, V.C., R.B. Hammer, S.I. Stewart, J.S. Fried, S.S. Holcomb, and J.F. McKeefry. The Wildland-Urban Interface in the United States. *Ecological Application*, 15(3):799-805, 2005. DOI: 10.1890/04-1413.
- [5] National Interagency Coordination Center. Wildland Fire Summary and Statistics Annual Report 2016. National Interagency Coordination Center, Boise, Idaho, 2016.
- [6] Grishin, A.M, A.I. Filkov, E.L. Loboda, V.V. Reyno, A.V. Kozlov, V.T. Kuznetsov, D.P. Kasymov, S.M. Andreyuk, A.I. Ivanov, and N.D. Stolyarchuk. A field experiment on grass fire effects on wooden constructions and peat layer ignition. *International Journal of Wildland Fire*, 23:445-449, 2014. DOI: 10.1071/WF12069.
- [7] Caton, S.E., R.S.P. Hakes, D.J. Gorham, A. Zhou, and M.J. Gollner. Review of Pathways for Building Fire Spread in the Wildland Urban Interface Part I: Exposure Conditions. *Fire Technology*, 53(2):429-473, 2016. DOI: 10.1007/s10694-016-0589-z.

- [8] Cohen, J. The Wildland-Urban Interface Problem. *Forest History Today*, pp. 20-26, 2008 (Fall).
- [9] Theobald, D. and W. Romme. Expansion of the U.S. wildland-urban interface. *Landscape and Urban Planning*, 83:340-354, 2007. DOI: 10.1016/j.landurbplan.2007.06.002.
- [10] Cohen, J. Relating flame radiation to home ignition using modeling and experimental crown fires. *Canadian Journal of Forest Research*, 34:1616-1626, 2004. DOI: 10.1139/x04-049.
- [11] National Fire Protection Association. The basics of defensible space and the home-ignition zone, 2006. URL: <http://www.firewise.org/wildfire-preparedness/be-firewise/home-and-landscape/defensible-space.aspx>.
- [12] Cohen, J.D. and R.D. Stratton. Home Destruction Examination: Grass Valley Fire, Lake Arrowhead, CA. United States Department of Agriculture, R5-TP-026b, 2008 (June).
- [13] Quarles, S., P. Leschak, R. Cowger, K. Worley, R. Brown, and C. Iskowitz. Lessons Learned from Waldo canyon: Fire Adapted Communities Mitigation Assessment Team Findings. Insurance Institute for Business and Home Safety, 2012.
- [14] Maranghides, A., D. McNamara, R. Vihnanek, J. Restaino, and C. Leland. A Case Study of a Community Affected by the Waldo Fire – Event Timeline and Defensive Actions. Technical Note (TN 1910). National Institute of Standards and Technology, 2015. DOI: 10.6028/NIST.TN.1910.
- [15] Maranghides, A. and W. Mell. A case study of a community affected by the Witch and Guejito fires. Technical Note (TN 1635). National Institute of Standards and Technology, Gaithersburg, Maryland, 2009.
- [16] Maranghides, A., D. McNamara, W. Mell, J. Trook, and B. Toman. A case study of a community affected by the Witch and Guejito fires: Report 2 - evaluating the effects of hazard mitigation actions on structure ignitions. Technical Note (TN 1796) National Institute of Standards and Technology, 2013.
- [17] Mell, W.E., S.L. Manzello, A. Maranghides, D. Butry, and R.G. Rehm. The wildland-urban interface problem – current approaches and research needs. *International Journal of Wildland Fire*, 19:238-251, 2010. DOI: 10.1071/WF07131.

- [18] Manzello, S.L., T.G. Cleary, J.R. Shields, and J.C. Yang. Ignition of mulch and grasses by firebrands in wildland-urban interface fires. *International Journal of Wildland Fire*, 15:427-431, 2006. DOI: 10.1071/WF06031.
- [19] Martin, S. Diffusion-Controlled ignition of cellulosic materials by intense radiant energy. In: 10th International Symposium on Combustion, pp. 877-896, 1965.
- [20] Drysdale, D.D. and H.E. Thomas. Flammability of Plastics II: Critical Mass Flux at Firepoint. *Fire Safety Journal*, 14:179-188, 1989.
- [21] Rein, G. Smoldering Combustion. Chapter 19. In: SFPE Handbook of Fire Protection Engineering, 5th Ed., Ed: M.J. Hurley. Pp. 581-603. Springer, New York, 2016.
- [22] Anthenien, R.A. and A.C. Fernandez-Pello. A Study of Forward Smolder Ignition of Polyurethane Foam. In: 27th International Symposium on Combustion, pp. 2683-2690, 1998.
- [23] Gratkowski, M.T., N.A. Dembsey, and C.L. Beyler. Radiant smoldering ignition of plywood. *Fire Safety Journal*, 41:427-442, 2006. DOI: 10.1016/j.firesaf.2006.03.006.
- [24] Gol'dshleger, U.I., K.V. Pribytkova, and V.V. Barzykin. Ignition of a Condensed Explosive By A Hot Object of Finite Dimensions. Translated from *Fizika Goreniya i Vzryva*, 9(1):119-123, 1973.
- [25] Zak, C., J. Urban, V. Tran, and C. Fernandez-Pello. Flaming Ignition Behavior of Hot Steel and Aluminum Spheres Landing in Cellulose Fuel Beds. In: Fire Safety Science Proceedings of the 11th International Symposium, pp. 1368-1378, 2014. DOI: 10.3801/IAFSS.FSS.11-1368.
- [26] Fernandez-Pello, A.C., C. Lautenberger, D. Rich, C. Zak, J. Urban, R. Hadden, S. Scott, and S. Fereres. Spot fire ignition of natural fuel beds by hot metal particles, embers, and sparks. *Combustion Science and Technology*, 187:269-295, 2015. DOI: 10.1080/00102202.2014.973953.
- [27] Gray, B.F. Spontaneous Combustion and Self Heating. Chapter 20. In: SFPE Handbook of Fire Protection Engineering, 5th Ed., Ed: M.J. Hurley. Pp. 604-632. Springer, New York, 2016.
- [28] Dosanjh, S. and P.J. Pagni. Forced Countercurrent Smoldering Combustion. Proceedings of the Second ASME-JSME Thermal Engineering Joint Conference, 1987.

- [29] Ellis, P.F.M. Firebrand characteristics of the stringy bark of messmate (*Eucalyptus obliqua*) investigated using non-tethered samples. *International Journal of Wildland Fire*, 22:642-651, 2013. DOI: 10.1017/WF12141.
- [30] Santamaria, S., K. Kempná, J.C. Thomas, M. El Houssami, E. Mueller, D. Kasimov, A. Filkov, M.R. Gallagher, N. Skowronski, R. Hadden, and A. Simeoni. Investigation of structural wood ignition by firebrand accumulation. In: *Proceedings of the First International Conference on Structures Safety under Fire Blast*, 2015.
- [31] Dowling, V.P. Ignition of Timber Bridges in Bushfires. *Fire Safety Journal*, 22:145-168, 1994.
- [32] Quarles, S.L., L.G. Cool, and F.C. Beall. Performance of Deck Board Materials Under Simulated Wildfire Exposures. In: *Proceedings of the Seventh International Conference on Woodfiber-Plastic Composites*, pp. 89-93, 2003.
- [33] Viegas, D.X., M. Almeida, J. Raposo, R. Oliveria, and C.X. Viegas. Ignition of Mediterranean Fuels Beds by Several Types of Firebrands. *Fire Technology*, 50(1):60-77, 2014. DOI: 10.1007/s10694-012-0267-8.
- [34] Manzello, S.L., T.G. Cleary, J.R. Shields, and J.C. Yang. On the ignition of fuel beds by firebrands. *Fire and Materials*, 30:77-87, 2006. DOI: 10.1002/fam.901.
- [35] Waterman, T.E. and A.N. Takata. Laboratory Study of Ignition of Host Materials by Firebrands. IIT Research Institute, 1969.
- [36] Manzello, S.L., S. Park, and T.G. Cleary. Investigation on the ability of glowing firebrands deposited within crevices to ignite common building materials. *Fire Safety Journal*, 44:894-900, 2009. DOI: 10.1016/j.resaf.2009.05.001.
- [37] Manzello, S.L., S. Suzuki, and Y. Hayashi. Enabling the study of structure vulnerabilities to ignition from wind driven firebrand showers: A summary of experimental results. *Fire Safety Journal*, 54:181-196, 2012. DOI: 10.1016/j.resaf.2012.06.012.
- [38] Hildalgo, J.P., C. Maluk, A. Cowlard, C. Abecassis-Empis, M. Krajcovic, and J.L. Torero. A Thin Skin Calorimeter (TSC) for quantifying irradiation during large-scale fire testing. *International Journal of Thermal Sciences*, 112:383-394, 2017. DOI: 10.1016/j.ijthermalsci.2016.10.013.
- [39] Manzello, S.L., A. Maranghides, J.R. Shields, W.E. Mell, Y. Hayashi, and D. Nii. Mass and size distribution of firebrands generated from burning Ko-

- rean pine (*Pinus koraiensis*) trees. *Fire and Materials*, 33:21-31, 2009. DOI: 10.1002/fam.977.
- [40] Forest Products Laboratory. Wood Handbook: Wood as an Engineering materials, pp. 2.4-2.18. United States Department of Agriculture, 2010.
- [41] American Society for Testing and Materials. ASTM D4442: Standard Test Methods for Direct Moisture Content Measurement of Wood and Wood-Based Materials, 2015.
- [42] Miller, C.H., W. Tang, M.A. Finney, S.S. McAllister, J.M. Forthofer, and M.J. Gollner. An investigation of coherent structures in laminar boundary layer flames. *Combustion and Flame*, 181:123-135, 2017. DOI: 10.1016/j.combustflame.2017.03.007.
- [43] Safronava, N., R.E. Lyon, S. Crowley, and S.I. Stoliarov. Effect of Moisture on Ignition Time of Polymers. *Fire Technology*, 51:1093-1112, 2015. DOI: 10.1007/s10694-014-0434-1.
- [44] Singh, A.V. and M.J. Gollner. Local Burning Rates and Heat Flux for Forced Flow Boundary-Layer Diffusion Flames. *AIAA Journal*, 54(2):408-418, 2016. DOI: 10.2514/1.J054283.
- [45] Muller, E., N. Skowronski, K. Clark, R. Kremens, M. Gallagher, J. Thomas, M. El Houssamia, A. Filkov, B. Butler, J. Hom, W. Mell, and A. Simeoni. An experimental approach to the evaluation of prescribed fire behavior. In: *Advances in forest fire research*, Imprensa da Universidade de Coimbra, 2014. DOI: 10.14195/978-989-26-0884-64.
- [46] American Society for Testing and Materials. ASTM E459: Standard Test Method for Measuring Heat Transfer Rate Using a Thin-Skin Calorimeter, 2016.
- [47] Special Metals Corporation. INCONEL alloy 625, 2013.
- [48] Ballestrín, J. Direct Heat-Flux Measurement (MDF) for Solar Central Receiver Evaluation. *Informes Técnicos Ciemat*, 961, 2001.